Investigating the impact of stellar feedback algorithms on galactic evolution

by

Samantha R Pillsworth

A Thesis Submitted to
Saint Mary's University, Halifax, Nova Scotia
in Partial Fulfillment of the Requirements for
the Degree of Master of Science in Astronomy
(Department of Astronomy and Physics)

April 20, 2016, Halifax, Nova Scotia

Approved: Dr. Rob Thacker(Supervisor)

Approved: Dr. David Guenther (Examiner)

Approved: Dr. Marcin Sawicki (Examiner)

Date: April 20, 2016.

Acknowledgements

I would like to express my sincere thanks to Dr. Rob Thacker for acting as my supervisor and mentor during this time. His critiques of this work were invaluable, and his patience during this process was immeasurable. Without his support, this work would not have been possible. Next, I would like to thank Ben Keller, both for the simulation results used in this study, and for his helpful advice during the analysis process. I would also like to thank my committee members, Dr. David Guenther and Dr. Marcin Sawicki, for their time and discussion.

The support and inspiration I received from my colleagues at Saint Mary's cannot be overestimated. I am immensely grateful to Dr. Luigi Gallo for helpful discussions during this process, and to Dr. Roby Austin for our talks over the past semester. My fellow graduate students, past and present, are a constant source of encouragement. Thank you to Liz, Mitch, Kirsten, Anneya, Diego, Rasalhague, Adam, Chris, Jenn, and Maan. The conversations of the graduate office were always enlightening (although not always about astrophysics).

I must express my very profound gratitude to my friends and family. Their support and cheer has been indispensable to me while undertaking this endeavour. Lastly, I must thank Bryan for puzzling over the Universe with me.

Contents

1 Introduction **1**

1.1 Galaxy Formation . . . 2

1.1.1 Collapse of DM Halos . . . 3

1.1.2 Collapse of Baryons . . . 6

1.2 Galaxy Evolution . . . 9

1.2.1 Star Formation . . . 9

1.2.2 Stellar Feedback . . . 10

1.2.3 AGN Feedback . . . 13

1.2.4 Mergers . . . 14

1.3 Analytic and Semi-Analytic Modelling . . . 15

1.4 Simulations . . . 16

2 Methods **21**

2.1 Smoothed Particle Hydrodynamics . . . 21

2.2 GASOLINE2 . . . 23

2.3 Blastwave Feedback . . . 25

2.4 Superbubble Feedback . . . 27

2.4.1 Thermal Conduction . . . 27

2.4.2 Mass Evaporation . . . 28

2.4.3 Multi-Phase Particles 29
2.4.4 Initial Conditions 30

3 Results **32**

3.1 $z = 0$ Galaxy Morphology: Comparing the Results of Different Feedback Mechanisms 32
3.1.1 The Density Structure of the Gas Disk 32
3.1.2 The Temperature Structure of the Gas 41
3.1.3 Velocity Structure of the Nucleus, Disk, and Halo 46
3.2 Galactic Structure Evolution 51
3.2.1 Star Formation Rates 51
3.2.2 Evolution of the Disk Mass 54
3.2.3 Evolution of the Dark Matter within the Virial Radius 64
3.3 Fuelling Star Formation through Gas Accretion 69
3.3.1 The General Accretion Rate: Flux through a Spherical Shell 70
3.3.2 Accretion onto the Disk: Flux through the sheet and Annuli Geometries 74
3.3.3 Reducing Scatter via Co-Added outputs 83

4 Discussion and Conclusions **90**

4.0.1 Limitations 93
4.0.2 Future Work 94

APPENDICES **95**

A Scale Heights and Radii **95**

List of Figures

1.1 The luminosity distribution calculated by Press & Schechter (1974) shown as the dotted and dashed lines, compared to observations of the Coma cluster by Oemler (1973). Data replotted from Press & Schechter (1974) 5

1.2 A cartoon showing the general two-step process of galaxy formation. Blue represents dark matter, red represents hot gas, while green represents cold gas. At t_1 is a cold dark matter halo. As baryons fall into the potential well, they are shock heated, t_2. The inner region of hot gas halo cools, forming a rotationally supported disk, t_3. The gas continues to cool and accrete onto the disk, t_4. Based on figure 8, Baugh,2006. 8

3.1 The surface density of cold (top) and warm gas (bottom) in g1536_BW is plotted against height. An inner profile is fit in red, and an outer profile is fit in magenta. 36

3.2 The surface density of all gas in the disk of g1536_BW plotted against radius. The break point, separating the outer and inner profiles, is used to define the edge of the disk. 36

3.3 The smoothed face-on density field for disk g1536 simulated with the three distinct feedback algorithms. 39

3.4 The smoothed edge-on density field for disk g1536 simulated with the three distinct feedback algorithms. 39

3.5 The smoothed face-on density field for disk g15784 simulated with the three distinct feedback algorithms. 39
3.6 The smoothed edge-on density field for disk g15784 simulated with the three distinct feedback algorithms. The white lines in the NF panel depict the sheet (solid) and annuli (dashed) geometries analyzed in section 3.3.2. . . . 40
3.7 The geometry used to create the maps of gas temperature and density. The disk is shown edge-on (blue pillbox), with cones opening vertically, and radially. 44
3.8 The radial and vertical density and temperature structure of g1536 and g15784 at $z = 0$. The colours represent gas temperature: $T < 10^4$ K in blue, $10^4 < T < 10^5$ K in green, $10^5 < T < 10^6$ K in red, and $T > 10^6$ K in magenta. 45
3.9 Rotation curves for g1536 disks, at $z = 0$ 47
3.10 Totation curves for g15784 disks, at $z = 0$ 47
3.11 The smoothed velocity contours for disk g1536 49
3.12 The smoothed velocity contours for disk g15784 50
3.13 g1536 star formation rates 53
3.14 g15784 star formation rates 53
3.15 Evolution of disk mass for g1536 55
3.16 Evolution of disk mass for g15784 56
3.17 Evolution of the radial temperature structure for g1536 60
3.18 Evolution of the total gas mass in radial bins for g1536 60
3.19 Evolution of the cold gas mass in radial bins for g1536 61
3.20 Evolution of the radial temperature structure for g15784 61
3.21 Evolution of the total gas mass in radial bins for g15784 62
3.22 Evolution of the cold gas mass in radial bins for g15784 62
3.23 Evolution of the inflow and outflowing gas mass in radial bins for g1536 . . 63

3.24 Evolution of the inflowing and outflowing gas mass in radial bins for g15784 63

3.25 The density profiles of the dark matter (solid) and the baryons (dotted) for disk g1536. The red, green, and blue lines represent the results for SB, BW, and NF respectively. 67

3.26 The density profiles of the dark matter (solid) and the baryons (dotted) for disk g15784. The red, green, and blue lines represent the results for SB, BW, and NF respectively. 68

3.27 In the left figure: gas particles, blue, are projected linearly forward (orange vectors) according to their velocity (black vectors). The larger the projection time step, the further they are projected to go. For the same projection time step, a particle with a larger velocity is projected to go further. In the right panel: we see that inflowing particles are red, and outflowing particles are blue. 71

3.28 Flux through a 30 kpc sphere for g1536 at $z = 0$ 73

3.29 Flux through a sphere for g15784 at $z = 0$ 74

3.30 The sheet is located 7 kpc above the disk, with a radius of 17 kpc. Hot and cold material is tagged as red or blue, and inflowing and outflowing material is shown in solid, or dot-dashed lines. 76

3.31 Flux through a sheet for g1536 at $z = 0$ 77

3.32 Flux through sheet for g15784 at $z = 0$ 78

3.33 A diagram of the annuli geometry. Material flowing into the annuli volume is shown with solid lines, while material moving out of the annuli volume is shown with dot-dashed lines. The filled grey region is not considered in the analysis, to avoid the bulge 79

3.34 Flux through annuli for g1536 at $z = 0$ 81

3.35 Flux through annuli for g15784 at $z = 0$ 81

3.36 Radial flux through annuli for g1536 at $z = 0$ 82

3.37 Radial flux through annuli for g15784 at $z = 0$ 82

3.38 Co-added flux through sphere for g1536. The input is averaged over $z = 0, 0.008, 0.016$ 83

3.39 Co-added flux through sphere for g15784. The input is averaged over $z = 0, 0.008, 0.016$ 84

3.40 Co-added flux through sheet for g1536. The input is averaged over $z = 0, 0.008, 0.016$ 85

3.41 Co-added flux through sheet for g15784. The input is averaged over $z = 0, 0.008, 0.016$ 86

3.42 Co-added flux through annuli for g1536. The input is averaged over $z = 0, 0.008, 0.016$ 87

3.43 Co-added flux through annuli for g15784. The input is averaged over $z = 0, 0.008, 0.016$ 87

3.44 Co-added radial flux through annuli for g1536. The input is averaged over $z = 0, 0.008, 0.016$ 88

3.45 Co-added radial flux through annuli for g15784. The input is averaged over $z = 0, 0.008, 0.016$ 89

A.1 For g1536_NF: The surface density of warm gass is plotted against height. An inner profile is fit in red, and an outer profile is fit in magenta. 95

A.2 For g1536_NF: The surface density of all gas plotted against radius. The break point, separating the outer and inner profiles, is used to define the edge of the disk. 96

A.3 For g1536_NF: The surface density of all stars plotted against radius. The red line is fit to the stellar bulge, while the magenta line is fit to the stars within the disk. 96

A.4 For g1536_BW: The surface density of cold (top) and warm gas (bottom) in g1536_BW is plotted against height. An inner profile is fit in red, and an outer profile is fit in magenta. 97

A.5 For g1536_BW: The surface density of all gas plotted against radius. The break point, separating the outer and inner profiles, is used to define the edge of the disk. 97

A.6 For g1536_BW: The surface density of all stars plotted against radius. The red line is fit to the stellar bulge, while the magenta line is fit to the stars within the disk. 98

A.7 For g1536_SB: The surface density of cold (top) and warm gas (bottom) in g1536_BW is plotted against height. An inner profile is fit in red, and an outer profile is fit in magenta. 98

A.8 For g1536_SB: The surface density of all gas plotted against radius. The break point, separating the outer and inner profiles, is used to define the edge of the disk. 99

A.9 For g1536_SB: The surface density of all stars plotted against radius. The red line is fit to the stellar bulge, while the magenta line is fit to the stars within the disk. 99

A.10 For g15784_NF: The surface density of warm gas is plotted against height. An inner profile is fit in red, and an outer profile is fit in magenta. 99

A.11 For g15784_NF: The surface density of all gas plotted against radius. The break point, separating the outer and inner profiles, is used to define the edge of the disk. 100

A.12 For g15784_NF: The surface density of all stars plotted against radius. The red line is fit to the stellar bulge, while the magenta line is fit to the stars within the disk. 100

A.13 For g15784_BW: The surface density of cold (top) and warm gas (bottom) in g15784_BW is plotted against height. An inner profile is fit in red, and an outer profile is fit in magenta. 101

A.14 For g15784_BW: The surface density of all gas plotted against radius. The break point, separating the outer and inner profiles, is used to define the edge of the disk. 101

A.15 For g15784_BW: The surface density of all stars plotted against radius. The red line is fit to the stellar bulge, while the magenta line is fit to the stars within the disk. 102

A.16 For g15784_SB: The surface density of cold (top) and warm gas (bottom) in g15784_BW is plotted against height. An inner profile is fit in red, and an outer profile is fit in magenta. 102

A.17 For g15784_SB: The surface density of all gas plotted against radius. The break point, separating the outer and inner profiles, is used to define the edge of the disk. 103

A.18 For g15784_SB: The surface density of all stars plotted against radius. The red line is fit to the stellar bulge, while the magenta line is fit to the stars within the disk. 103

List of Tables

1.1 A sub-set of ΛCDM cosmology parameters, as calculated by Planck Collaboration et al. (2015). 6

3.1 The parameters of the disks analyzed in this work. 33

3.2 The scale heights and radii of the gas for all disks. Errors correspond to the 95th% confidence interval of the fit parameters. 35

Abstract

Investigating the impact of stellar feedback algorithms on galactic evolution

by Samantha R Pillsworth

The numerical algorithm used to implement stellar feedback in a galactic simulation will strongly influence the resulting disk. Using two disks from the MUGS2 simulation suite (Keller et al., 2015), we study the morphologies of the disks at $z = 0$, the evolution of baryons and dark matter from $z = 4$ onward, and the accretion of gas onto the disk. Each disk is evolved with three different feedback algorithms: no feedback (NF), blastwave (BW), and superbubble (SB). We find that below a virial mass of $10^{12}\mathrm{M}_{\odot}$, SB feedback produces a denser, colder disk; prevents the formation of, or destroys, a bulge; removes the central velocity peak in the rotation curve, in good agreement with observed rotation curves; and, maintains a core in the central dark matter density profile. Above this virial mass, the binding energy of the halo is dominant, and the differences between disks evolved with BW and SB are less evident. Furthermore, we find that SB feedback fuels a cold gas reservoir in the halo. When the disk mass surpasses $\sim 4 \times 10^{10}\mathrm{M}_{\odot}$, this cold gas reservoir begins to be accreted. Thus SB disks show higher accretion rates at $0.17R_{\mathrm{vir}}$ of $\sim 2 - 4\mathrm{M}_{\odot}\mathrm{yr}^{-1}$. Again, these values are consistent with the observed accretion onto disk galaxies.

April 20, 2016

Chapter 1

Introduction

Hydrodynamics studies of galaxy formation arguably began in earnest with the work of Katz & Gunn (1991) and Katz (1992). Katz & Gunn (1991) studied the evolution of the collapse of a spherical, rotating, cloud of dark matter and gas that included initial density perturbations consistent with the cold dark matter (CDM) cosmology (Blumenthal et al., 1984). Galactic disks successfully formed in this collapse, but they were highly warped, contained central knots of dense material, and gas within them cooled so efficiently that the virial temperature was never reached. Katz (1992) included star formation and stellar feedback in an attempt to produce more reasonable facsimiles of the Milky Way. Unfortunately, this early attempt at including stellar feedback found that the energy returned to the gas through supernovae was radiated away almost immediately.

At a similar time, Navarro & Benz (1991) simulated the dynamical evolution of galaxy formation in a cosmological context. The internal structure of the galaxies were poorly resolved, but the same issue of over-efficient cooling was found. As dark matter haloes merged, so too did the condensed gas structures within them. During this merging process much of the angular momentum of the disk was transferred to the dark matter halo via dynamical friction. This resulted in disks that were far more compact than those observed.

To maintain angular momentum as well as prevent high levels of early star formation these simulations needed to include stellar feedback physics (see also White & Frenk 1991 for an semi-analytic model including feedback). Stellar feedback provides heating mechanisms that oppose gas cooling, allowing more realistic galaxies to be produced in simulations. The fact that these heating processes occur at sub-pc scales, considerably below the typical resolution in a galaxy formation simulation, means that there are many different algorithms which can be used to include stellar feedback, and each algorithm produces markedly different disks (see Thacker & Couchman, 2000 and Scannapieco et al., 2012) for reviews of the differences). Before we can discuss how the chosen feedback algorithm changes the evolution of a galaxy, we must introduce how galaxies are formed, the important physics in their evolution, and how that evolution can be modelled.

1.1 Galaxy Formation

Galaxies are composed of gas and stars which are directly observable, but there is also strong evidence of a third, unseen and massive, component: the rotation curves of galaxies, the plot of their circular velocity versus radii, are nearly constant rather than Keplerian in nature. Flatness in the rotation curve suggests the existence of more material than is observed directly (and so is non- or only weakly-interacting), but which can affect the gas and stars through gravitational forces (van Albada et al., 1985). However, it is important to note that prior evidence of dark matter existed in the literature as early as the 1930s. Zwicky (1933, 1937) analyzed the velocities of galaxies in the Coma cluster, and found that they were too high to be gravitationally bound if the only mass that existed was that which was observed. Similar analysis was done for the Virgo cluster by (Smith, 1936). Additionally, stars within the Andromeda galaxy were found to orbit too quickly to be bound by only the visible matter (Babcock, 1939).

Hoyle (1949) suggested that the rotation of galaxies came about because they were formed through the collapse of large volumes of diffuse matter. This was extended by Peebles (1969), who calculated the angular momentum a galaxy would have if it resulted from the collapse due to density perturbations in the "primeval" material (now known as dark matter). The angular momentum was converted to a measure of "oblateness" of a disk, which was found to agree, in general, with the Milky Way itself. At this point in the history of galaxy formation study, computational simulations became possible. This would have an impact on the overall development of the field as fully non-linear studies became possible.

Galaxy formation is most easily discussed in two stages. First, the collapse of dark matter - weakly interacting particles governed by gravity only; and second, the collapse of baryons to form the observable gas and stars of galaxies. In practice, these two processes are concurrent.

1.1.1 Collapse of DM Halos

If the collapse of dark matter haloes is purely gravitational then there must be some initial density imbalance, usually termed an over-density, to trigger it. This requires some initial density perturbation to exist in the Universe, creating the initial conditions for galaxy formation. These perturbations arise from inflation, as quantum fluctuations are inflated to macroscopic scales. The work of Peebles & Yu (1970) studied these perturbations in the context of the cosmic microwave background (CMB) which had recently been observed (Penzias & Wilson, 1965). The CMB provides evidence that at some point in the early Universe, matter and radiation were in thermal equilibrium. The physics of this coupled baryon-photon plasma, notably the viscosity and thermal conduction, influences the evolution of small perturbations (Coles & Lucchin, 2002).

Peebles & Yu (1970) numerically integrated the Boltzmann equation with respect to the distribution of photons in the early Universe before recombination. Starting with an

initial adiabatic density perturbation spectrum, the Boltzmann equation can be used to calculate how the density perturbations will change with time, treating in detail the regime of recombination, and finding a final perturbation spectrum after recombination has occurred. This analysis led to two characteristic masses: $\sim 10^{15} M_{\odot}$, a mass very similar to cluster masses; and $\sim 10^{11} M_{\odot}$, a characteristic galaxy mass. This suggests that possibly the large cluster-mass groups would fragment into smaller galaxy-sized objects, a theory today often referred to as 'top-down' galaxy formation. However the adiabatic perturbations assumed in the model proved to be in conflict with observations. Adiabatic perturbations affect all particles (baryon, dark matter, and radiation) because it is a net perturbation in the energy density. The alternative would be isocurvature perturbations, in which the relative number density of the particles are perturbed, essentially a perturbation in entropy. The adiabatic perturbations in matter necessary to form the characteristic masses found by Peebles & Yu (1970) would yield radiation perturbations much larger than the observational limits placed on the CMB, with an observed temperature of $3.5° \pm 1.0°$ K at the time (Penzias & Wilson, 1965).

Press & Schechter (1974) investigated galaxy formation from small scales to large scales: they considered the possibility that larger mass objects were in fact the result of interactions between smaller objects (i.e.. 'bottom-up' galaxy formation). The initial perturbations were allowed to be statistically random, described as 'grainy', with an initial spectrum of 'small' masses (the seed mass was approximately $10^{7} M_{\odot}$). As mass points condensed and became bound, they were considered to be single points again, with a total mass equal to the sum of the particles combined. The condensation proceeds to larger and larger scales until eventually the model gives no indication of the initial perturbations, and approaches a self-similar solution. The Press & Schechter formalism ultimately predicts the number of objects with a certain range of masses. The modelled range of galaxy masses was converted to a luminosity using the mass-to-light ratio for elliptical galaxies in order to plot a galaxy luminosity distribution. This function can be seen in figure 1.1 compared to

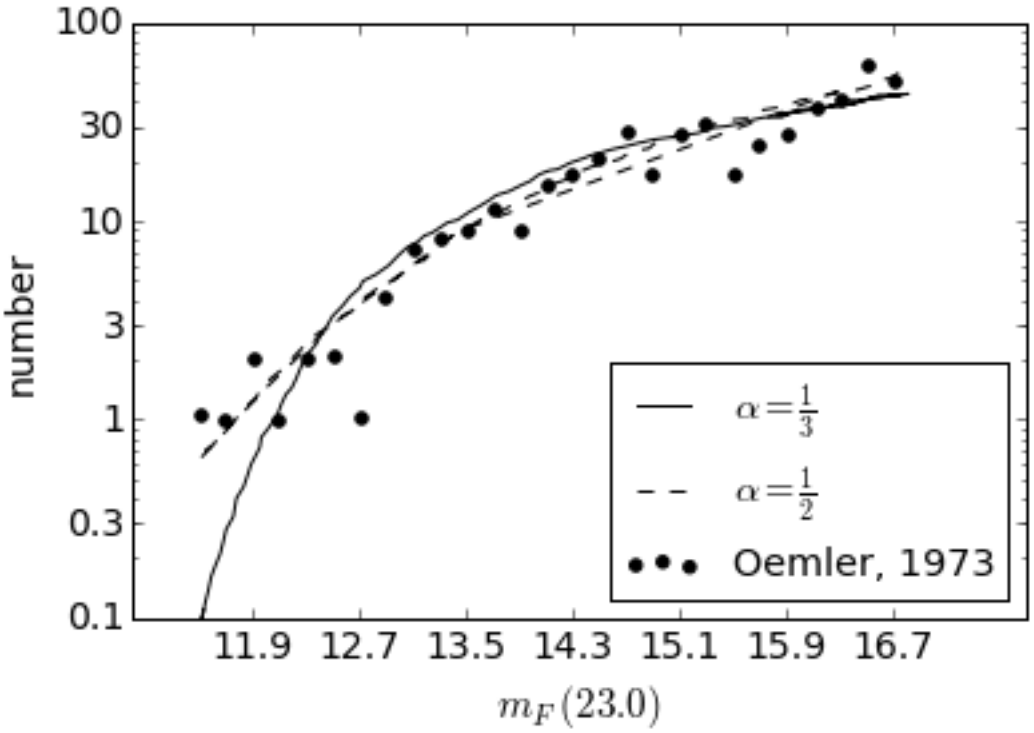

Figure 1.1: The luminosity distribution calculated by Press & Schechter (1974) shown as the dotted and dashed lines, compared to observations of the Coma cluster by Oemler (1973). Data replotted from Press & Schechter (1974)

observations of the Coma cluster (Oemler, 1973). The α parameter of the Press & Schechter model characterizes the relationship between mass variance and volume. There is equal agreement between the observations and both values of α suggesting general agreement between observations of clusters and the bottom-up formation model.

Work on galaxy formation in a cosmological context continued and the cold dark matter scenario became progressively more favourable (Peebles, 1982; Blumenthal et al., 1984). CDM is straight-forward to evolve in simulations because it is governed purely by gravity. Simulations allow us to follow the initial conditions governing dark matter all the way to the resulting present day universe (Davis et al., 1985; Barnes & Efstathiou, 1987; Lacey & Cole, 1994). The relative ease with which these simulations could be implemented allowed

Parameter	Planck 2015 value, 68% limits
H_0	67.74 ± 0.46
Ω_Λ	0.6911 ± 0.0062
Ω_m	0.3089 ± 0.0062
$\Omega_\mathrm{b}h^2$	0.02230 ± 0.00014

Table 1.1: A sub-set of ΛCDM cosmology parameters, as calculated by Planck Collaboration et al. (2015).

for studies of parameter spaces, narrowing our cosmological parameters to only those which produced universes reasonably matching present day observations.

For example, one requirement was the reproduction of observed large scale structure in the universe. Early N-body simulations found that CDM reproduced the correlation function, and filamentary structure in the Universe, showing clusters, superclusters, and voids (Davis et al., 1985). The CDM model became the strongly preferred cosmology when Smoot et al. (1992) announced measurements of the CMB power spectrum from the COBE maps. Scale invariant fluctuations with a Gaussian distribution were found which closely matched with the already assumed initial spectrum of density perturbations in the CDM cosmological model.

The results of the COBE maps have been improved upon by measurements taken with WMAP (Hinshaw et al., 2013), and Planck (Planck Collaboration et al., 2015). The 2015 results released by the Planck collaboration represent the most accurate set of cosmological parameters to date. Values of the Hubble constant, density parameters for dark energy, matter, and physical baryons are given in table 1.1.

1.1.2 Collapse of Baryons

The model of Press & Schechter (1974) is impressive in both its simplicity and predictive power, but it is not a complete model of galaxy formation. It does not include baryon physics, and does not discuss how a galaxy might form within a dark matter halo. Since baryons are what we observe, it is imperative that they be included in galaxy formation

models.

Such a model was developed by White & Rees (1978). They suggested that galaxies were formed in two stages. A cartoon representing this two-step formation process can be seen in figure 1.2. First, there was the dissipationless collapse of dark matter. As in Press & Schechter (1974), the dark matter condensed first on small scales, proceeding to larger and larger structures in a self-similar way. Second, baryons would fall into the gravitational potential well of the DM halos, and are heated by shocks along the way. Thirdly, gas at the centre of the halo would cool, collapsing further into a rotationally supported disk. Fourth, hot gas continues to cool and adds to the disk, increasing its radius. The gas cools radiatively, through bremsstrahlung radiation, recombination, and collisionally excited emission. The cooling time, $t_{cool} \sim E/\frac{\mathrm{d}E}{\mathrm{d}t}$ (where E is the thermal energy), of gas depends on all three of these processes (except at low temperatures, where bremsstrahlung is irrelevant). Since E is proportional to ρ, and dE/dt is proportional to ρ^2, we find that t_{cool} is proportional to ρ^{-1} – gas in denser environments will cool more quickly.

The cooling timescale will govern the range of sizes of galaxies found, as originally outlined in Rees & Ostriker (1977). The cooling argument which follows is very similar to that of Rees and Ostriker, although it was White & Rees (1978) who first considered gas cooling within a dark matter halo. t_{cool} can be constrained by considering it in relation to the dynamical time, t_{dyn} of the halo: defined as twice the turnaround time of the potential well (White & Rees, 1978). The turnaround time is defined as the time it takes for a perturbation to reach a point of maximum expansion and begin collapsing. If $t_{cool} \lesssim t_{dyn}$ then it is possible for the gas to cool, and begin forming stars. If $t_{cool} > t_{dyn}$ then the gas would remain pressure supported on timescales longer than it would take for the halo to undergo significant evolution (e.g. merge with another). A long cooling time would unavoidably prevent a luminous galaxy from forming at all. So it is necessary that $t_{cool} \lesssim t_{dyn}$. It is also necessary that the cooling timescale be less than the Hubble time or else luminous baryons would not be visible today. This cooling condition allows for baryons to cool such that they

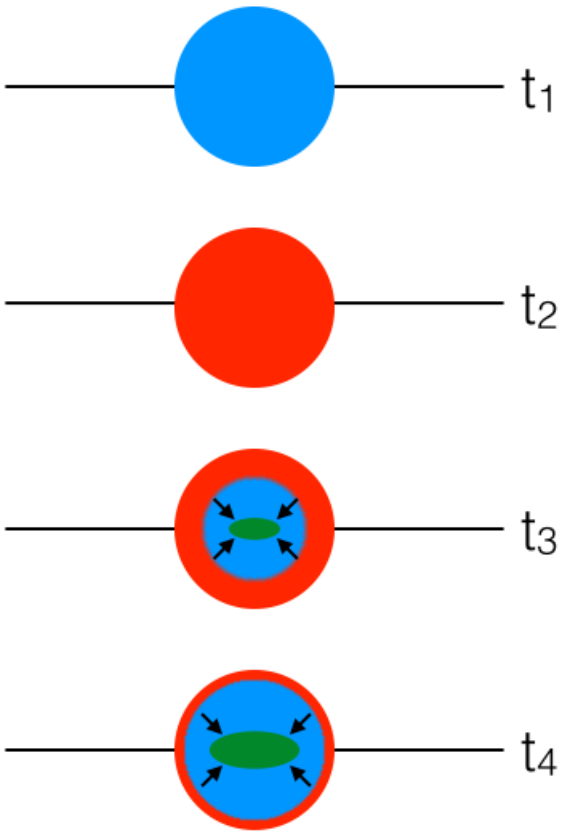

Figure 1.2: A cartoon showing the general two-step process of galaxy formation. Blue represents dark matter, red represents hot gas, while green represents cold gas. At t_1 is a cold dark matter halo. As baryons fall into the potential well, they are shock heated, t_2. The inner region of hot gas halo cools, forming a rotationally supported disk, t_3. The gas continues to cool and accrete onto the disk, t_4. Based on figure 8, Baugh,2006.

are robust enough not to be reheated in mergers.

The galaxy formation model of White & Rees (1978) defined an upper limit to galactic luminosity by imposing restrictions on the length of t_{cool}. This luminosity limit imposes a mass limit (by the mass to light ratio), and also a radius limit. The form and scaling of the volume density of galaxies as a function of their stellar mass (converted to a luminosity by a mass-to-light ratio) predicted is in good agreement with the expression derived by Schechter (1976). The inclusion of gas cooling in a galaxy formation model emphasized that a more complex treatment of baryon physics was necessary.

1.2 Galaxy Evolution

Galaxy formation is made more complex by not being simply the evolution of a closed system. There are continued mergers, star formation and stellar feedback, and possibly feedback from a central supermassive blackhole.

1.2.1 Star Formation

Star formation generally occurs in giant molecular clouds (GMCs). These clouds have masses $\sim 10^{5-6}\mathrm{M}_{\odot}$, diameters of ~ 50 pc, and average densities of $10^2\mathrm{cm}^{-3}$ (Blitz, 1993). In order that a GMC be gravitationally bound (while in equilibrium), it must obey the virial theorem: $2K = -U$, where K is the kinetic energy and U is the potential energy. These clouds have substructure, containing clumps, filaments, and cavities, and it is these structures which collapse to form stars, not the GMC itself. Therefore it is necessary that the substructure within the GMC be gravitationally bound as well (Williams et al., 2000).

These clumps and filaments are unstable to collapse when their mass exceeds the Jeans mass,

$$M_J \simeq \left(\frac{5kT}{G\mu m_H}\right)^{3/2}\left(\frac{3}{4\pi\rho_0}\right)^{1/2}, \tag{1.1}$$

where k is Boltzmann's constant, T is the temperature, μ is the mean molecular weight,

and ρ_0 is the initial density of the cloud (assumed to be constant throughout; Jeans (1902) Carroll & Ostlie, 2007). Although we are discussing the collapse of clumps within a cloud, these structures are still large enough that they form a cluster of stars, rather than a single star. Regions of the clump collapse down into pre-stellar cores, the precurser to a star. The particular geometry of this fragmentation is itself the subject of research (Klessen et al., 2000; Arzoumanian et al., 2011; Kirk et al., 2015). It is worth noting that poor simulation methods have further confused this subject. As outlined in Bate & Burkert (1997), it is necessary that the minimum resolvable mass in an SPH simulation be always less than the Jeans mass as otherwise artificial fragmentation can occur.

1.2.2 Stellar Feedback

While the scale on which a single star injects energy is small compared to a galaxy, the large number that exist and their grouped distribution make their impact non-negligible. Stars can affect the ISM in three ways: photoionization, stellar winds, and supernovae. Each mechanism has a distinct impact on the temperature, velocity, and density of the ISM. Stellar winds and supernovae can also impact the ISM metal and dust content.

Photoionization

A photon with energy above the ionization potential can collide with an atom and free a bound electron, with excess energy above the threshold value being transferred to the electron as kinetic energy. The process of photoionization is particularly important where the ISM is dense, such as the optically thick clouds in which stars are born. Photoionization plays a key role in disrupting these star forming clouds, which is theoretically described as a Strömgren sphere (Strömgren, 1939). A hot, young, star (particularly O-type stars) can ionize the hydrogen surrounding it through photoionization, up to the Strömgren radius.

Stellar Winds

Stellar winds are the flow of neutral or charged particles that are mostly driven from the upper atmosphere of a star. Depending on the type of star they originate from, stellar winds are driven by two different mechanisms.

Red giants, supergiants, and AGB stars have large radii, and consequently, their outer regions are only weakly bound by the gravity of the star. The high luminosity of these stars produces high radiation pressures which can easily overcome the gravitational forces in the outer regions of the star. Radiation pressure is capable of boosting material, which consists mostly of dust, above the escape velocity. These winds are categorized by their low velocities, but large quantities of material (Moaz, 2007).

Young, hot, O- and B-type stars are also capable of driving stellar winds. These winds are also referred to as line-driven winds, because it is the absorption and re-emission of photons by atoms which accelerates the wind. An atom will absorb a photon above the ionization energy needed to excite an electron, the remainder of the photon energy being transferred to the atom as kinetic energy. The life-time of the atom in this excited state is very short, the electron will quickly fall back to its original energy level and the photon is re-emitted. The atoms are accelerated outwards, which causes them to be Doppler shifted out of the core of their photospheric absorption line, and able to absorb continuum photons. This further increases the acceleration of the atom, driving very energetic stellar winds (Lamers & Cassinelli, 1999).

Supernovae

A supernova is the violent explosion of a star, caused either by core collapse in massive stars, or through runaway fusion processes in white dwarfs triggered by mass infall from a companion. While the physical phenomena leading up to events are different, the resulting supernovae proceed in much the same way. A supernova moves through essentially three

stages of evolution. These three phases are discussed in brief here, but see Reynolds (2008) for a more in-depth review.

Phase 1: Free Expansion The first phase of a supernova is known as the free expansion phase. The energy and density of the ejected material is so much greater than that of the ISM, it is as if the material exists in a vacuum. The supernova remnant (SNR) expands and sweeps up mass but has such high energy that the expansion is not significantly impacted. This stage lasts until the SNR has roughly doubled in mass.

Phase 2: Adiabatic Expansion The second phase is characterized by the adiabatic expansion of the SNR, and is sometimes referred to as the blastwave phase. The outer edge of the SNR is a moving shock. The post-shock material within the SNR is very hot at the centre (approximately 5×10^7 K), and the temperature decreases as the SNR expands and the shock loses energy. This creates a bubble hotter at the centre than at the edge. When the edge temperature drops below 10^6 K nuclei are able to capture free electrons, leading to a sudden cooling. The outer layer of the SNR radiates rapidly, and a thin cool shell of high density material forms around the SNR (the interior of which is commonly referred to as a bubble). This shell is typically formed after ~ 0.3 Myrs.

Phase 3: Snowplow In the third phase of the supernovae in which the SNR spends most of its lifetime the cold dense shell contains roughly half the mass of the SNR. The bubble continues to expand, sweeping up material from the ISM into the shell, much the same way a snowplow sweeps up snow. Thermal conduction evaporates mass from the inner edge of the cold shell into the hot bubble interior.

While individual events are confined to modest volumes, stellar feedback is important because of the sheer number of stars in a galaxy. It is the work of a population of stars that influences a galaxy's evolution. In comparison, for AGN feedback there is generally only

one supermassive black hole in a galaxy, yet it is powerful enough to disrupt its host.

1.2.3 AGN Feedback

An active galactic nuclei (AGN) is a galactic nuclei with a much higher luminosity that is typically expected of a galactic nucleus. Arguably, the first AGN was discovered by Schmidt (1963). A star-like object was discovered at $z = 0.158$ but which proved to be 10 times more luminous than the brightest galaxies. This quasi-stellar radio source, a 'quasar', was the first of its kind to be identified. Quasars were found to vary rapidly, with timescales ranging from hours to weeks. This indicates that they are small; causality requires that the quasar be only light-hours to light-months across in order for it to vary coherently (Peterson, 2001) . Other less luminous forms of AGN were found, and it is now generally accepted that all of these AGN are powered by the same mechanism: accretion onto a central supermassive blackhole (Kormendy & Richstone, 1995). Supermassive black holes are defined as black holes with masses above $10^6 M_\odot$. An accretion disk forms around the black hole, and it is physical processes driven by or interacting with the disk that are observable: winds or jets ejected from the disk, emission from the corona above the disk, and emission from the corona reflected off the accretion disk.

A significant body of research focuses on the study of how supermassive black holes co-evolve with their host galaxy. This is thought to be the case due to relationships existing between the black hole mass, velocity dispersion, and mass, of the galactic bulge (Gültekin et al., 2009). There are a number of theoretical attempts to explain this, for example, Begelman & Nath (2005) suggest that the relationships are caused by accretion. The central black hole radiates some amount of energy (dependent on its mass) while accreting gas. Infalling gas interacts with the black hole radiation, and is heated. This gives the gas an isothermal density profile and a velocity dispersion intrinsically related to the mass of the black hole. Recent work (reviewed by Kormendy & Ho, 2013) indicates that the relationship between a galaxy and its central black hole is more complicated.

At the present time the impact of an AGN on its host galaxy is not completely understood. For larger galaxies AGN feedback is possibly dominant over the effects of stellar feedback. In this thesis we focus on disk galaxies smaller than the giant ellipticals presumed to have been impacted by AGN feedback so, for these reasons, AGN feedback is not included in the models discussed.

1.2.4 Mergers

Galaxy masses grow via the hierarchical merging process. This process introduces dynamical features that would not be present in isolated systems, such as tidal tails. If the galaxies are of similar masses, the merger is considered major. In major mergers violent relaxation causes the potential energy distribution to broaden (strongly bound particles become more bound, while weakly bound particles gain enough energy to escape the galactic potential), and the amount of dark matter in the central regions to increase (Hilz et al., 2012). If the merging galaxy is small compared to the primary ($M_{sat}/M_{pri} \sim 0.1$), the size of the primary increases by tidally stripping the stars from the satellite. Minor mergers are thought to be primarily responsible for the growth of bulges in some disk galaxies (Aguerri et al., 2001; Hilz et al., 2012). Due to their non-linear nature, mergers require numerical calculations to be modelled in detail - semi-analytical models are limited by their lack of dynamical modelling. Simulations designed to explicitly study mergers can be set up, modelling two galaxies in isolation, examples of such simulations would be Toomre & Toomre (1972); Mihos & Hernquist (1994); Barnes (1992); Springel et al. (2005). A better motivated way to study mergers is to run a full cosmological study at low resolution, and then to run a high resolution simulation 'zoomed in' on the galaxy of interest (a common method today, an early example is Katz et al. 1994). Cosmological models allow mergers to occur 'naturally', through the gravitational forces arising between dark matter halos, and with statistical properties determined by the initial conditions.

Including stellar feedback, AGN feedback, and mergers would be necessary to model a

complete process of galactic evolution, along with the gas cooling discussed in section 1.1.2. Such a complete model is not tractable at this time, as it is not yet entirely understood *how* these processes change the evolution of their host. Studying their effects is more easily done in isolation. For this reason, we will focus on models of disk galaxies which include stellar feedback, but not AGN feedback.

1.3 Analytic and Semi-Analytic Modelling

Analytic and semi-analytic models implement the physics of galaxy formation phenomenologically. Equations defining star formation, stellar feedback, gas cooling, etc. are motivated, and a variety of parameters are set, according to observations. The galaxy luminosity distribution (Schechter, 1976; Blanton et al., 2001) for example, is observed and 'known' so a semi-analytical model could use the parameters defining the relation as input. The usefulness of analytic or semi-analytical models comes from their speed: any free parameters remaining in the model can be varied quickly and with relative ease (see Baugh 2006 for a review of semi-analytical modelling of galaxy formation). Large samples of galaxies can be quickly produced, with lower computational costs than would be required by direct numerical simulations.

Semi-analytical models do not directly solve the equations of hydrodynamics, and so they do not inherently model gas dynamics. Effects on the density, temperature, and velocities of gas from stellar feedback do not follow 'naturally' from first principles, but are varied as according to the feedback model. For example, White & Frenk (1991) required that their modelled galaxies match the observed luminosity density of the Universe, so the efficiency of supernovae (the amount of energy returned to the ISM) is set, such that the luminosity density function is reproduced. As numerical simulations have become more detailed, modern semi-analytical models can limit free parameters through their results as well (Makiya et al., 2015).

The work of White & Frenk (1991) is considered seminal as it highlighted the need for stellar feedback. Without feedback, gas clouds can cool on timescales as short as 1 Myr (the *cooling catastrophe*) leading to extremely high star formation rates at early times, and disks nearly depleted of gas at later times (Hopkins & Beacom, 2006). With the implementation of stellar feedback processes (supernovae), they showed that the cooling catastrophe could be avoided, with a star formation rate peaking at later times, in better agreement with the cosmic star formation history (Hopkins & Beacom, 2006).

Today, semi-analytical models and numerical simulations work together. Numerical simulations can provide new insight into galaxy formation by simulating directly gas dynamics and galaxy mergers. Semi-analytical models allow the fast study of vast parameter spaces, often making use of the results of numerical simulations, such as implementing merger trees (a tree-like structure which stores the merger history of a halo).

1.4 Simulations

Numerical simulations allow us to solve the fully non-linear equations of galaxy formation. Cold dark matter is collisionless, and so simulations without baryons can be modelled fairly straightforwardly. These N-body codes solve only for the gravitational forces between particles (Davis et al., 1985; Springel et al., 2005 are two notable examples of cosmological N-body simulations). Including baryon physics requires that the hydrodynamical equations of motion be solved.

These equations can be solved with two different methods. The first method is by modelling a fluid as a series of discrete particles, implementing different particle types for gas, stars, and dark matter. This is known as *Smoothed Particle Hydrodynamics* (SPH) (Lucy, 1977; Gingold & Monaghan, 1977). Each particle has a position, velocity, temperature, density, pressure and equations of motion and conservation must be solved (discussed further in section 2.1). The second method of galaxy modelling considers a fluid described

using a grid. Grid methods solve for the velocity, temperature, density, and pressure in each cell of the grid. While there are pros and cons to each method, all of the simulations discussed will be of the SPH variety, as the simulations we use were previously computed.

After the work of White & Frenk (1991) indicated that stellar feedback was a necessary inclusion, Katz (1992) included star formation and supernovae in SPH simulations of an isolated disk (as opposed to a cosmological model of a large number of disks), to investigate their effects on the formation of galaxies. The model implemented the following assumptions: (1) Stars formed with solar masses greater than $8M_{\odot}$ go supernova; (2) A supernova adds 10^{51} ergs to the surrounding ISM as heat, implemented in the SPH code by smoothing the thermal energy over the gas particles neighbouring the parent gas particle (the gas particle out of which the star particle was formed); (3) The supernova leaves behind a mass remnant of $1.4M_{\odot}$ (Chandrasekhar, 1931; Shu, 1982). Katz (1992) found that the energy of the supernova was radiated away quickly, before being able to affect the evolution of the galaxy; this is contrary to observations which indicate that the ISM responds rapidly to supernova (observations of SN 1987A suggest that a remnant was observed only a week after the event, Arnett et al. 1989). It did, however, remove dense knots of material that were prone to forming in the centres of disks when feedback was not implemented (Katz & Gunn, 1991). These dense knots were particularly visible in the circular velocity profiles, shown as a peak in velocity in the central region before flattening at larger radii. Observed rotation curves do not show a central peak, but a circular velocity which rises smoothly before stabilizing at its maximum value (Begeman et al., 1991; Rubin et al., 1980)

Stellar feedback due to supernovae can also be applied as a combination of thermal and kinetic energy in simulations. The kinetic energy acts by giving particles a 'kick', adding to their radial velocity (Navarro & White, 1993). When energy is returned to the ISM as predominantly kinetic the star formation rate is reduced; however, when returned as predominantly thermal energy there is very little effect on the host galaxy. This is due to the overcooling problem which plagues feedback governed by thermal energy, but which

does not impact kinetic feedback algorithms. This is a serious problem, as the qualitative properties of the disk change depending on how feedback energy is returned to the ISM. When cosmological simulations were run which did not include a heating mechanism from stellar feedback but did include radiative cooling, all gas clumped in the central core of the disk and was never able to be reheated (Navarro & White, 1994). The produced disks were substantially more compact than observed disks, again signalling that a heating mechanism is necessary to balance radiative cooling.

It should be noted that in the simulations discussed here, star formation and feedback is most often applied as a subgrid model. These processes occur on small scales compared to size of a galaxy, and cannot be resolved in simulations which study galaxies in their dynamic environment. Subgrid models apply physics which is below the dynamical resolution in a semi-analytical way. Star formation, for example, cannot be modelled explicitly, so a stochastic method is used in which a gas particle will produce a star particle with some probability (depending on local properties). The smoothing of feedback energy onto nearby gas particles is a subgrid model of a supernova, as the physical expansion of a blastwave cannot be solved directly at these resolutions.

Some simulations were done which avoided the over-cooling problem by returning supernovae feedback as only kinetic energy, and ignoring the thermal energy component entirely. Mihos & Hernquist (1994) returned a small fraction (10^{-4}) of the expected supernova energy to nearby particles as kinetic energy. Two smoothing lengths were used, so that nearby particles received more energy than those further from the star particle. The exact fraction of SN energy that was to be returned to the ISM was tuned to produce disks with reasonable scale heights. Variations in this fraction would not only produce disks which were too thick or too thin; the star formation would either become very spatially smooth, or it wouldn't provide enough support at all and the disk would fragment.

Evrard et al. (1994) ran cosmological simulations and found that cooling mechanisms were more efficient at higher resolution. Although they confirmed that disk formation was

a result of hierarchical clustering and cooling, the more efficient cooling mechanisms meant that there was too much cold gas clustered together at early times. This material could be diffused through a heating mechanism, but the problem of overcooling still remained: the resolution was not high enough to properly resolve temperature gradients and cold gas would almost immediately radiate away supernova energy rather than be dispersed by it. One possible solution to this problem was to limit the cooling by disabling the algorithm for a period of time following a supernova (Gerritsen, 1997) . This was effective in systems of low-mass dwarf galaxies, but larger hierarchical simulations at lower resolution were still largely unaffected by the inclusion of stellar feedback (Thacker & Couchman, 2000), unless the delay period of the cooling was extended (Thacker & Couchman, 2001).

Another solution to the problem of overcooling due to unresolved temperature gradients is to allow particles to have multiple phases, whose evolution is determined by models motivated by McKee & Ostriker (1977). Springel & Hernquist (2003) used particles which represented patches of the ISM; they were composed of hot ambient gas, cold collapsed clouds, and stars. The hydrodynamical equations are solved for the hot ambient gas. The supernova feedback heats the ambient hot phase and transfers mass from the cold cloud phase into the ambient hot phase. Radiative cooling causes material in the ambient hot phase to condense into cold clouds. These multi-phase particles allow for the feedback to be applied as heat, but without being radiated away immediately. Consequently, the galaxies produced have star formation rates which are comparable with the Kennicutt-Schmidt law: their star formation rate varies with gas density, following a power law function with index $n \simeq 1.4$ (Schmidt, 1959; Kennicutt, 1998). Unfortunately, modelling the ISM with these multi-phase particles coupled the hot and cold mass, preventing hot gas from being ejected from the disk in winds or outflows.

Many of the feedback algorithms discussed so far have been largely phenomenological, adding supernovae energy to the ISM, and disabling cooling for a user-defined period of time. Stinson et al. (2006) proposed a feedback recipe which disabled cooling for a time

roughly equal to the lifetime of a blastwave remnant, for particles within the radius of a typical blastwave (further discussed in Section 2.3). This algorithm produces an isolated Milky Way-like galaxy which agrees with the observed Kennicut-Schmidt law. The feedback algorithm was then applied in a cosmological context (Stinson et al., 2010). These galaxies suffer from similar problems as already discussed: there is a high concentration of material at the centre of the galaxy, which can be seen in centrally-peaked velocity profiles, and high bulge-to-disk ratios.

Implementing feedback such that it will produce galaxies consistent with observed populations has proven to be difficult. Only recently has a feedback algorithm been proposed which can accurately produce rotation curves, without a central peak, for Milky Way sized galaxies in a cosmological context (Keller et al., 2014, 2015). This method removes the problem of overcooling by allowing gas particles to take on both a hot and a cold phase, while still allowing for hot outflows by not requiring that particles be multi-phase. Rather than smoothing the energy injected into the ISM by the SNe over the smoothing length, a distance without physical interpretation, the expansion of the supernova remnant, and thus the injected energy, is governed by an algorithm solving for thermal conduction, and a sub-grid model describing mass evaporation (discussed in further detail in section 2.4).

Chapter 2

Methods

This thesis focuses on analyzing simulations that were performed by Keller et al. (2015). These SPH simulations were run using an updated version of the code GASOLINE (Wadsley et al., 2004). Three different models for feedback were used: no feedback, blastwave feedback (Stinson et al., 2006), and superbubble feedback (Keller et al., 2014).

2.1 Smoothed Particle Hydrodynamics

A description of SPH was given briefly in the introduction but requires a more thorough explanation. This section will provide a brief summary of the SPH method employed. This summary is based on the much more thorough review of Price (2010).

Smoothed particle hydrodynamics provides a framework to interpolate the position of Lagrangian particles onto continuous fluids. The first step of any SPH implementation is to interpolate a density field based upon the particle field. The basic equation for this smoothing at the location of particle a is:

$$\rho\left(r_a\right) = \sum_{b=1}^{N_{neigh}} m_b W_{ab}, \tag{2.1}$$

where $\rho(r)$ is the density field, b is the particle index, N_{neigh} is the number of particles over which to smooth, m_b is the mass of particle b, and W_ab is a weighting function between particles. W takes as input the distance between the two particles and their smoothing lengths, a scale parameter which sets the resolution length.

From the SPH implementation of the density equation, the momentum and internal energy equations can be derived:

$$\frac{d\vec{v}_a}{dt} = -\sum_{b=1}^{N_{neigh}} m_b \left(\frac{P_a}{\rho_a^2} + \frac{P_b}{\rho_b^2} + \Pi_{ab} \right) \nabla_a W_{ab}, \tag{2.2}$$

$$\frac{du_a}{dt} = \frac{P_a}{\rho_a^2} \sum_{b=1}^{N_{neigh}} m_b (\vec{v}_a - \vec{v}_b) \cdot \nabla_a W_{ab}. \tag{2.3}$$

These equations depend on the particle pressure, P, density, mass, and weighting function. The momentum equation further includes an artificial viscosity term, Π. This term artificially increases the viscosity, which is necessary to computationally model transition zones around shocks.

The weighting function, W, also called the smoothing kernel, has four properties. First, when integrated over the entire volume, the smoothing function must go to unity. This requirement comes from the conservation of mass, $\int \rho dV = \sum_{b=1}^{N_{part}} m_b$. Second, it must be a positive, monotonically decreasing (with relative distance) function with smooth derivatives (that is, the second derivative must be continuous). Third, it must be isotropic about $r - r_b$ such that $W(r - r_b, h) = W(|r - r_b|, h)$. Finally, it must be relatively flat in the centre, so that small changes in particle position do not drastically affect the density field.

One such function that meets all of these requirements in the Gaussian function. There is a drawback to the Gaussian however: it is infinite in extent. Using a Gaussian as the smoothing kernel would require that each particle be smoothed over the entire simulation domain. This is computationally expensive, and needless: at large distances the particle would contribute negligibly to the density. Splines are a good alternative; the most simple

of which is the cubic spline. It has continuous first and second derivatives, but goes to zero away from the particle.

The smoothing kernel, then, can be written as $W(|r-r'|,h) \equiv \frac{1}{h^d} w(q)$ where

$$w(q) = \sigma \begin{cases} \frac{1}{4}(2-q)^3 - (1-q)^3, & 0 \leq q < 1 \\ \frac{1}{4}(2-q)^3, & 1 \leq q < 2 \\ 0. & q > 2 \end{cases} \tag{2.4}$$

In the above equation, $q = \frac{|r-r'|}{h}$, $d = [1,2,3]$, and $\sigma = [\frac{2}{3}, \frac{7}{10\pi}, \frac{1}{\pi}]$ depending on the dimension of the problem.

The smoothing length sets the resolution length of a particle. It is desirable to resolve both dense and sparse regions evenly, so it follows that the smoothing length should depend on the local number density. The gas particles considered here are of roughly the same mass, and so the smoothing length can be chosen such that it encloses a constant number of particles. The distance to the 64 nearest neighbour of each particle was defined to be the smoothing length of that particle.

2.2 GASOLINE2

GASOLINE, and its recent update GASOLINE2, is an SPH based code, with a K-D tree gravity solver, originally developed by Wadsley et al. (2004); Keller et al. (2014). It includes photoelectric heating of dust grains, photoionization due to UV radiation, and cooling due to hydrogen, helium, and metals. The code utilizes an internal energy equation which conserves energy exactly and closely conserves entropy. Shen et al. (2010) updated the code to include a sub-grid model for the turbulent mixing of metals and energy. Keller et al. (2014) introduced GASOLINE2 (a complete paper describing the updated code is forthcoming). A modified pressure force was implemented (Ritchie, 2001), reducing forces

due to artificial surface tension at density discontinuities, and allowing for better modelling of Kelvin-Helmholtz instabilities.

The runs used herein applied three different methods of stellar feedback, but made use of the same star formation algorithm. Stars are allowed to form from converging flows of gas with temperatures less than 1.5×10^4 K, and densities equal to 9.3 cm^{-3} (the maximum density allowed by the softening parameter). The softening parameter, ϵ, defines the minimum allowed distance between two particles. This is necessary to prevent gravity calculations from going to infinity. In GASOLINE, $\epsilon = 312.5$pc. The star formation rate density, $\dot{\rho}_*$, is governed by the local free-fall time of the gas (the time for gravitational collapse, $t_{ff} = \sqrt{\frac{3\pi}{32G\rho}}$):

$$\dot{\rho}_* = c_* \frac{\rho_{gas}}{t_{ff}}, \tag{2.5}$$

where the efficiency parameter is set, $c_* = 0.1$.

Type II supernovae, in the runs with stellar feedback, are assumed to occur for stars with masses in the range $8 - 40 M_\odot$. The number of stars formed in this range is determined by the initial mass function; in these simulations a Chabrier (2003) IMF. If each supernova returns 10^{51} ergs of energy to the ISM, then the Chabrier IMF dictates that 10^{49} ergs are returned per solar mass. Type I supernovae, distinguished from type II by their lack of hydrogen lines, are not included in models. Type Ia SNe, those resulting from a degenerate white dwarf in a binary system, occur much later in the lifetime of a star, when the dense ISM around it would have already dissipated. While these SNe return a significant amount of energy, they occur rarely compared to type II SNe and are physically less important in disrupting dense gas. Type Ib and Ic SNe do occur in star forming regions, but after the star has already lost its outer hydrogen envelope. These are likely evolved from very massive stars, such as Wolf-Rayet stars, which are also very rare compared to those stars which will result in a type II SNe.

The blastwave feedback method employed in these simulations was first discussed by

Stinson et al. (2006), and later employed by Stinson et al. (2010, 2013). Stinson et al. (2013) also included early stellar feedback: winds and radiation driven by young stars before any supernova would have happened. The intent of this feedback is to disrupt the dense molecular star forming gas; seeing as dense molecular gas is not resolved in these particular simulations, there is no need for early stellar feedback to be implemented to disrupt it.

2.3 Blastwave Feedback

Blastwave feedback, as utilized here, was first presented by Stinson et al. (2006). It was so named because it took the blastwave solution presented by McKee & Ostriker (1977) as input: cooling was turned off only for those particles which fell within the radius associated with a blastwave, for an amount of time consistent with the lifetime of the cold shell around the blastwave. In this algorithm energy is returned to the ISM through smoothing, in the same way as Katz (1992).

The energy, metals, and mass returned to the ISM are first smoothed over the gas particles nearest to the star, following an SPH type prescription. For example, the energy that a gas particle receives from a supernova explosion will be

$$\Delta E_{\mathrm{SN,i}} = \frac{m_i W(|r_i - r_s|, h_s) \Delta E_{\mathrm{SN}}}{\sum_{j=1}^{N} m_j W(|r_j - r_s|, h_s)}. \tag{2.6}$$

As in section 2.1, W represents the smoothing kernel (a cubic spline), m is the mass of the gas particle, and E_{SN} is the total energy of the supernova. h_s is the smoothing length of the star: the distance to the 32^{nd} gas particle away from the star.

Immediately after a supernova, the cooling algorithm is turned off for a short period of time (a few tens of Myrs). The particles, and the length of time, for which cooling is turned off is usually a user-defined parameter. Stinson et al. (2006) propose that these parameters should be set by treating the returned feedback as a blastwave. The maximum radius of a

blastwave was shown by McKee & Ostriker (1977) to be

$$R_E = 10^{1.74} E_{51}^{0.32} n_0^{-0.16} \tilde{P}_{04}^{-0.20} \text{ pc.} \tag{2.7}$$

The parameters are defined thus: $E_{\rm SN} = E_{51} 10^{51}$ ergs, n_0 is the ambient hydrogen density, and $\tilde{P}_{04} = 10^{-4} P_0 k^{-1}$ where P_0 is the ambient pressure and k is Boltzmann's constant. All particles within this radius, up to an arbitrary maximum of 32, have their cooling disabled. The amount of time this cooling is disabled can be set to the amount of time the hot, low density, shell will survive:

$$t_{max} = 10^{6.85} E_{51}^{0.32} n_0^{0.34} \tilde{P}_{04}^{-0.70} \text{ years.} \tag{2.8}$$

With these two equations, the details of disabled cooling are set analytically.

In the Stinson et al. (2006) blastwave feedback algorithm, small amounts of energy were returned to the ISM during every feedback timestep, resulting in the calculation of small blastwave radii and short lifetimes. Knowing that supernovae in a single stellar population will combine into superbubbles, Stinson et al. (2010) implemented a stochastic method to determine whether feedback energy was released, allowing energy to accumulate over many feedback timesteps and form larger blastwaves.

The amount of energy returned to the ISM during a feedback timestep, $N_{\rm ESN}$, is

$$N_{\rm ESN} = \text{floor}\left(\frac{N_{\rm SNII}}{N_{\rm SNQ}}\right) + \begin{cases} 0, & p \leq r \\ N_{\rm SNQ}, & p > r \end{cases} \tag{2.9}$$

where $N_{\rm SNII}$ is the number of SNe calculated to explode during the feedback timestep, $N_{\rm SNQ}$ is the 'SN quantum', the number of supernova required per feedback release (set to 20 SNe), r is a random number, and p is the probability that energy will be released. The probability

is calculated using $N_{\rm SNQ}$ and $N_{\rm SNII}$ such that

$$p = \frac{N_{\rm SNII} \bmod N_{\rm SNQ}}{N_{\rm SNQ}} \tag{2.10}$$

2.4 Superbubble Feedback

This method was initially described by Keller et al. (2014). Its motivation is to correctly model the impact of multiple shells merging in the ISM and the physics that is necessary to follow these processes. The feedback method is based on three phenomena that account for superbubble formation, reduce the number of parameters set, and prevent overcooling.

Energy from supernovae is deposited into the gas particle nearest to the star at a rate of 3×10^{38} ergs $\mathrm{s}^{-1}\mathrm{M}_{\odot}^{-1}$. Star particles are representative of stellar populations, and so releases energy beginning 4 Myrs after formation, until 30 Myrs after. This is the expected lifetimes of OB-type stars of a range of masses expected to explode as type II supernova. These lifetimes and rates result in the expected 10^{51} ergs of energy released per supernova.

It is important to note that the energy is not smoothed over a number of gas particles. Particles receive feedback energy through the thermal conduction algorithm, and are incorporated into the bubble through stochastic mass evaporation. These algorithms replace the BW feedback method of distributing energy and turning off cooling for particles within a certain radius.

2.4.1 Thermal Conduction

The process of thermal conduction maintains a uniform hot temperature in the interior of superbubbles. Heat is transported down temperature gradients, by electrons, in an ionized gas. The heat flux can be a complicated calculation, unless the gradient becomes steep when compared with the mean free path of the electrons. Material making up the shell of the bubble has a temperature of $T_{\rm shell} < 100\mathrm{K}$, and a density of $\rho \approx 10\mathrm{cm}^{-3}$. This is

compared to the material inside the bubble, with a temperature of $T_{\rm interior} \sim 10^6$K and a density of $\rho \approx 10^{-3}{\rm cm}^{-3}$. This is a very steep temperature gradient, so the heat flux becomes *saturated*, and depends only on the density, temperature, and thermal velocity of the electrons in the medium (Cowie & McKee, 1977), such that:

$$\mathbf{Q} = \nabla \left(\frac{3}{2} n_e k_B T_e v_e \right). \tag{2.11}$$

When the temperature gradient is not steeper than the mean free path of electrons (the scale length of the temperature gradient is larger than the mean free path of the electrons) the heat flux depends on a conduction coefficient and the temperature gradient, such that $\mathbf{Q} = -\kappa \nabla T$. The conduction coefficient is well-approximated by $\kappa(T) = \kappa_0 T^{5/2}$, where $\kappa_0 = 6.1 \times 10^{-7}$erg s^{-1} K$^{-7/2}$ cm^{-1}. This approximation only applies in the absence of magnetic fields.

2.4.2 Mass Evaporation

Conservation of energy requires that a heat flux into a cold cloud is balanced by a mass flux out of the cold cloud (Cowie & McKee, 1977). This mass flux is the dominant process governing what gas particles are affected by feedback, operating at the junction between hot bubble interior and cold bubble shell. As this boundary is unable to be resolved, mass evaporation is applied as a sub-grid model. The amount of mass flowing into a bubble with some interior temperature T, according to Mac Low & McCray (1988), is,

$$\frac{dM_b}{dt} = \frac{4\pi\mu}{25 k_B} \kappa_0 \frac{\Delta T^{5/2}}{\Delta x} A, \tag{2.12}$$

where A is the bubble surface area, and Δx is the thickness of the outermost hot layer of particles. This hot layer is defined as the particles with no other hot particles within 45° of the vector to the centre of mass of their cold neighbour. The surface area of the

bubble depends on the radius of the superbubble. It would be computationally expensive to calculate the radius for each mass evaporation time step; it would be better if each particle could somehow estimate the bubble radius. Keller et al. (2014) empirically found that each particle could estimate its surface area contribution as $A_i = \frac{6\pi h^2}{N_{hot}}$, where N_{hot} is the number of hot neighbours for the particle.

The mass evaporation is applied stochastically. The probability that a particle with cold mass m will be converted into a hot particle over a time period Δt is,

$$P_{evap} = \frac{dM_b}{dt}\frac{\Delta t}{m}. \tag{2.13}$$

This prevents partial particle evaporation from occurring, which would also be susceptible to overcooling. Each hot particle is capable of evaporating N_{evap} cold particles. The thermal energies of the hot particle and the evaporated cold particles is averaged, and the cold particles are spontaneously added to the bubble interior.

Similar to the heat flux, the mass flux is also capable of being saturated. In this case, the mass flux is approximated by

$$\frac{dM_{sat}}{dt} = 17\rho c_s h^2. \tag{2.14}$$

2.4.3 Multi-Phase Particles

While the blastwave feedback method applies a cooling turnoff to prevent overcooling, it is also possible to prevent overcooling by allowing particles to 'store' feedback energy in a second phase, kept in pressure equilibrium. Particles enter the multiphase state if they are given energy from feedback, and if their energy is less than 10^5 K. The mass and energy of the two phases are combined to find mass and energy of the total particle:

$$m = m_{hot} + m_{cold} \qquad E = u_{hot}m_{hot} + u_{cold}m_{cold}, \tag{2.15}$$

where m_{hot}, m_{cold}, u_{hot}, and u_{cold} are the mass and specific energy of the hot and cold phases of the particle.

The two phases will be in pressure equilibrium with one another, so the total pressure of the particle can be used to find the hot and cold component densities:

$$\frac{P}{\rho} = \frac{(\gamma - 1)E}{m} \tag{2.16}$$

$$\rho_{cold} = \frac{P}{(\gamma - 1)u_{cold}} \qquad \rho_{hot} = \frac{P}{(\gamma - 1)u_{hot}} \tag{2.17}$$

Work on the particle is shared between the two phases, weighted by their energy respective to the total energy of the particle. This allows each phase to maintain constant entropy if the phase density changes (ignoring the processes of heating and cooling).

Mass evaporation allows for a mass flux between the cold and hot phases of the particle. It is calculated in a manner consistent with equation 2.12. The equation for mass flux does differ slightly when used for phases of a single particle, compared to flux between particles. A fraction of the cold phase is evaporated each time step,

$$\frac{dM_b}{dt} = \frac{16\pi\mu}{25k_B}\kappa_0\frac{\Delta T_{hot}^{5/2}}{h} \tag{2.18}$$

The multiphase state of a particle lasts until the cold phase is entirely evaporated into the hot phase, or until the hot phase has cooled below 10^5 K.

2.4.4 Initial Conditions

The MUGS2 initial conditions are the same as those used for the original MUGS simulations, outlined in Stinson et al. (2010). The initial conditions of these simulations can be thought of in two parts: the definition of the cosmology which governs the simulation, and the initial properties of the particles within the simulation. Here a *Wilkinson Microwave Anisotropy Probe Three* ΛCDM cosmology is used, with $H_0 = 73\mathrm{kms}^{-1}\mathrm{Mpc}^{-1}$, $\Omega_\mathrm{m} = 0.24$, $\Omega_\Lambda = 0.76$,

$\Omega_{\rm bary} = 0.04$, and $\sigma_8 = 0.76$.

To create the particle initial conditions, a low-resolution N-body simulation containing only 256^3 dark matter particles (no baryon physics) is evolved to $z = 0$ for a cosmological cube with a side length of $50h^{-1}$ Mpc. At $z = 0$, a friends-of-friends algorithm (Davis et al., 1985) is used to find virialized haloes with masses between $5 \times 10^{11}{\rm M}_\odot$ and $2 \times 10^{12}{\rm M}_\odot$, and which are also at least 2.7 Mpc away from their nearest neighbour in the same mass range. Of the 276 possible haloes which met these two requirements, 9 were chosen to be simulated at a higher resolution.

The simulation domain for these 'zoomed-in' runs was found by tracing all of the dark matter particles within 5 virial radii of the halo back to their original positions. These original positions mark the boundaries of the high resolution domain, which is populated with dark matter particles on a regular lattice with an effective resolution of 2048^3. Outside of this domain, a spherical region with a radius of 1.2 times the maximum radius of the high resolution region is populated with dark matter particles with an effective resolution of 512^3. There are three more spherical regions evenly spread in radius with resolutions of 256^3, 128^3, and 64^3, filling the $50h^{-1}$ Mpc^3 box. All the particles are perturbed using the Zel'dovich approximation (Zel'dovich 1970), and the simulation is again run to $z = 0$.

After this second run, any dark matter particles within three virial radii at $z = 0$ have a fraction of their mass converted to a gas particle at the initial position of the dark matter particle, with a mass corresponding to the cosmic baryon fraction, $\Omega_{\rm b}/\Omega_{\rm m}$. The gas particles are again perturbed using the Zel'dovich approximation. This particle configuration, with a low resolution perturbed grid of dark matter particles at the edges moving to a high-resolution region in the centre of the box containing both dark matter and gas particles defines the initial conditions for a simulation to be run including baryon physics. Dark matter particles in the high resolution centre have a mass of $1.1 \times 10^6{\rm M}_\odot$, and gas particles are initialized with a mass of $2.2 \times 10^5{\rm M}_\odot$. Star particles are created during the simulations with masses of $6.3 \times 10^4{\rm M}_\odot$. All particles use a gravitational softening length of 312.5 pc.

Chapter 3

Results

3.1 $z = 0$ Galaxy Morphology: Comparing the Results of Different Feedback Mechanisms

3.1.1 The Density Structure of the Gas Disk

Feedback algorithms return energy to the ISM, thus impacting its temperature and density structure. It is therefore expected that different feedback algorithms will produce different morphologies. A basic overview of the parameters of each disk at $z = 0$ is given in table 3.1.

The gas density is an important object of analysis because it will allow us to compare the structure of the disk which results from different feedback algorithms. The disk structure can be analyzed quantitatively by calculating the scale heights and radii associated with the disk, and visually through maps of the smoothed density field.

The scale heights and radii have been calculated by fitting an exponential function to the gas density of the form: $\rho(x) = ae^{-x/x_0}$, where a is the normalization and x_0 is the scale height or radius. In all cases there is a break point, beyond which a second exponential function is required to achieve a good fit. The values of all scales are given in table 3.2. An

Disk	Number of Particles			Softening	Virial Radius	Virial Mass	Disk Mass	Bulge Mass
	DM	Gas	Stars	Length (kpc)	(kpc)	($10^{11}M_{\odot}$)	($10^{11}M_{\odot}$)	($10^{11}M_{\odot}$)
g1536_NF	3021673	815433	368877	0.3125	173	6.54	0.68	0.44
g1536_BW	3021673	906745	375437	0.3125	173	6.63	0.65	0.37
g1536_SB	3021673	1066814	133091	0.3125	174	6.67	0.41	0.05
g15784_NF	5254617	940743	643643	0.3125	219	13.1	1.26	0.88
g15784_BW	5254617	974067	908407	0.3125	218	12.8	1.40	0.78
g15784_SB	5254617	992105	1044140	0.3125	219	1.31	1.56	0.86

Table 3.1: The parameters of the disks analyzed in this work.

example of the fitted histograms are given for g1536_BW, shown in figures 3.1 and 3.2.

These values can be compared with observations to give a general idea of how reasonable these simulated galaxies. The stellar scale radii all fall within the range of the estimated values used when modelling the Milky Way of 3 to 5 kpc (Robin et al., 2003). The cold gas inner scale heights of g1536_BW and g1536_SB, both $\approx$ 1kpc, are larger than the $0.1 - 0.6$ kpc observed in galaxies of similar masses in The HI Nearby Galaxy Survey (THINGS) (Bagetakos et al., 2011), while g15784_SB and g15784_BW, with cold gas scale heights of $\approx$ 0.4kpc, are a good match. This indicates that both of the smaller disks evolved with feedback are more vertically extended than observations suggest. Material hotter than 10^4 K is fit to exponentials with much larger scale heights. In general the inner scale heights of warm material are in good agreement with the Milky Way value of 2 kpc (Kalberla & Kerp, 2009), except for g1536_SB. g1536_SB does not show a distinct population of warm gas in the disk, separate from the hot circumgalactic medium (CGM) above the disk. This hot halo material is fit with scales listed as the outer warm scale height. To emphasize, these heights are associated with the CGM and not the disk.

In all disks the surface density of all gas components is constant with radius, within a ring around the disk, see figures in appendix A. In figure 3.2 this is true between 3 and 16 kpc. HI is observed to have a constant surface density in disks with similar circular velocities to the Milky Way, and the simulated galaxies considered here, as seen in Bigiel et al. (2010), figure 2 (circular velocity information on THINGS galaxies can be found in Walter et al., 2008). Furthermore, a flat HI surface density profile is in good agreement with the semi-analytical model of the Milky Way implemented by Wolfire et al. (2003). In the radial plot, we consider the surface density of gas of all temperatures, and in the central ring this density is dominated by cold material, HI and H_2. The surface densities increase in the central region, where the density of ionized hydrogen dominates, this can be further seen when examining the temperature and density in tandem, in section 3.1.2.

Disk	Cold Gas Scale Heights, kpc		Warm Gas Scale Height, kpc	Gas Scale Radii, kpc			Stellar Scale Radii, kpc
	Inner	Outer	Inner	Inner	Outer	Break Radius	Outer
g1536_SB	1.1 ± 0.1	4.1 ± 0.4	8 ± 1[†]	15 ± 4	1.7 ± 0.1	12.5 ± 0.25	3.1 ± 0.1
g1536_BW	0.94 ± 0.08	1.9 ± 0.1	1.9 ± 0.4	14 ± 2	1.70 ± 0.07	16.0 ± 0.25	3.5 ± 0.1
g1536_NF	N/A[‡]	N/A[‡]	0.32 ± 0.1	N/A[‡]	2.1 ± 0.2	8.75 ± 0.25	3.1 ± 0.3
g15784_SB	0.40 ± 0.05	1.9 ± 0.1	3.0 ± 0.6	12 ± 1	1.7 ± 0.1	16.5 ± 0.25	2.3 ± 0.1
g15784_BW	0.44 ± 0.04	1.16 ± 0.06	1.8 ± 0.1	30 ± 10	1.8 ± 0.2	16.75 ± 0.25	2.99 ± 0.09
g15784_NF	N/A[‡]	N/A[‡]	0.28 ± 0.08	N/A[‡]	1.4 ± 0.1	12.75 ± 0.25	4.4 ± 0.9

Table 3.2: The scale heights and radii of the gas for all disks. Errors correspond to the 95th% confidence interval of the fit parameters.

[†]associated with the CGM and not the disk

[‡]no cold gas in NF models

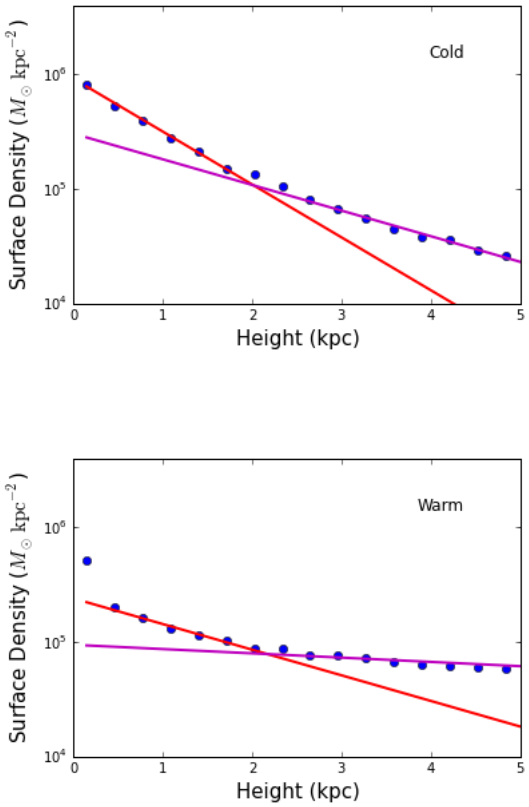

Figure 3.1: The surface density of cold (top) and warm gas (bottom) in g1536_BW is plotted against height. An inner profile is fit in red, and an outer profile is fit in magenta.

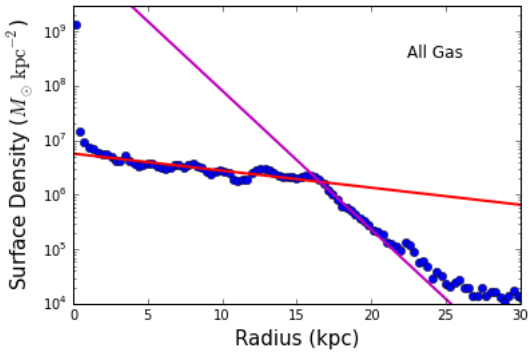

Figure 3.2: The surface density of all gas in the disk of g1536_BW plotted against radius. The break point, separating the outer and inner profiles, is used to define the edge of the disk.

The side-on and face-on density fields, seen in figures 3.3-3.6 are calculated using the smoothing routine discussed in section 2. To develop an understanding of the structure of a galactic disk, without the complications of stellar feedback, we discuss first the density fields of disks evolved in its absence. These disks are thin, with scale heights of only 0.37 and 0.28 kpc, for g1536 and g15784 respectively. These scale heights are calculated with warm material, as cold material does not exist within the disk. They are also truncated radially, as marked by a sharp drop-off in density. Defined as the location of the break point between the two exponential fits to the surface density, the NF disks extend to 8.5 and 12.75 kpc respectively. These disks have small pockets of material with densities above 10^8 $M_\odot$ kpc^{-2}, but are dominated by material with densities between 10^7 and $10^{7.5}$ $M_\odot$ kpc^{-2}. The region above the disk (seen in the side-on density fields, figures 3.4 and 3.6) contains material with densities less than 10^7 $M_\odot$ kpc^{-2}, and the density progressively lowers with distance.

Disks without feedback differ from those evolved with feedback, through two mechanisms. First, without feedback to heat gas and increase turbulence, stars form very rapidly. Disks evolved without feedback show very little dense gas because dense gas will very quickly form stars. Second, feedback drives outflows which eject material from the disk. The lack of these outflows is the primary cause of the thin, and truncated disks seen at $z = 0$.

We next analyze the changes which arise through the inclusion of feedback. As would be expected, the disks evolved with stellar feedback are larger than those evolved without, in both the radial and vertical directions. Disks evolved with feedback have radial extents ranging from 12.5-16.5 kpc (defined as the location of the break point in the radial gas density profiles). Their scale heights range from 0.5-1 kpc for cold material in the inner region, and 0.5-4 kpc for warm material in the inner region. Comparing these values with those of our own Milky Way, cold material ($T < 10^4$ K) has a scale height of 0.4 kpc, while ionized material in the Milky Way extends as high as 2 kpc (Kalberla & Kerp, 2009). The MW radial scale length is 3.75 kpc, and the disk radius (again, considered to be the break radius between exponential profiles in the radial surface density) is $\sim$ 13 kpc. These values

agree well with the disks evolved with stellar feedback.

Furthermore, perhaps somewhat surprisingly, disks evolved with feedback contain more highly dense material, $> 10^8$ $M_\odot$ kpc^{-2}, than disks evolved without. We attribute this to conversion of gas to stars in models with feedback being slower than in models without it. Moderately dense material, $10^7 - 10^{7.5}$ $M_\odot$ kpc^{-2} extends further, in both the radial and vertical directions. In general, disks evolved with stellar feedback are more radially extended compared to those evolved without, as seen visually in figures 3.4 and 3.6, and quantitatively in their scale lengths.

We next consider the differences in disk structure created by our two different feedback algorithms. SB feedback is focused on modelling combined outflows and thus drives more material out of the disk. The efficiency of SB feedback has also decreased star formation (discussed in more detail in section 3.2.1). The SB disks are more dense (when considering only the gas) than other disks because there are still large amounts of gas available to form stars. Disks evolved with SB feedback are also more vertically extended than disks evolved with BW. This is particularly evident in the case of g1536, where the cold outer scale height is ~ 4 kpc, compared to ~ 2 kpc in the disk evolved with BW. In the radial direction, disks evolved with SB feedback are smaller than their BW counterparts. This is possibly due to supernovae at large radii disrupting the disk more easily when implemented through SB feedback than BW, as Keller et al. (2015) postulates.

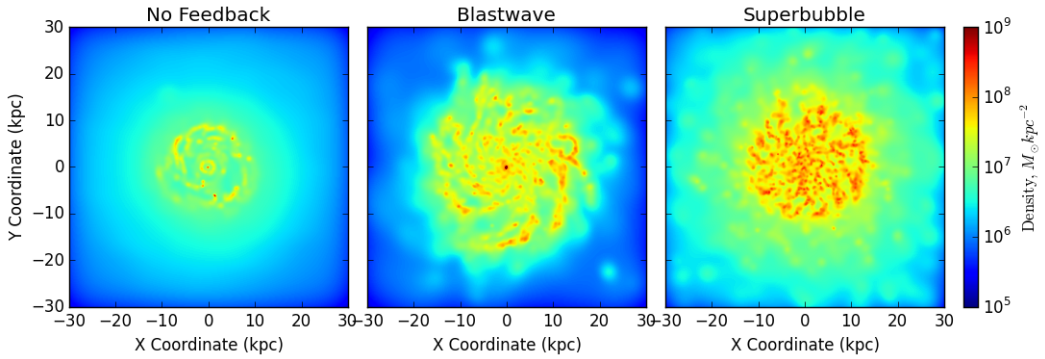

Figure 3.3: The smoothed face-on density field for disk g1536 simulated with the three distinct feedback algorithms.

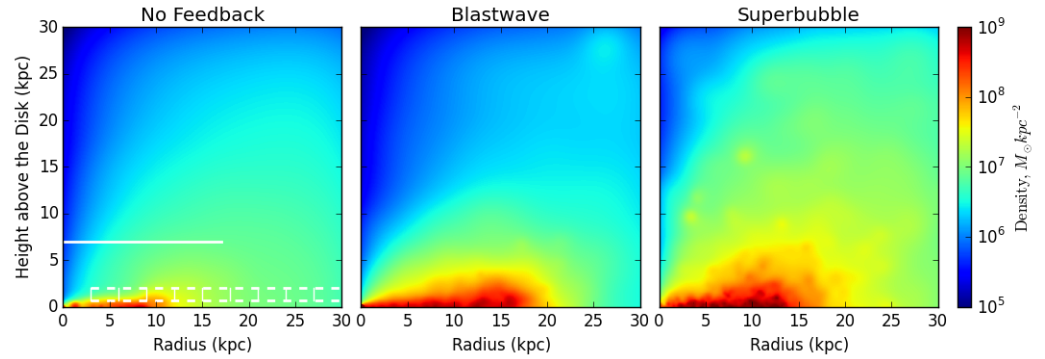

Figure 3.4: The smoothed edge-on density field for disk g1536 simulated with the three distinct feedback algorithms.

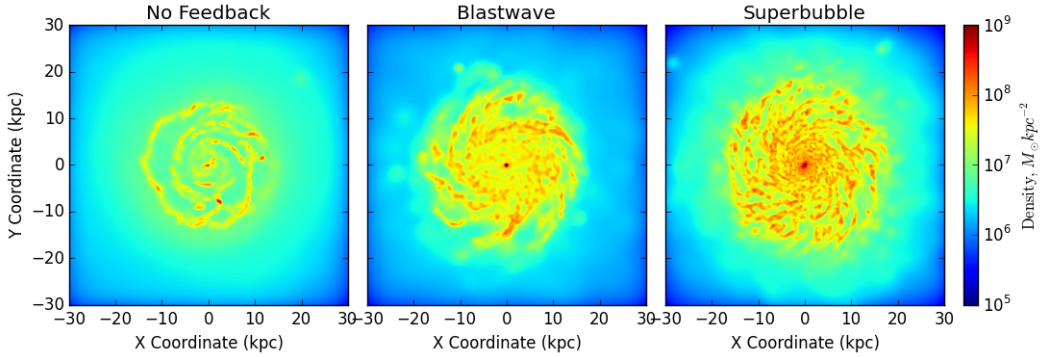

Figure 3.5: The smoothed face-on density field for disk g15784 simulated with the three distinct feedback algorithms.

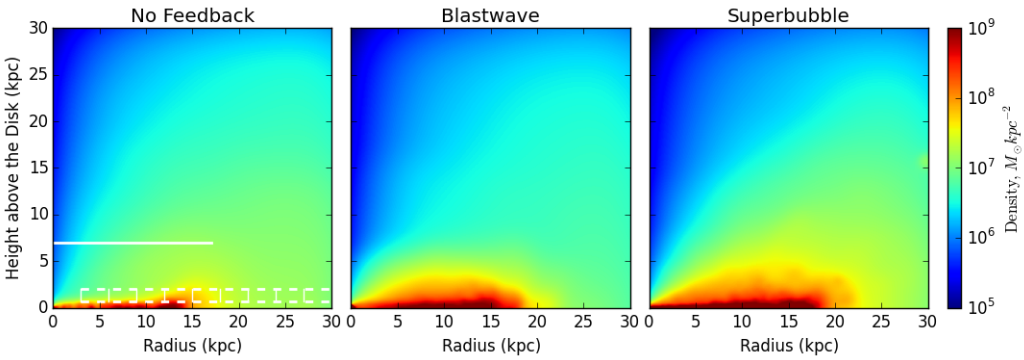

Figure 3.6: The smoothed edge-on density field for disk g15784 simulated with the three distinct feedback algorithms. The white lines in the NF panel depict the sheet (solid) and annuli (dashed) geometries analyzed in section 3.3.2.

3.1.2 The Temperature Structure of the Gas

To co-examine the density and temperature of the gas, we produce density profiles coloured by gas temperature, shown in figure 3.8. The goal of these plots is to determine how the gas is distributed as a function of temperature within the galaxies and halos. These plots were computed using the method of Marasco et al. (2015), which we describe here for completeness.

A cone with an opening angle of 30° is aligned with the z axis for the vertical maps. This opening angle is chosen by Marasco et al. (2015) such that the extra-planar HI gas, which is expected to exist in a toroidal shape (Fraternali & Binney, 2006), is not included in the analysis. The average density and temperature of the gas is calculated for bins of height 3 kpc, extending from 0 kpc, out to the virial radius. The gas maps are coloured according to temperature of the gas: $T < 10^4$ K in blue, $10^4 < T < 10^5$ K in green, $10^5 < T < 10^6$ K in red, and $T > 10^6$ K in magenta. The method is the same for the radial maps, except that the cone is aligned with the radial axis of the disk, and has an opening angle of 10°. This opening angle is set so that the cone will intersect the disk, but will not be contaminated by the atmosphere above and below it. A diagram of this geometry can be seen in figure 3.7.

First, to avoid the complexities of stellar feedback, we will consider the features of disks evolved without it. Shown in figure 3.8, panels *a* and *b*, these disks show no gas with temperatures less than 10^4 K. As discussed in section 2, all cold material within these disks has been turned into stars. Warm material extends out to the edge of the disk at approximately 10 kpc and then cuts off sharply. Disks without stellar feedback do not drive outflows, and are naturally less extended. Beyond 30 and 80 kpc, for g1536 and g15784 respectively, very hot gas no longer exists. This gas has either cooled below 10^6 K, or never existed at such high temperatures beyond the aforementioned radii in the first place. Note that this transition from $T > 10^6$K to $T < 10^6 K$ occurs at roughly the same height

as radius, as expected for a spherical distribution. Due to g15784 having twice the virial mass of g1536, the halo of g15784 is noticeably hotter, pushing this temperature transition outwards. We re-emphasize the differences between g1536 and g15784 arise from different masses, not from differences in the way feedback is applied.

We next compare the disks evolved with stellar feedback to those evolved without, and quantify the differences. The most obvious difference in figure 3.8 is that cold gas does exist in disks evolved with stellar feedback. This is likely explained by SNe outflows increasing turbulence in the ISM: although the material is both cold and dense, it has not all collapsed to form stars because it has not met the 'converging flow' criterion. Evidence of these outflows is also visible in the cold and warm material which exists beyond the break radii in disks evolved with feedback. Cold material exists up to radii of 45-60 kpc and 30-40 kpc, for g1536 and g15784 respectively and is associated with satellite systems. The existence of both hot and cold material in disks evolved with feedback is obviously indicative of the star formation feedback cycle. Although the temperature structure of these disks are more mixed than their NF counterparts, the cooling of material below 10^6 K or the point at which hot gas ceases to exist (the transition from magenta to red), occurs at the same spherical radii: 30 kpc for g1536, 80 kpc for g15784. This indicates a limiting radius at which feedback has not had a major impact on the halo gas state.

Although both BW and SB disks include type II supernovae physics, the implementation differences will drive different temperature structures in the halo gas. The bigger differences arise largely from the inclusion of mass evaporation: modelling the evaporation of material from the cold shell of the SNe bubble into the hot intarior. SB feedback includes an algorithm to calculate the heat flux due to thermal conduction, and a sub-grid model to calculate the mass evaporation that would arise. As gas is heated, it diffuses, leading to a smoothing of the dense interfaces between hot and cold material.

The effects of mass evaporation can be seen in two ways. For comparison, note both BW disks show a hot, dense nucleus of gas within the central 2 kpc. This can be difficult

to see, represented by the thin triangle of hot, very dense material at small radii in panels *c* and *d* of figure 3.8. In both disks, the density peaks at 10^{11} $M_{\odot}kpc^{-3}$. These nuclei are absent in the disks evolved with SB feedback. The mass evaporation implemented as part of the SB algorithm prevents the formation of gas which is hot and exceptionally dense. Secondly, away from the central nucleus at a radius of 10 kpc, hot material is less dense in disks evolved with SB feedback than BW feedback. Warm and hot gas in disks evolved with SB feedback is below 10^{8} $M_{\odot}kpc^{-3}$ at 10 kpc. In comparison, gas in disks evolved with BW feedback is approximately 10^{8} $M_{\odot}kpc^{-3}$, and consistently more dense than 10^{7} $M_{\odot}kpc^{-3}$. As material is heated by SB feedback it is transported opposite to the heat flux, resulting in hot material which is systematically less dense than in disks evolved with BW feedback.

Finally, note that there is cold material in the vertical maps of disks evolved with SB feedback. It is likely that BW feedback is strong enough to destroy cold gas in the central regions above the disk, while SB feedback is not. This may seem counter-intuitive, as we have been arguing that SB feedback is more efficient than BW. However, recall that at the centre of the BW disks there exists a stellar bulge and a dense nucleus of gas. Many more stars are forming here than in the same region of a disk evolved with the SB algorithm. The feedback associated with nuclear star formation blows out the gas in the central region above the disk, away from the region being analyzed for figure 3.8.

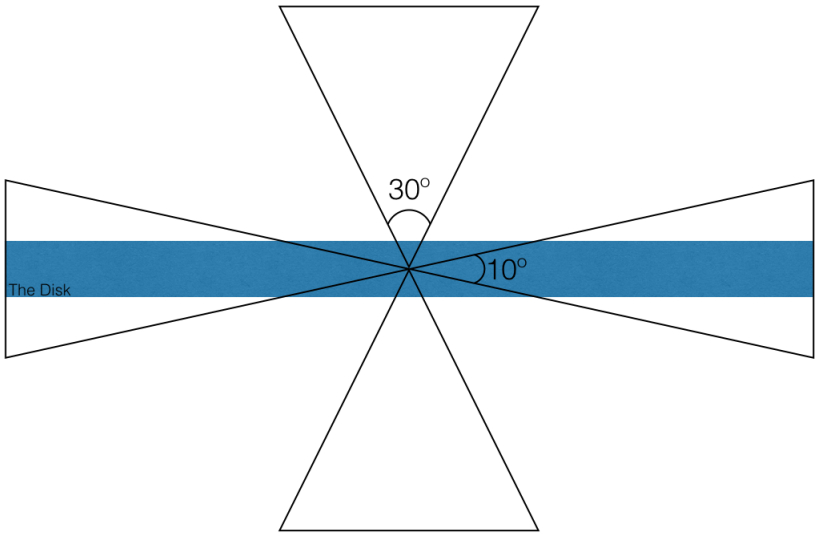

Figure 3.7: The geometry used to create the maps of gas temperature and density. The disk is shown edge-on (blue pillbox), with cones opening vertically, and radially.

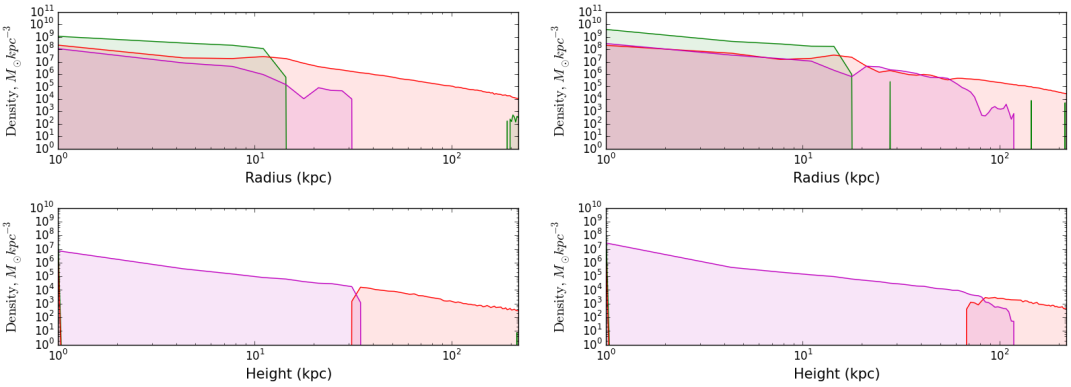

(a) g1536, NF

(b) g15784, NF

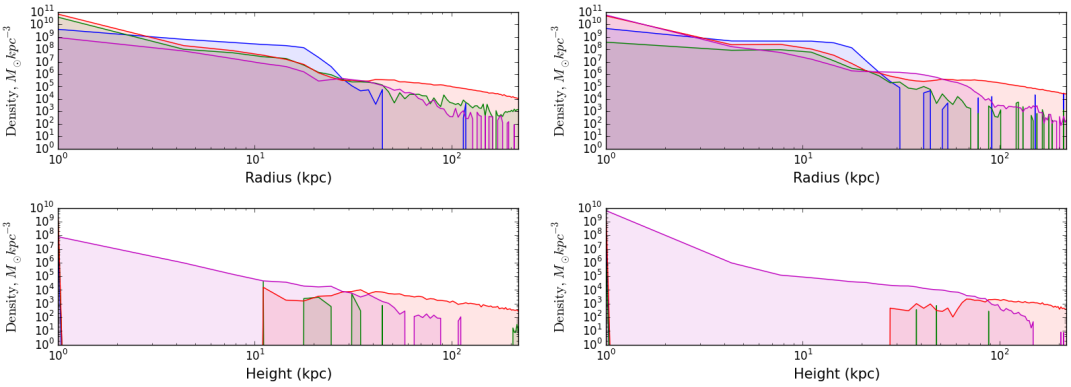

(c) g1536, BW

(d) g15784, BW

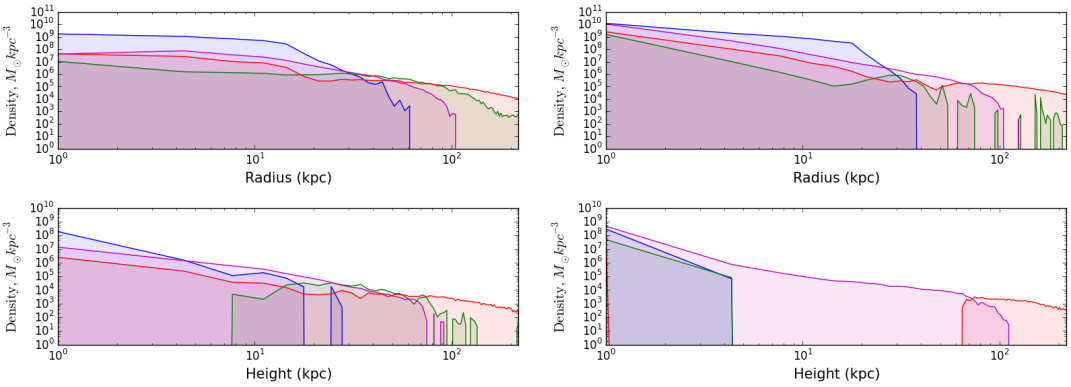

(e) g1536, SB

(f) g15784, SB

Figure 3.8: The radial and vertical density and temperature structure of g1536 and g15784 at $z = 0$. The colours represent gas temperature: $T < 10^4$ K in blue, $10^4 < T < 10^5$ K in green, $10^5 < T < 10^6$ K in red, and $T > 10^6$ K in magenta.

3.1.3 Velocity Structure of the Nucleus, Disk, and Halo

In the density and temperature profiles, the disks evolved with BW feedback exhibits a dense hot nucleus of gas in the centre of the disk. This massive nucleus would eventually convert gas into stars, producing a large bulge component. The lack of gaseous nuclei in disks evolved with SB feedback prompts another question: does SB feedback solve the problem of overly large stellar bulges seen in simulated galaxies? Figures 3.9 and 3.10 show the rotation curves for each disk and feedback algorithm. The circular velocity is calculated, taking both baryons and dark matter into account, and plotted in red. The tangential velocity of the gas is calculated within the disk (solid blue lines), and at varying heights above the disk, to study the vertical rotation structure of the galaxies.

Focusing first on the rotation curve of g1536 evolved without stellar feedback, the left most panel of figure 3.9, this disk shows the most peaked circular velocity curve in the central region. The maximum circular velocity is 375 km/s, while the maximum tangential velocity of the gas in 325 km/s within the plane of the disk. The tangential velocity of the gas is less than the circular velocity because the gas is partially supported through turbulence within the disk or other issues of gas dynamics (such as a central bar). Gas away from the central bulge, but within the plane of the disk, rotates at approximately 230 km/s. The velocity within the plane of the disk falls off quickly at a radius coincident with the disk edge, 8.75 kpc - this behaviour is seen in all disks. The rate of rotation falls off quickly with height, decreasing to 140 km/s just 3 kpc above the disk. 40 kpc away from the centre, the circular velocity is 175 km/s, while gas at all heights rotates at approximately 75 km/s.

BW feedback will delay star formation, and prevent runaway collapse of gas. This reduces the size of the stellar bulge, as seen in the decreased central velocity shown in the second panel of figure 3.9. The maximum circular velocity is 325 km/s in the stellar bulge. The tangential velocity of the gas within the stellar bulge peaks at 275 km/s. Gas within

the disk, but not the bulge, has a velocity of 225 km/s. The rate of rotation with height, $\frac{dv_c}{dz}$, does not fall off as quickly as seen in g1536_NF. At 40 kpc, the circular velocity is 175 km/s, while gas at all heights rotates at approximately 75 km/s beyond $\sim$ 25kpc. This is exactly as seen in the disk evolved without feedback, suggesting BW feedback has not strongly impacted this material, or has not done so recently.

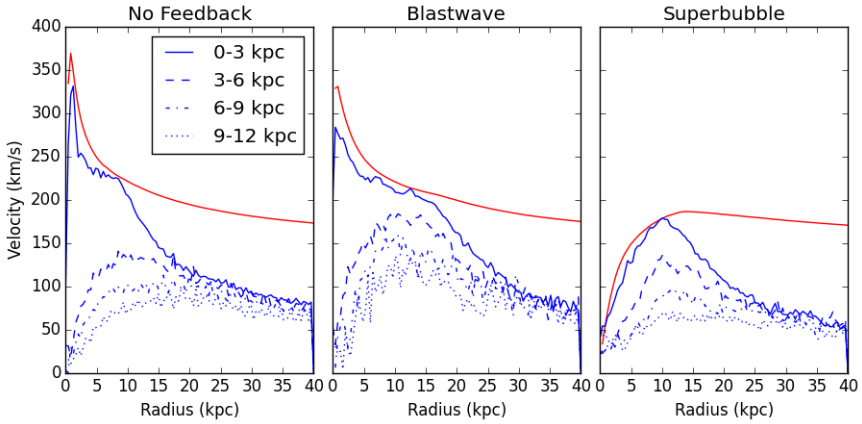

Figure 3.9: Rotation curves for g1536 disks, at $z = 0$

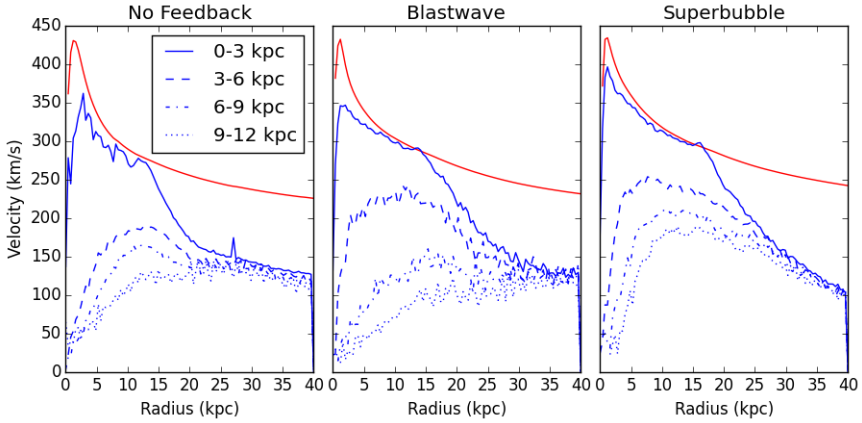

Figure 3.10: Totation curves for g15784 disks, at $z = 0$

We now consider the rotation curves of g1536_SB, in comparison to those of g1536_BW. As discussed in the previous section, the implementation of mass evaporation in SB feedback prevents the formation of a dense nucleus of gas. Furthermore SB feedback effectively

combines many supernovae, thus driving material further from the disk. Consequently, SB feedback effectively prevents the formation of a stellar bulge. This is directly seen in the rotation curves: the disk evolved with SB feedback has no central velocity peak. The maximum circular velocity is 200 km/s at $\sim$ 12 kpc. The tangential velocity of the gas within the plane of the disk (shown in solid blue) peaks at 175 km/s at 10 kpc. At 40 kpc, the circular velocity is the same as in g1536_BW and g1536_NF, 175 km/s, indicating the similarity of the enclosed masses. The tangential velocity of the gas above the disk is slower, only rotating at 50 km/s beyond $\sim$ 25kpc compared to the 75 km/s seen in BW, however the overall disk rotation is slower as well.

To understand the structure of the gas above the disks and how it is rotating with them, we plot contours of the smoothed velocity, shown in figures 3.11 and 3.12. First, we consider the contours of g1536. The disk evolved without stellar feedback shows the fastest fall-off of velocity with height, exactly as seen in the rotation curves. g1536_BW retains the fastest rotation rate 15 kpc above the disk. At all heights, the rotation speed of the gas of g1536_SB is slower than its BW counterpart, as expected from it's lower circular velocity.

Turning our attention to the rotation curves of g15784, as shown in figure 3.10, the most obvious feature of these plots is the central peak in the circular velocity seen in all disks, including g15784_SB. Recall that g15784 is twice as massive as g1536, and as such the temperature of the halo is hotter (this is seen in figure 3.8). Stellar feedback will heat gas to approximately 10^6 K, regardless of halo mass. As such, there is a larger difference between feedback temperature and halo temperature for a small galaxy than a large galaxy; so feedback will impact the small galaxy while eventually becoming negligible in more and more massive haloes. The end-result is three disks which all exhibit a peak in the circular velocity of $\sim$ 425 km/s at small radii. The tangential velocities within the plane of the disk peak close to the centre as well. Notice that the gas in the central regions of the disk evolved with SB feedback is rotating the most quickly. As mentioned in the discussion of g1536, the tangential velocities are less than the circular velocities due to support provided

by turbulence and gas dynamics. These reasons also explain why g15784_SB has a much larger central tangential velocity than g15784_BW or g15784_NF. g15784_BW is very hot in the central regions (recall the hot gaseous nucleus discussed in section 3.1.2), lending the material thermal support. g15784_NF has a strong central bar, transferring angular momentum from the gas and decreasing rotation speed.

In figure 3.12 we plot the vertical rotation structure of g15784. The highest velocity material traces the disk for all feedback algorithms. Gas with tangential velocities of 100 km/s or greater extends as high as 25 kpc above the disk in g15784_SB, $\sim$ 10 kpc higher than g15784_NF or g15784_BW. This indicates that gas above the disk is more strongly coupled with it, in the case of SB feedback. This is likely due to the mass evaporation allowing material to diffuse outwards, and preventing the formation of harsh transitions in density. This is seen in figure 3.6 as well.

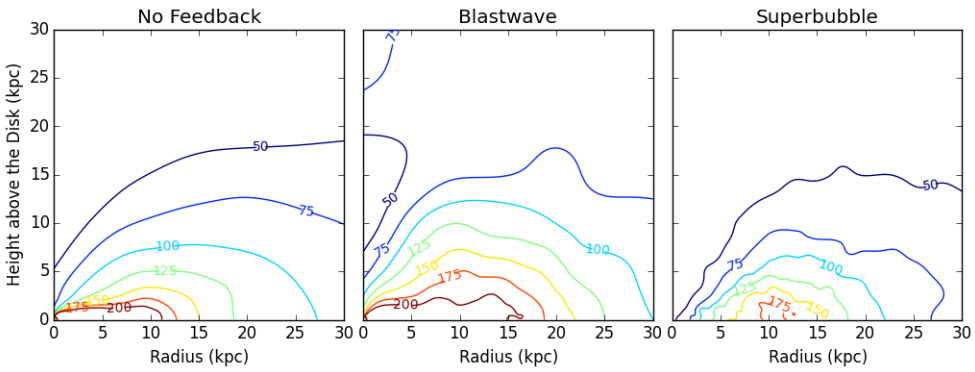

Figure 3.11: The smoothed velocity contours for disk g1536

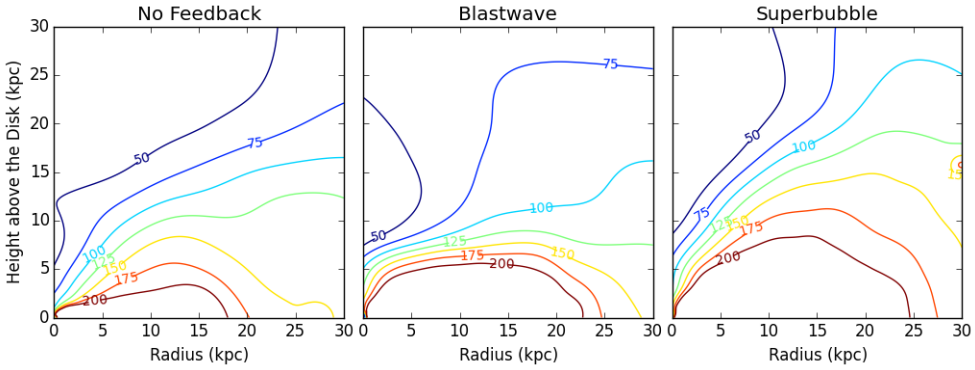

Figure 3.12: The smoothed velocity contours for disk g15784

3.2 Galactic Structure Evolution

We have seen how different feedback algorithms affect the morphologies of the disk at $z = 0$. We next look at how they impact the evolution of galactic structure and other properties. This can be probed in three ways: by looking at the star formation rates, the evolution of the disk mass, and the evolution of the density profiles of the dark matter and baryons.

3.2.1 Star Formation Rates

The star formation history of a galaxy traces its growth. For obvious reasons, the star formation rate is closely tied to stellar feedback. We expect the star formation histories to vary greatly with different stellar feedback algorithms. The star formation history is plotted in bins of ~ 137 Myr, shown in figures 3.13 and 3.14.

We focus first on the disks evolved without stellar feedback specifically. Without stellar feedback, the star formation rate is not moderated. The star formation rate peaks at 26 $M_{\odot}yr^{-1}$, at $z = 4$ for g1536_NF; 46 $M_{\odot}yr^{-1}$, at $z = 3$ for g15784_NF. Note that g15784_NF also has an early peak in star formation, 27 $M_{\odot}yr^{-1}$ at $z = 4.5$. Much of the gas, in both disks, is turned into stars before 2 Gyr, as there is no heating mechanism implemented to prevent its collapse. Early star formation is associated with the formation of a stellar bulge, in good agreement with the results of section 3.1.3. We have discussed previously the absence of cold material in disks when evolved without stellar feedback, and argued that it was due to all material collapsing to form stars. This is reinforced by the peak in star formation at high redshift, and the very low star formation rate at $z = 0$, $\sim 2.5 M_{\odot}$/yr and ~ 5 $M_{\odot}$/yr, for g1536_NF and g15784_NF respectively.

Including stellar feedback introduces a heating mechanism to balance the gas cooling. Star formation is delayed, and controlled such that gas exists for star formation to continue at $z = 0$. The disks evolved with BW feedback show a delayed peak in star formation. g1536_BW peaks at 23 $M_{\odot}yr^{-1}$ at $z = 2$, while g15784_BW shows two peaks, at

~ 50 $M_{\odot}yr^{-1}$, at $z = 3$ and $z = 2$. This is in good agreement with the average cosmic star formation history (Heavens et al., 2004). While we would expect any single galaxy to differ from the cosmic average SFH, the comparison here is used to show that star formation has been delayed to a redshift at which high levels of star formation are observed. From $z = 1.5$ to $z = 0$ the star formation is nearly constant, at 5 $M_{\odot}yr^{-1}$.

Finally, we consider the star formation histories of disks evolved with SB feedback. The SB feedback algorithm is more efficient at heating material through the thermal conduction algorithm and the implementation of multi-phase particles. In g1536_SB, this highly efficient feedback algorithm produces a disk with comparatively little star formation. As seen in figure 3.13, no peak in star formation has occurred. The star formation rate has been steadily increasing with time, reaching a maximum of 5 $M_{\odot}yr^{-1}$ at $z = 0$. The lack of stars in g1536_SB can be further emphasized by considering the stellar mass of the system. g1536_SB has a stellar mass of only 1.8 $\times 10^{10}$ $M_{\odot}$, while g1536_BW and g1536_NF have stellar masses of 5 $\times 10^{10}$ $M_{\odot}$ and 7.2 $\times 10^{10}$ $M_{\odot}$, respectively.

In g15784_SB, we see a very different disk. Recall that g15784 has twice the virial mass of g1536, and it has already been established that the gravitational binding energy of the halo is dominant over the energy returned through stellar feedback. After a merger at $z = 3$, the star formation rate of g15784_SB increases dramatically by 30 $M_{\odot}yr^{-1}$ in less than 1 Gyr, peaking at 37 $M_{\odot}yr^{-1}$ at $z = 1.5$. The star formation history of g15784_SB is highly skewed towards lower redshifts, unlike the SFH of g15784_BW or g15784_NF which are more symmetric about their peak. SB feedback prevents the excess gas from forming many stars all at once, but as material builds up star formation must occur. This allows a moderately high star formation rate to persist for much longer periods of time.

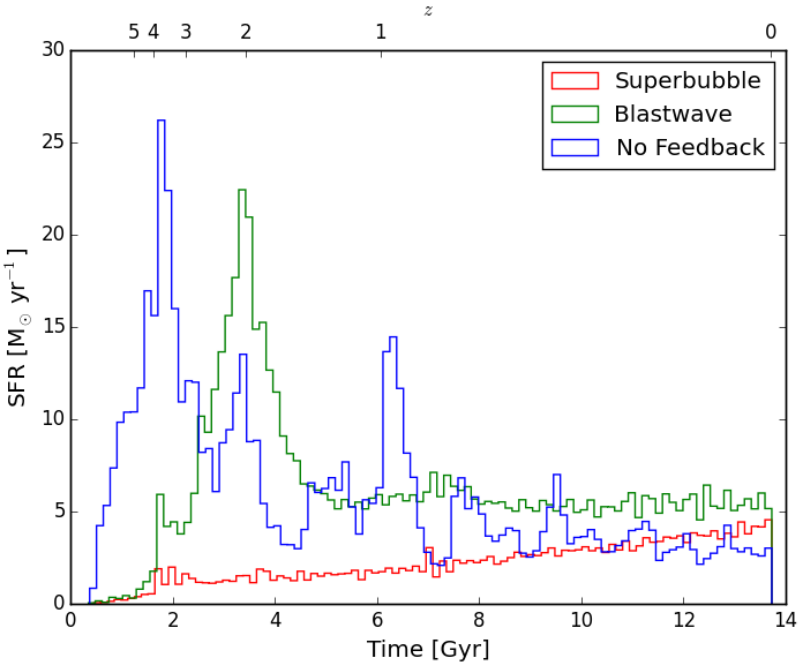

Figure 3.13: g1536 star formation rates

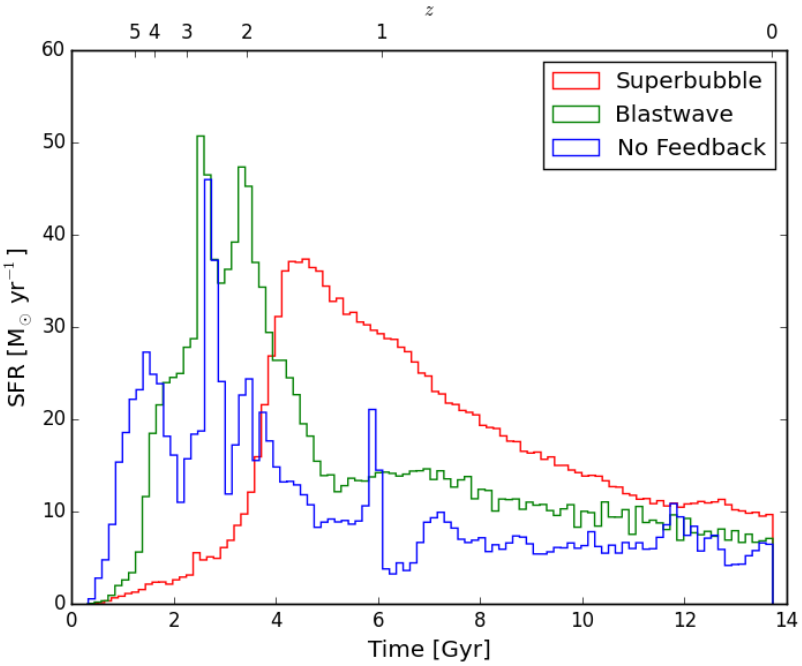

Figure 3.14: g15784 star formation rates

3.2.2 Evolution of the Disk Mass

The Disk Mass

In section 3.1 we considered the properties of the gas in each disk at $z = 0$. We now consider the evolution of the gas in conjunction with the stellar evolution by calculating the disk mass at six redshifts $z = [3, 2, 1, 0.5, 0.25, 0]$. To calculate the disk mass we sum the total baryon mass within a cylinder of height ± 3 kpc, and a radius of 20 kpc, centered on the star with the minimum potential. All of the disks have a radius less than 20 kpc at $z = 0$, so they will certainly be radially contained by this cylinder. Material beyond the edge of the disk drops off radially, so there is little concern of over-estimating the disk mass by setting the radial boundary to 20 kpc.

Although all of the disks have a break radius of less than 20 kpc, material in the region beyond the disk drops off exponentially, and will have only a small effect on the disk mass estimates.

We consider the evolution of the disk mass for the smaller disk first, g1536, shown in figure 3.15. The disk evolved without feedback produces the most massive disk at $z = 0$, 6.9 $\times 10^{10}$ $M_\odot$; followed closely by the disk with BW feedback, 6.5 $\times 10^{10}$ $M_\odot$. This is expected, as the star formation histories of both disks are similar. The star formation of g1536_SB is suppressed by SB feedback. This leads to the formation of a less massive disk, reaching a disk mass of 4 $\times 10^{10}$ $M_\odot$ at $z = 0$. Let us also consider how the disk mass is built up with time. In the disks evolved without feedback and with BW feedback, the disk is built up quickly between $z = 4$ and $z = 1$. 50% of the disk mass is established by $z = 1.4$. Contrarily, g1536_SB has a slowly increasing star formation rate and slowly increased disk mass to match. 50% of the SB disk is assembled after $z = 1$.

We next turn our attention to the evolution of the disk mass for g15784, which has twice the virial mass of g1536. We would expect similar behaviour to g1536: the disk evolved without feedback to be most massive, and the disk evolved with SB feedback to be least

massive. However, as shown in figure 3.16, we see the opposite trend. g15784_SB produces the most massive disk, reaching 1.6 $\times 10^{11}$ $M_\odot$ at $z = 0$; followed by g15784_BW, reaching 1.4 $\times 10^{11}$ $M_\odot$ at $z = 0$. The disk evolved without stellar feedback is the least massive, reaching 1.2 $\times 10^{11}$ $M_\odot$ at $z = 0$. This is contradictory to the behaviour of g1536, and also to the expected behaviour based on prior research. Recall from the introduction that stellar feedback was initially implemented to prevent runaway star formation and over-massive disks. Furthermore, consider the evolution of g15784_SB; the disk mass increases quite suddenly beginning at 4 Gyr. This is coincident with the peak in star formation of g15784.

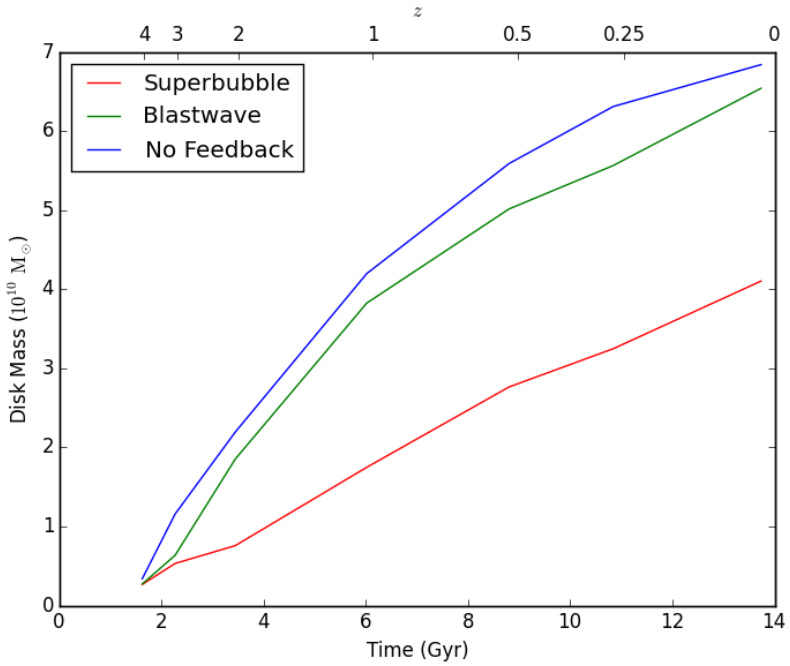

Figure 3.15: Evolution of disk mass for g1536

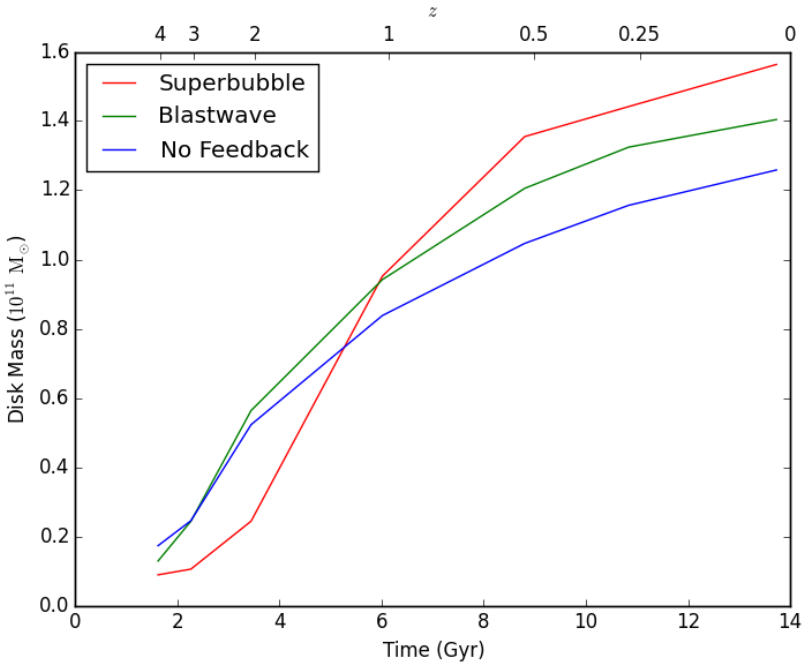

Figure 3.16: Evolution of disk mass for g15784

Can Superbubble Feedback Trigger Accretion?

It is counterintuitive that a galaxy evolved with more efficient feedback would be more massive than one evolved without feedback entirely. To explore why this is occurring, we can look at the radial mass and temperature structure of the halo. We will focus on the redshifts close to the point at which the disk mass of g15784_SB increases dramatically.

We first consider the radial mass and temperature of g1536, which does conform to the expected relationship between mass and feedback algorithm efficiency. Figure 3.17 shows how the temperature structure of g1536 changes with time. At $z = 2$, all three g1536 halos have similar temperature structures away the central regions. Within the central region, $r < 25$ kpc, the temperature structure is different between the different feedback mechanisms due to the significantly different star formation histories at this point in evolution. The halo of g1536_SB becomes progressively cooler than g1536_NF and g1536_BW with time, until $z = 0$.

Figure 3.18 shows the gas mass of g1536 in radial bins. This plots essentially the density of the halo in radial bins, without normalizing by the bin volume. g1536_NF and g1536_BW show similar radial mass profiles in the outer region of the halo. g1536_BW shows more gas at radii less than 25 kpc (for $z \leq 1.0$), which is expected because blastwave outflows will eject material into this region (outflows which are absent in the NF disk). g1536_SB is more massive in all radial bins, at all redshifts, indicating that the gas around g1536_SB is more dense. The mass differences are greater at smaller radii, coincident with the cooler regions of the g1536_SB halo.

We can directly confirm whether the dense gas around g1536_SB is cold by plotting the mass in radial bins of cold gas only ($T_{\rm gas} < 1.5 \times 10^4$K), shown for g1536 in figure 3.19. First, notice that there are only very small amounts of cold material around g1536_NF, likely associated with individual cold clouds. In g1536_BW, the radial cold mass peaks around 10-20 kpc, and doesn't exist beyond 25 kpc. This can be contrasted with g1536_SB:

the radial cold mass peaks higher than g1536_BW, and extends radially further into the halo. So there is more cold gas in the halo of g1536_SB than g1536_BW, particularly in the inner 50 kpc. The increased cold gas could indicate that SB feedback is creating a reservoir of cold material in this region. Enriched gas is ejected into the halo, which cools quickly compared to the pristine gas. Thermal conduction allows for these cold, enriched, pockets to cool the warm halo gas around them.

With this theory of a SB feedback fuelling a cold gas reservoir, we can analyze g15784. Again, we begin with the radial temperature structure, shown in figure 3.17. All three halos have similar temperature structures beyond 75 kpc. g15784_SB is cooler at radii less than 75 kpc, until $z - 0$. Figure 3.21 shows the gas mass in radial bins for g15784. At radii less than 75 kpc, where g15784_SB is cooler than the BW or NF halos, the gas in the halo of g15784_SB is more dense. From $z = 2.0$ to $z = 0.5$, there is a transition in the region from over-dense to under-dense, compared to g15784_BW. This suggests a flow of material onto the disk in the SB halo, which does not exist for the BW or NF halos. From figure 3.22, we can confirm that the dense material in g15784_SB is cold. There is more cold material in the halo of g1584_SB than in the BW or NF halos. The amount of cold material in g15784_SB decreases from $z = 2$ to $z = 0.5$, consistent with the flow suggested in figure 3.21. This is where g15784_SB is different from g1536_SB. The cold reservoir created by SB feedback around g1536 persists until $z = 0$ without accreting back onto the disk. This is not true for g15784, where the flow of material between $z = 2$ and $z = 0.5$ suggests that the cold reservoir is accreted.

To understand why this cold gas accretes onto g15784, but not g1536, we consider the amount of inflowing and outflowing material in the halo. In spherical bins, any particle with a radial velocity inwards is considered inflowing, and material with an outwards radial velocity is outflowing. Figures 3.23 and 3.24 show the inflowing and outflowing gas mass for g1536 and g15784 respectively. Note that these figures omit the results of $z = 0.5$ to instead include $z = 2.5$. We can see that g1536_SB shows larger amounts of outflowing

material than g1536_BW, at all radii at $z \geq 1$. By $z = 0$, the amount of outflowing material in g1536_SB beyond 100 kpc has decreased to below the level of g1536_BW. In contrast, g15784_SB has less outflowing material beyond 50 kpc than g15784_BW, at all $z < 2$. At $z = 2.5$, g15784_SB is very similar to results of g1536_SB at $z = 0 - 0.5$. g15784_SB stops driving very strong outflows when it begins accreting the cold reservoir built by SB feedback, and this occurs at $z = 2.0 - 2.5$. This suggests a binding energy argument: at $z = 2$ the mass of g15784 is large enough that SB outflows cannot be driven as far into the halo, and the cold reservoir begins to be accreted. It is interesting to note that the virial mass of g15784 is $6.88 \times 10^{11} M_{\odot}$ at $z = 2$, just slightly more massive than g1536 at $z = 0$. The similarities between g1536 at $z = 0$ and g15784 at $z = 2 - 2.5$ suggests that with more time to evolve, g1536 would likely follow the same path and accrete the cold gas reservoir built up by SB feedback, and become overmassive compared to g1536_BW. It is also likely that this accretion would trigger a sudden spike in star formation, similar to the one seen in g15784_SB at $z = 2.5$.

It is not a novel idea that SB feedback might trigger accretion onto a galactic disk. Hobbs et al. (2015) suggests that SB feedback triggers accretion onto the disk through the creation of filaments in the halo. SB feedback-driven outflows extend further into the halo than is modelled by BW feedback. These outflows can collide and shock within the halo: creating pockets of dense, enriched material. This material is prone to cooling quickly, and can form filaments which funnel material directly onto the disk. Although these filaments cannot be resolved by our simulations, our findings of increased cold material in halos evolved with SB feedback and the subsequent accretion onto g15784_SB are in broad agreement with Hobbs et al. (2015).

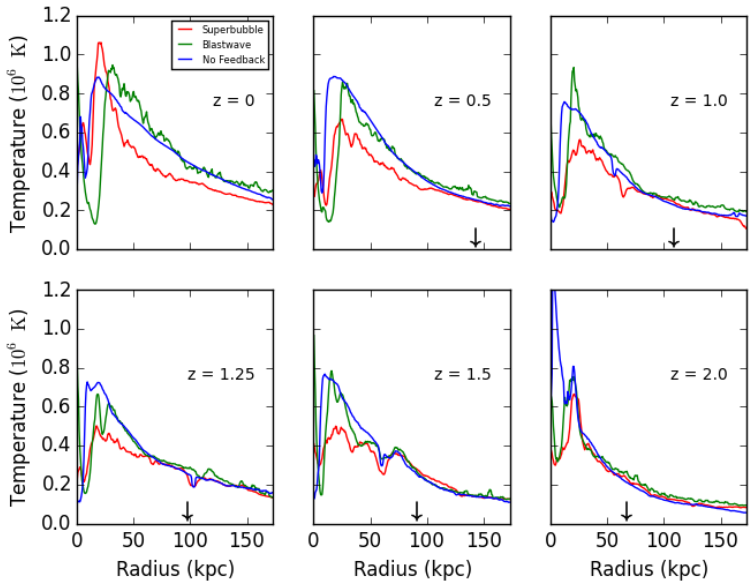

Figure 3.17: Evolution of the radial temperature structure for g1536

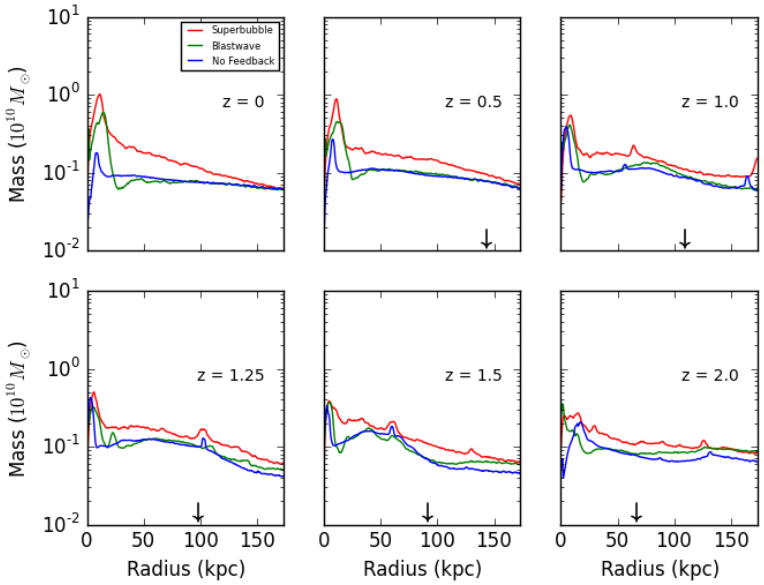

Figure 3.18: Evolution of the total gas mass in radial bins for g1536

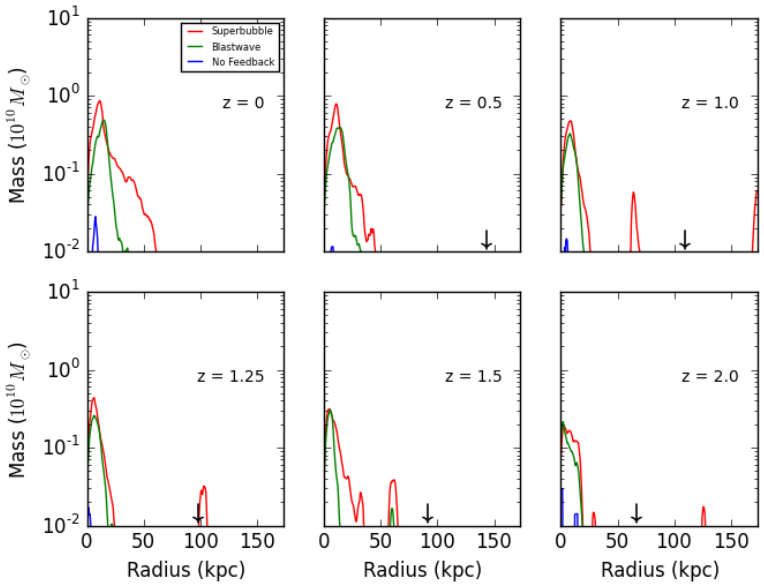

Figure 3.19: Evolution of the cold gas mass in radial bins for g1536

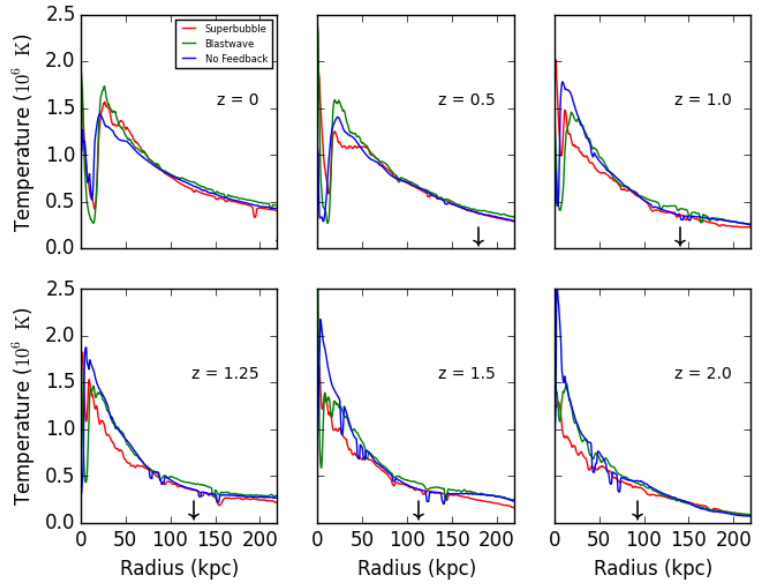

Figure 3.20: Evolution of the radial temperature structure for g15784

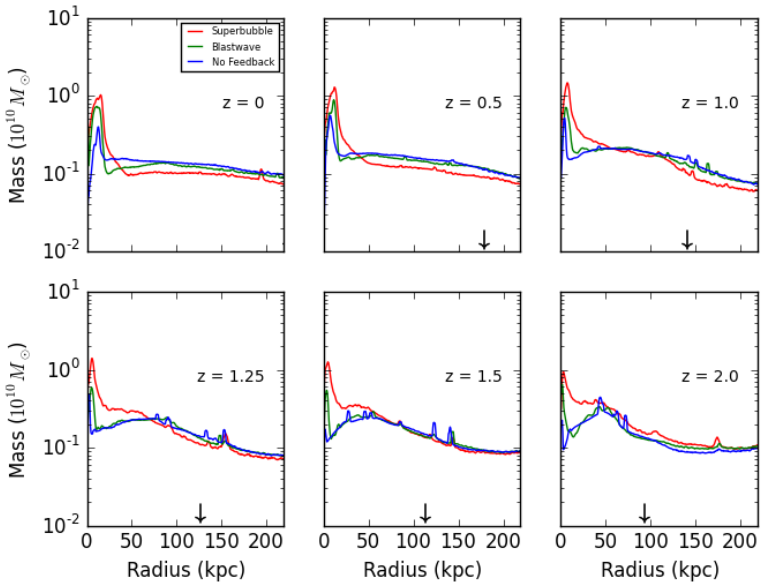

Figure 3.21: Evolution of the total gas mass in radial bins for g15784

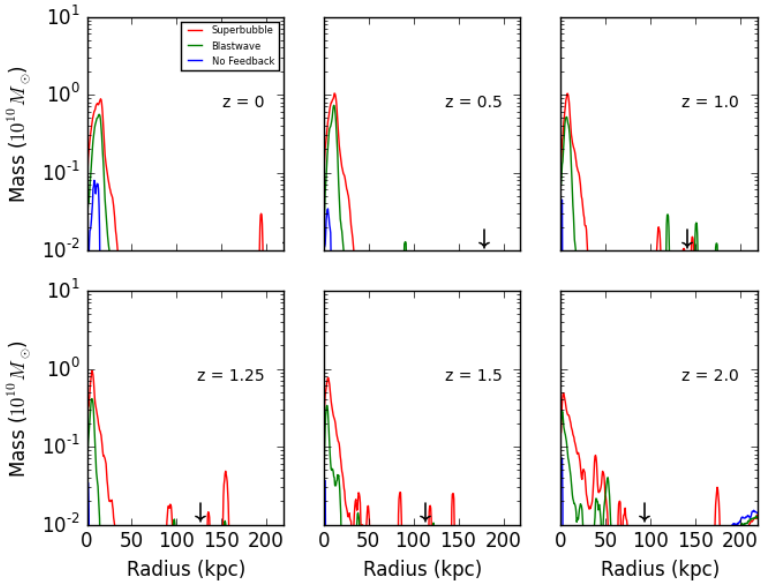

Figure 3.22: Evolution of the cold gas mass in radial bins for g15784

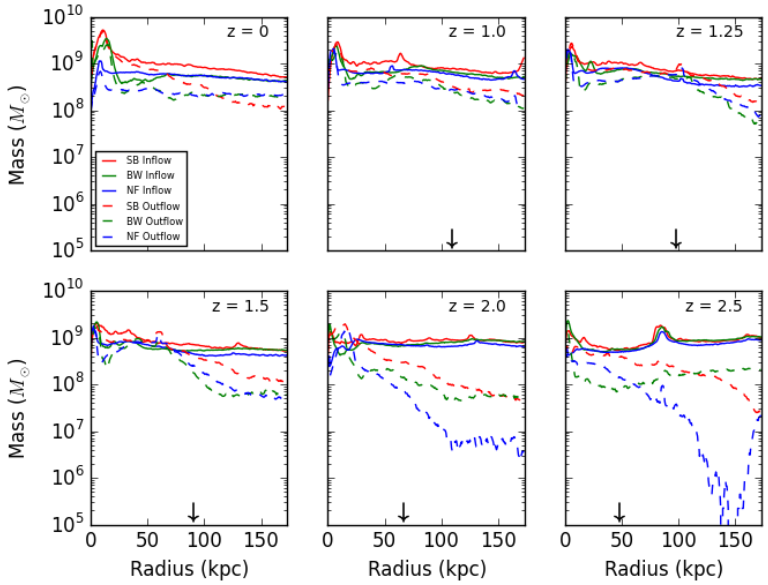

Figure 3.23: Evolution of the inflow and outflowing gas mass in radial bins for g1536

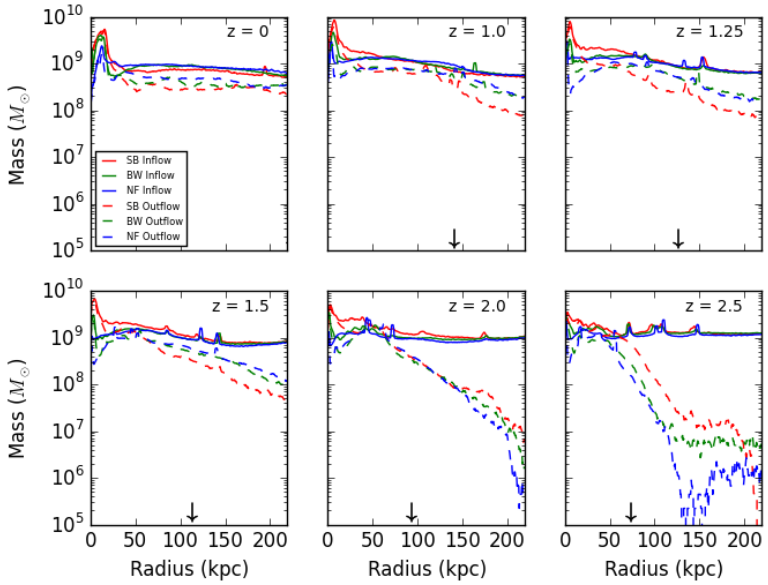

Figure 3.24: Evolution of the inflowing and outflowing gas mass in radial bins for g15784

3.2.3 Evolution of the Dark Matter within the Virial Radius

We have seen so far the ways in which stellar feedback impacts the gas and stars of g1536 and g15784. We next consider how stellar feedback will impact the dark matter in these systems. The dark matter density profile has an expected relationship with radius, such that

$$\rho(r) = \frac{\rho_0}{\frac{r}{r_s}\left(1+\frac{r}{r_s}\right)^2}, \tag{3.1}$$

as originally discussed in Navarro et al. (1997) (hereafter, the NFW profile). The NFW profile describes the radial density profile of the dark matter with two parameters; ρ_0, a characteristic density, and r_s, the scale radius. The NFW profile is expected to follow a slope of $\sim r^{-1}$ in the central regions, and steepening to $\sim r^{-3}$ at distances close to the virial radius. Figures 3.25 and 3.26 show the baryonic and dark matter density for g1536 and g15784 respectively. The density profiles are calculated from 0.3 kpc out to the virial radius of the halo at $z = 0 - 4$. The virial mass of each halo, and the redshift of the plot is printed in the upper right. The softening length, 0.3 kpc, is marked by a solid black line, while three times the softening length, 0.9 kpc, is marked by the black dashed line. These lines indicate the point at which the simulations can be said to be resolved. Finally, a red line is annotated in the final panel, $z = 0$, indicating a line with slope of r^{-3}. The dark matter density profiles of all halos show NFW-like behaviour.

We first consider the density profiles of the dark matter for g1536, the less massive disk. In g1536_NF the dark matter density profile in the central region is less steep than at the virial radius. The central density is approximately 10^9 $M_\odot kpc^{-3}$ at $z = 4$, and does not vary greatly with redshift. At $z = 0$ we see that at close to the virial radius of the halo, the density follows a slope close to, or perhaps slightly shallower than, r^{-3}. This is in good agreement with the expectations of the NFW profile, and true for all three g1536 disks.

We can compare the profile of g1536_NF with the dark matter density profile of g1536_BW.

The dark matter density is initially less dense in the central region, 10^8 $M_\odot kpc^{-3}$ at $z = 4$, but increases to 10^9 $M_\odot kpc^{-3}$ at $z = 0$. At $z = 0$, the dark matter density profile of g1536_BW is very similar to g1536_NF. It is between $z = 3$ and $z = 2$ that the central dark matter density increases. We notice that this increase in the dark matter density is coupled with a similar increase in the baryon density. This coincides with the sudden onset of star formation in g1536_BW. As the gas cools and contracts this will trigger a similar contraction in the dark matter, as further investigated by Duffy et al. (2010). Once both g1536_NF and g1536_BW have experienced a peak in star formation, their dark matter densities look very similar. This implies that BW feedback is not affecting the dark matter density profile.

Other theories have been put forward to explain why some observed galaxies may deviate from the NFW profile in the central regions. In particular, Mashchenko et al. (2006) argues that small-scale bulk motions of gas in the central region at $z \geq 10$ remove the cusp. Once removed, it cannot be reintroduced. However, the time when this effect is expected to dominate is beyond what we are considering here ($z \leq 4$). Furthermore, the dark matter density profile of g1536_BW is shallower at $z = 4$ and steepens with time. This is in better agreement with the theory proposed by Duffy et al. (2010), in which the cusp is produced through baryon contraction.

We next consider how SB feedback will affect the dark matter density. At $z = 4$, the dark matter density profile of g1536_SB looks very similar to that of g1536_BW. The central region peaks at 10^8 $M_\odot kpc^{-3}$, and is shallower than the density profile closer to the virial radius. However, unlike g1536_BW, the dark matter never contracts. The density remains at 10^8 $M_\odot kpc^{-3}$, and shallow in the central region up to $z = 0$. Recall that g1536_SB showed no peak in star formation, and so it follows that there is no sudden contraction in the baryon density to trigger a contraction of the dark matter in the central regions. This lack of collapse could be due simply to the different heating efficiencies of BW and SB feedback in the central regions. Exactly how these two feedback algorithms differ in this complicated region is difficult to understand.

In previous results, we have seen that the effects of stellar feedback are diminished in the disks of g15784, due to their increased mass. We would therefore expect to see fewer differences in the dark matter density profiles of g15784. At $z = 3$ both g15784_NF and g15784_BW have experienced a peak in star formation. This results in similar dark matter density profiles, slightly shallower than at the virial radius, with a maximum of $\sim 10^9$ $M_\odot kpc^{-3}$ in the central region. Notice that at $z = 3$, g15784_SB has not yet experienced a star formation peak, and so the dark matter density profile is shallower, and has a lower central density of 2×10^8 $M_\odot kpc^{-3}$. At $z = 2$ there still has been no peak in star formation in g15784_SB, and the virial mass is very similar to that of g1536. The density profiles of g15784 at $z = 2$ look very similar to those of g1536 at $z = 0$. At $z = 1$, star formation has peaked in g15784_SB, and as expected we see a steepened dark matter density profile, with a central density of $\sim 10^9$ $M_\odot kpc^{-3}$. The dark matter density profiles of all disks appear to flatten from $z = 1$ to $z = 0$. This flattening is entirely contained within 0.9 kpc, and it cannot be determined if it is realistic, or a byproduct of the unresolved central region. Finally, similarly to g1536, all three disks show a dark matter density profile with a slope close to, or slightly shallower than, r^{-3}, in good agreement with the expected NFW profile.

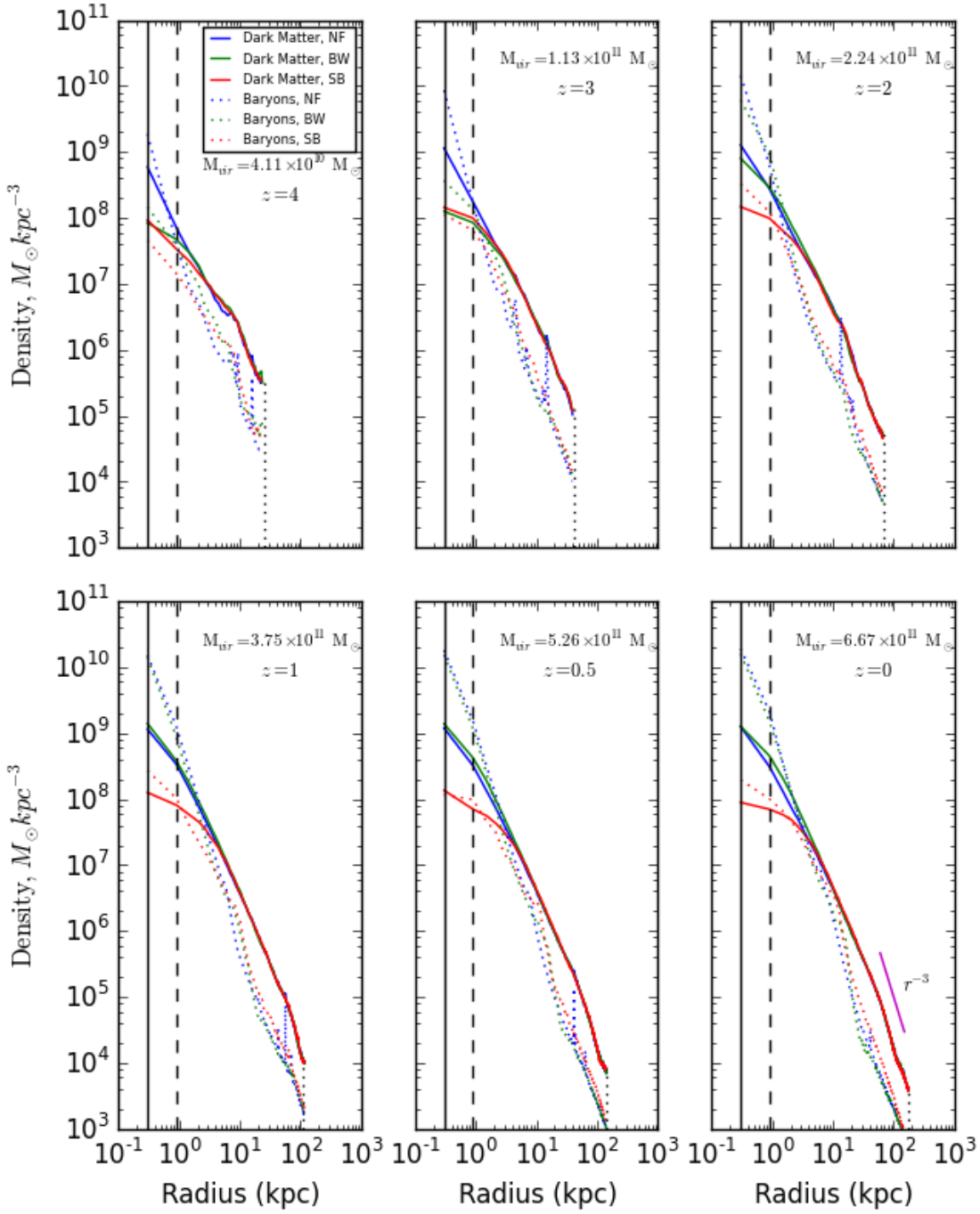

Figure 3.25: The density profiles of the dark matter (solid) and the baryons (dotted) for disk g1536. The red, green, and blue lines represent the results for SB, BW, and NF respectively.

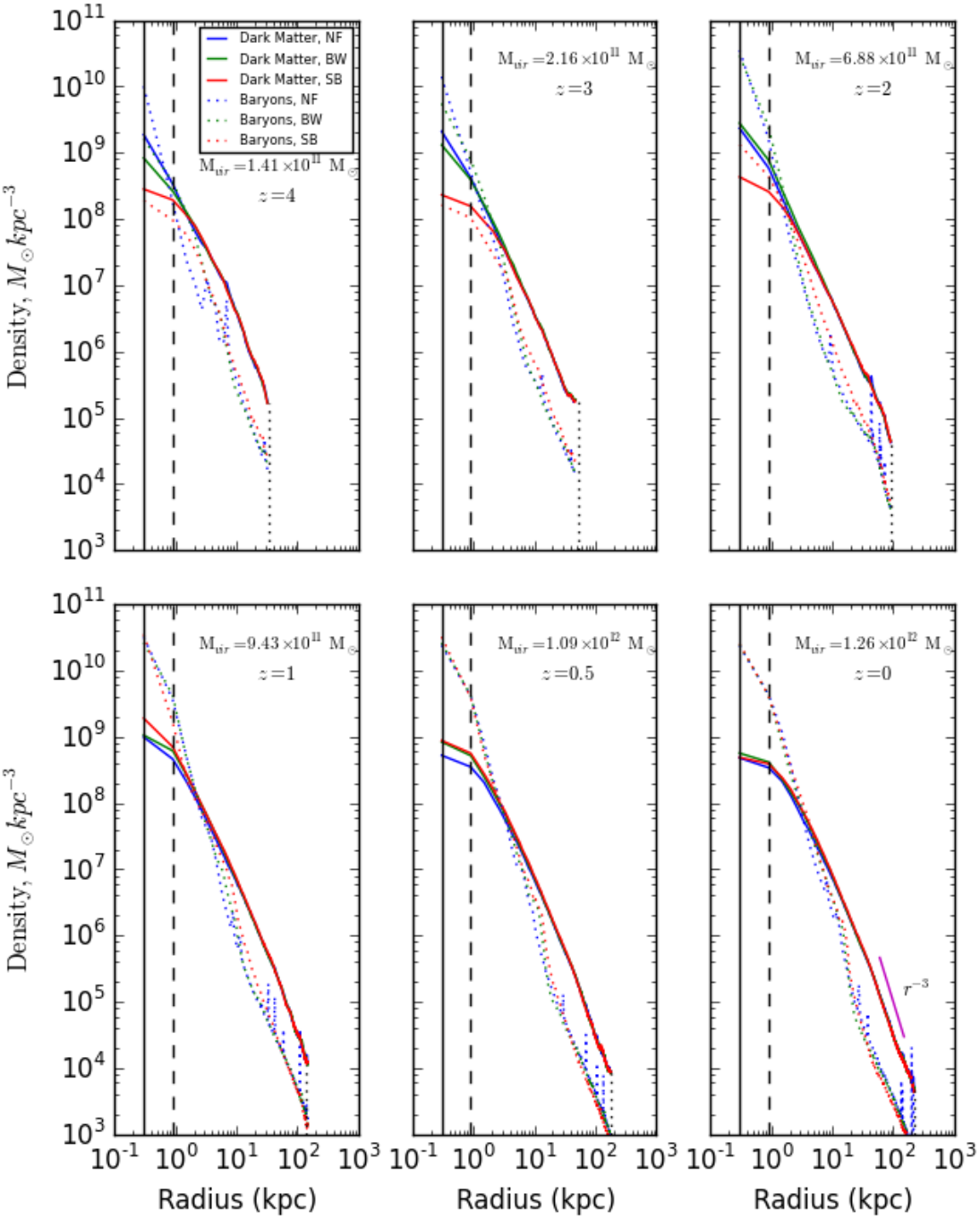

Figure 3.26: The density profiles of the dark matter (solid) and the baryons (dotted) for disk g15784. The red, green, and blue lines represent the results for SB, BW, and NF respectively.

3.3 Fuelling Star Formation through Gas Accretion

Star formation consumes the gas reservoir of the disk, leading to progressively lower SFRs for a fixed initial reservoir. Nevertheless, the Milky Way, and other galaxies in the local group, are observed to still be forming stars at modest rates. They must be accreting gas at a rate equal to or greater than the star formation rate, to sustain a constant star formation rate (generally speaking, though this can be made complicated by the density of the star forming gas). It is possible that this material comes from mergers; however, due to gas stripping, satellite galaxies merging with their host preferentially deposit their gas at radii larger than the star forming disk (Peek, 2009). The material could come from high velocity clouds of neutral hydrogen but, as discussed in a review by Sancisi et al. (2008), observations suggest that all the material from these clouds and any mergers yields a gas accretion rate of only ~ 0.2 $M_{\odot}$/yr. This is much lower than the star formation rate observed in nearby galaxies, approximately 1 $M_{\odot}yr^{-1}$(see Kennicutt & Evans (2012) and sources within), and so additional infall from the IGM is necessary.

Thus comparing the overall infall rate of a galaxy at a given radius with its star formation at said radius, is an investigation that tells us much about the balances between gas supply and consumption. This accretion rate is explored first by calculating the flux through a sphere with a radius of 30 kpc to find a general accretion rate of material into the system. We then consider the flow through a sheet, located 7 kpc above the disk, to analyze the flow from the 30 kpc sphere closer towards the disk system. Finally, we calculate the accretion rate of material through a series of annuli only 0.7 kpc above the disk. These annuli are of particular interest as we can compare the radial gas accretion with the star formation rate, which is applied with a radial dependence in semi-analytical star formation models. In all cases, we compare between the three different feedback mechanisms. We have already seen that different feedback mechanisms will impact the vertical velocity structure and the radial temperature structures of the disk and halo. Thus, indirectly, stellar feedback will

impact the way in which a galactic disk accretes material.

3.3.1 The General Accretion Rate: Flux through a Spherical Shell

There are two modes of accretion through the galactic halo. There is hot-mode accretion, which was discussed generally in section 1.1.2, when describing the collapse of baryons within a dark matter halo. As gas enters the galactic halo it hits the galactic accretion shock. If the gas is shocked then it must cool before it can collapse and accrete on to the galactic disk. There is also cold-mode accretion, in which particles remain cooler than 2.5×10^5 K, and radiate away energy. This cold material is never shocked, and accretes directly onto the disk. Work by Birnboim & Dekel (2003); Kereš et al. (2005) find that cold-mode accretion dominates in low mass halos, while hot-mode accretion dominates in high-mass halos. The precise baryonic mass of the galaxy is not important: a low mass galaxy inside of a halo with high baryonic mass will still be dominated by hot-mode accretion. This dependence of accretion mode on halo mass is due to cooling physics: a virial shock arises only when the post-shock cooling time is greater than the dynamical time. According to Kereš et al. (2005), a virial shock will persist when the halo mass is $\geq 10^{11.4}\mathrm{M}_{\odot}$. This can also be correlated with redshift, as low mass galaxies dominate at high redshift. Both disks considered here have halo masses greater than $2.5 \times 10^{11}\mathrm{M}_{\odot}$, so hot-mode accretion is anticipated to dominate the accretion processes.

To investigate the general accretion rate into the system, we consider the flux of material through a spherical surface centred on the minimum potential of the star particles, with a radius of $0.17R_{vir}$. This value was chosen such that the sphere around g1536 had a radius of 30 kpc, to match the work of Courty et al. (2010). The radius of the sphere around g15784 is approximately 38 kpc. Spherical geometries have been used to analyze gas flux in many works such as Dekel et al. (2013) and Keller et al. (2015). Each gas particle is projected forward linearly, by an amount of time δt_{proj}, using a range of prediction time steps so as to reduce the impact of fluctuations in the local density field. The mean mass found passing

through the sphere is normalized by δt_{proj}. Ideally we would analyze all time steps of the simulation to average over fluctuations, but that is not possible given the simulations are complicated. Figure 3.27 shows the process of projecting particles linearly forwards, and the colour scheme used when marking particles as inflowing or outflowing.

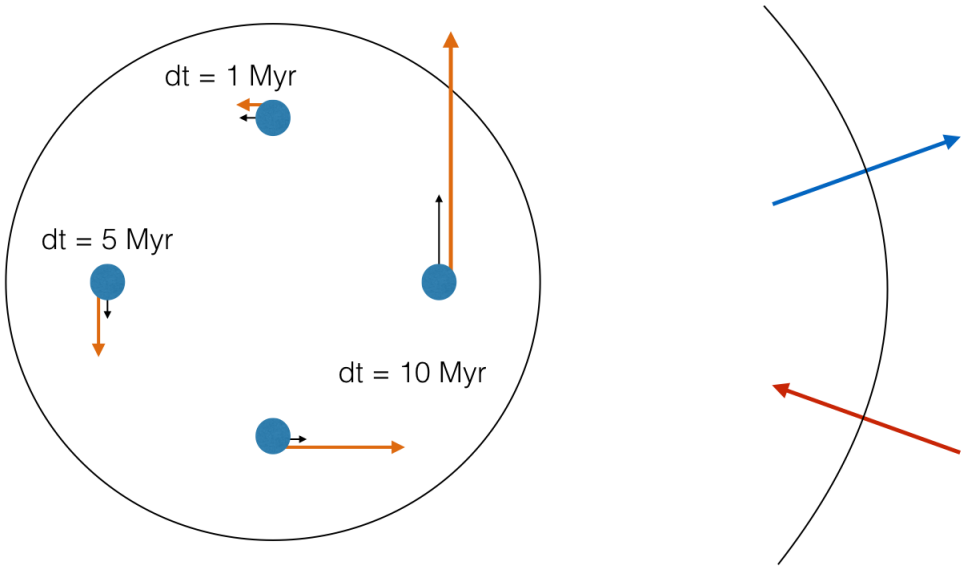

Figure 3.27: In the left figure: gas particles, blue, are projected linearly forward (orange vectors) according to their velocity (black vectors). The larger the projection time step, the further they are projected to go. For the same projection time step, a particle with a larger velocity is projected to go further. In the right panel: we see that inflowing particles are red, and outflowing particles are blue.

Figures 3.28 and 3.29 show the spherical flux for the g1536 and g15784 disks respectively. Figure 3.28 shows the fluxes for all three variations of g1536. The spherical flux is roughly constant for intermediate time steps, in the 10-50 Myr range. In the no feedback and blastwave cases the net flux is on the order of a few $M_{\odot}$/yr; similarly the inflow flux. The superbubble results are quite different. The inflow increases dramatically at very small projection steps. This is caused by a nearly constant mass crossing the boundary being averaged over small projection steps. This nearly constant mass comes from a cloud of

material close to the boundary, dominating the accretion rate at small prediction steps. This cloud is not present at earlier outputs for the SB disk, or in the BW or NF disks at $z = 0$.

Hence, to find an average accretion rate through the spherical surface at 30 kpc, we consider all the material which crosses the sphere using 5 projection steps from 10-50 Myr and average the mass crossing the sphere with each projection step. We then find that g1536_SB accretes ~ 4.6 $M_\odot$/yr, g1536_BW accretes ~ 1.5 $M_\odot$/yr, while g1536_NF accretes ~ 2.1 $M_\odot$/yr. g1536_BW would seem to accrete the least because it has a larger outflow than g1536_NF. In the rotation curves, figure 3.9, g1536_NF and g1536_BW had similar velocities in the plane of the disk; however material above the disk had larger velocities in the case of blastwave feedback than no stellar feedback. Material with larger velocities will be marked as outflow at lower projection steps. g1536_SB has the largest net accretion rate, and a very high inflowing accretion rate. In section 3.2.2 we postulated that g1536 may be about to accrete the large reservoir of cold gas populated by SB feedback. The very high inflow rate here would suggest that this accretion is beginning.

If we consider only the accretion rate of inflowing material, we see that g1536_SB accretes the most, followed by g1536_BW, and with g1536_NF accreting the least amount of material. The differences in the average accretion rates (and the inflowing accretion rates), indicate that stellar feedback is still affecting the flow of material 30 kpc away from the disk. This could suggest that the range of feedback is greater than 30 kpc, or that the effects of feedback persist for long periods of time (that is, we are either seeing the effects of recent feedback, or we are seeing signatures of the feedback history).

Figure 3.29 shows the spherical flux results for g15784. The inflowing flux is roughly constant from 10-50 Myrs, as seen in the case of g1536. Material in g15784 outflows vary drastically at projection steps greater than 50 Myrs. This is not a physical outflow however; g15784 is twice as massive as g1536 and so material within g15784 has greater rotational velocity; when projected linearly forward more material passes through the spherical bound-

ary at smaller projection steps than g1536. This is exactly the case shown in figure 3.27, for the example prediction step, $dt = 10$ Myr. Unlike g1536, there do not seem to be any clouds affecting the results of our spherical fluxes at small projection steps. The fluxes look very similar across all feedback mechanisms; as expected from previous results.

The average accretion rate is calculated for g15784 in the same way as g1536. We find that g15784_SB accretes ~ 2.5 $M_\odot$/yr, g15784_BW accretes ~ 1.2 $M_\odot$/yr, and g15784_NF accretes ~ 2.5 $M_\odot$/yr. These inflow rates are likely related to the disk masses discussed. g15784_SB shows larger infall rates than g15784_BW, the most massive disk, and the lowest temperatures in the radial regime around the disk.

We find that all six disks have a general accretion rate on the order of $1-5 M_\odot yr^{-1}$. This accretion rate is in good agreement with observed accretion rates, and those implemented in semi-analytical models of galaxy formation (observations: (Regan et al., 1997; Leitner & Kravtsov, 2011), semi-analytical models: (Dekel et al., 2013; Casuso & Beckman, 2001; Lacey & Fall, 1985)). In particular we find that these fluxes through a sphere of $0.17R_{vir}$ are in good agreement with the $z = 0$ results of Courty et al. (2010), who found accretion rates of approximately 2 $M_\odot$ yr^{-1} through a spherical shell at 30 kpc.

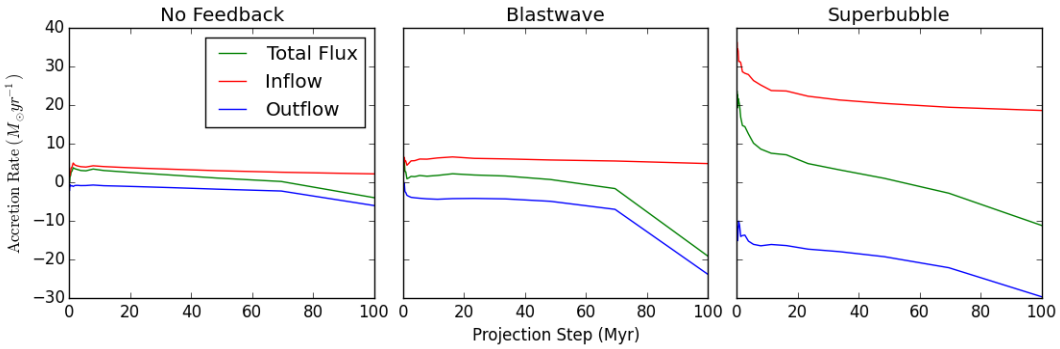

Figure 3.28: Flux through a 30 kpc sphere for g1536 at $z = 0$

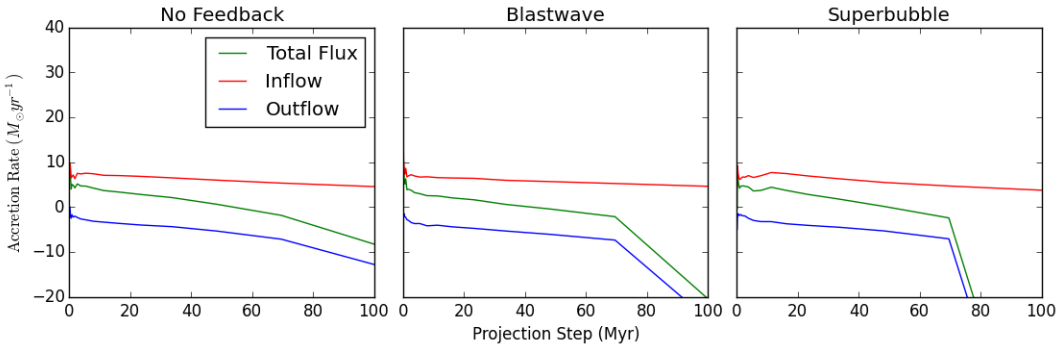

Figure 3.29: Flux through a sphere for g15784 at $z = 0$

3.3.2 Accretion onto the Disk: Flux through the sheet and Annuli Geometries

The general theory of hot-mode accretion says little about how material actually accretes onto the disk, i.e.. at what radius and in what direction. To investigate this, we looked at the flux of gas through two different geometries: a sheet located 7 kpc above the disk, and a series of annuli located just above the disk (diagrams of the sheet and annuli geometries in relation to the disk can be seen in the right-most panel of figure 3.4).

Sheet Geometry

The sheet geometries were inspired by the work of Courty et al. (2010) who considered a sheet 7 kpc above the plane of the disk, with a radius of 17 kpc (though here we have increased the radius to 30 kpc, to investigate possible flux beyond the disk). The annuli geometry was implemented to investigate gas flux close to the disk in relation to the radius, as well as any possible radial motion of the gas close to the disk. The relationship between accretion rate and radius is particularly important, as semi-analytical models of star formation, and the sub-grid star formation applied in hydrodynamical simulations, calculate the star formation rate as a function of local density (which depends on radius). In these

particular GASOLINE2 simulations, stars form at a rate such that

$$\dot{\rho}_* = c_* \frac{\rho_{gas}}{t_{ff}} \tag{3.2}$$

The local free-fall time of the gas, t_{ff}, also depends on the local gas density, and the star formation rate will be proportional to $\rho_{gas}^{3/2}$. If we assume local gas density falls with radius, this gives a star formation rate which will be higher at the centre of the disk than at the edge of the disk. In order for the star formation rate to be constant in time, at all radii, gas would need to be supplied at higher rates to the centre of the disk than the edges. In practise our scale lengths show that the fall off in density of cold gas is less strong than anticipated based upon usual, i.e. exponential, surface density expectations.

The particle flux in the annuli and sheet geometries is calculated using projection time steps $dt_p = [1 - 10]$Myr, and averaged to account for fluctuations in the local density field. Smaller projection steps are used as compared to the spherical geometry because the velocities of particles are higher when closer to the disk, leading to faster dynamical times. The average is implemented with the intention of minimizing the effects of large clouds that might pass through the surface at later time steps but not earlier (exactly the situation seen in the spherical flux of g1536_SB).

A diagram of the sheet geometry is given in figure 3.30. The sheet has a radius of 30 kpc, and is located 7 kpc above the disk. Material with temperatures less than 10^4 K is marked as cold, material with temperatures greater than 10^4 K is marked as hot. Inflowing and outflowing material is marked with solid, and dot-dashed lines respectively. Figures 3.31 and 3.32 show the flux through the sheet geometry for g1536 and g15784 respectively. The total flux is calculated as $hot_{in} + cold_{in} - hot_{out} - cold_{out}$.

We begin by considering the accretion through the sheet for g1536_NF. As expected, there is no cold inflow or outflow because there is no cold material in the disk. There is approximately 1 $M_\odot yr^{-1}$ of hot inflowing gas, and very little hot outflowing gas. The

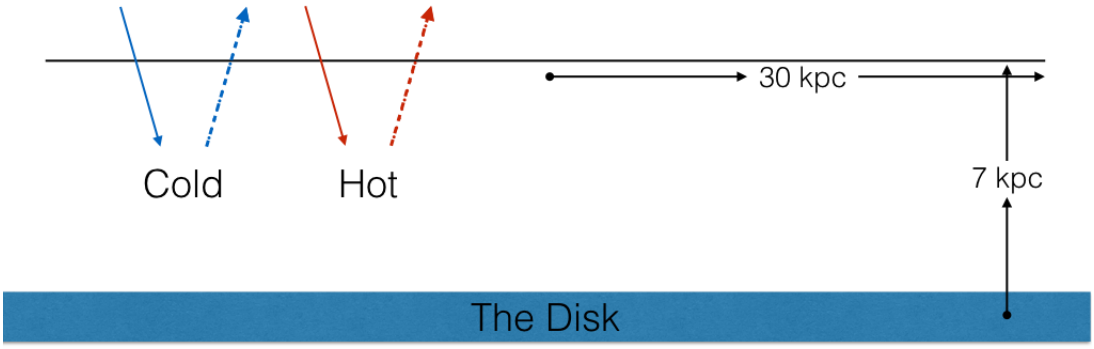

Figure 3.30: The sheet is located 7 kpc above the disk, with a radius of 17 kpc. Hot and cold material is tagged as red or blue, and inflowing and outflowing material is shown in solid, or dot-dashed lines.

amount of material flowing in through the sheet is similar in magnitude to the average accretion rate through the sphere. Disks modelled without stellar feedback are obviously not driving outflows, so it is expected that the hot inflow through the sheet would approximately agree with the inflow rate through the spherical shell. Otherwise the circum-galactic medium would grow in mass relative to the disk.

The disks evolved with stellar feedback do contain cold material, and in all cases show a cold inflow dominating over a cold outflow. This is expected due to the nature of the feedback algorithms implemented: feedback is applied as thermal energy so we expect outflows to be dominated by hot material, and cold outflows to be minimal. The accretion of hot material onto the disk of g1536_BW is similar in magnitude to g1536_NF, $\sim 0.5 - 1$ $M_{\odot}yr^{-1}$. This signifies that BW feedback is not ejecting a significant amount of material beyond a height of 7 kpc. g1536_BW shows cold inflow through the sheet at a similar rate of $\sim 0.5 - 1$ $M_{\odot}yr^{-1}$.

g1536_SB show larger inflow and outflow rates than the BW or NF disks. At radii close to the disk edge, the hot outflow peaks at 6 $M_{\odot}yr^{-1}$. Furthermore, g1536_SB accretes more cold material, at a maximum rate of 4 $M_{\odot}yr^{-1}$. Similarly to the spherical flux, this could

represent the beginning of the accretion of the cold gas reservoir onto the disk of g1536_SB. SB feedback drives hot outflows at a rate of ~ 1 $M_{\odot}yr^{-1}$. This is similar to g1536_BW, indicative of their similar star formation rates at $z = 0$.

g15784_NF is similar to g1536_NF. Hot material accretes inwards at a rate of $0.5 - 1$ $M_{\odot}yr^{-1}$, similar to the accretion rate through the sphere. There is no cold inflow or outflow. g15784_BW shows very little cold inflow and outflow, while hot material is accreted and ejected at a rate of $\sim 0.5-1$ $M_{\odot}yr^{-1}$. g15784_SB shows much more cold inflow, peaking around 2 $M_{\odot}yr^{-1}$, possibly a sign that g15784_SB continues to accrete cold material from the halo. Unlike g1536_SB, g15784_SB drives more massive hot outflows than its BW counterpart, at $\sim 1 - 2$ $M_{\odot}yr^{-1}$. However, this is expected due to the difference in their star formation rates, $\sim 4 - 5$ $M_{\odot}yr^{-1}$.

We can compare these results with the results of Courty et al. (2010). They find no cold material flowing through their sheet geometry, and hot material accretes at a rate of 2 $M_{\odot}yr^{-1}$. The simulations analyzed by Courty et al. (2010) use blastwave feedback, and their results are in moderate agreement with g1536_BW and g15784_BW. Both disks here show less inflow which could be the result of taking a single unrepresentative output. In section 3.3.3, we consider the flux of multiple simulation steps.

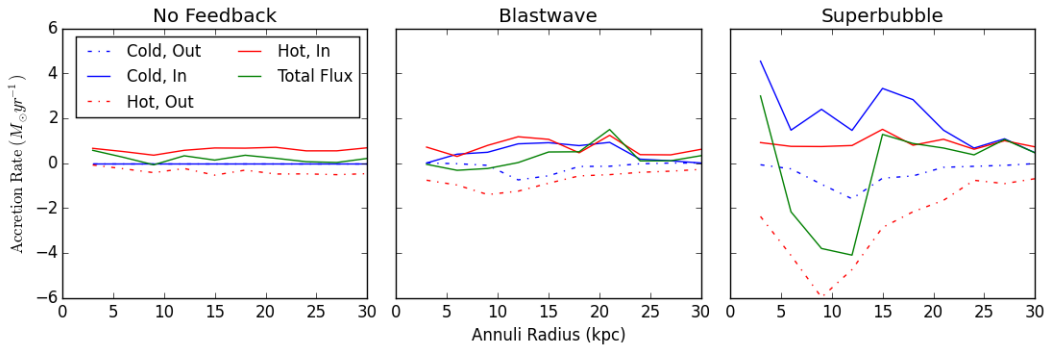

Figure 3.31: Flux through a sheet for g1536 at $z = 0$

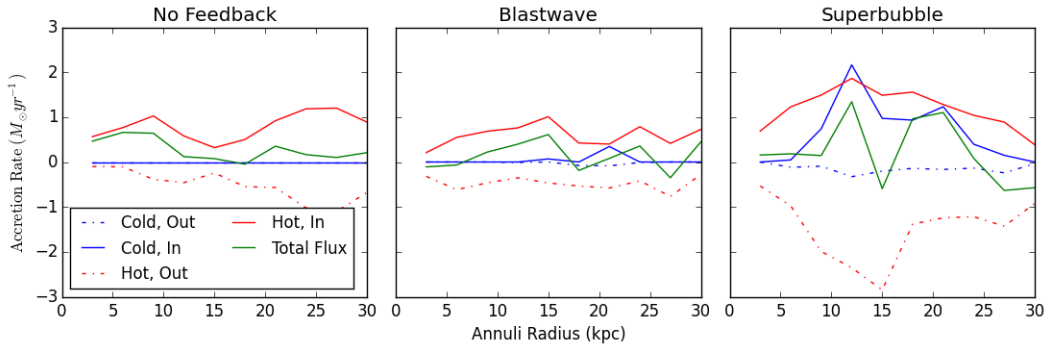

Figure 3.32: Flux through sheet for g15784 at $z = 0$

Annuli Geometry

The gas flux was also calculated through annuli, a diagram showing the geometry can be seen in figure 3.33. The annuli are located 0.7 kpc above and below the disk, and extending to 2 kpc above and below the disk. Each annulus has a width of 3 kpc. The inner radius of the annuli is 3 kpc, to avoid the bulge region of the disks. The flux into the annuli is split into three parts. Material moving through the top of the annuli is red, while material moving through the bottom face of the annuli is magenta. Material flowing into the annuli is shown as solid lines, while material moving out of the annuli is shown as dot-dashed lines.

Consider a particle moving completely through the annuli to accrete onto the disk. It will increase the material flowing in through the top face of the annuli (the solid red line), and the material moving out through the bottom face of the annuli (the dot-dashed magenta line). The equivalent will be true for a particle ejected from the disk, and moving completely through the annuli, showing as increases in the material flowing into the bottom face of the annuli (the solid magenta line), and out through the top face (the dot-dashed red line).

Figures 3.34 and 3.35 show the fluxes through the top and bottom faces of the annuli, for g1536 and g15784 respectively. In both disks evolved without stellar feedback, there is less material flowing through the annuli than the BW or SB by approximately an order of

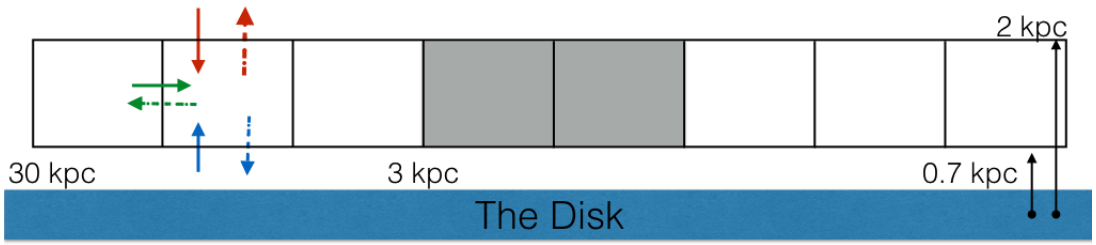

Figure 3.33: A diagram of the annuli geometry. Material flowing into the annuli volume is shown with solid lines, while material moving out of the annuli volume is shown with dot-dashed lines. The filled grey region is not considered in the analysis, to avoid the bulge

magnitude. There is a small amount of material, 5 $M_\odot$ yr^{-1} moving through the bottom surface of the annuli, showing roughly equal amounts moving into the annuli as moving out. The outflowing material entering the annuli through the bottom face is likely caused by turbulence, driven by resonances in the disk (as opposed to outflows that might be driven by stellar feedback).

We now consider disks evolved with BW feedback. In both, there are roughly equal amounts of inflow and outflow beyond the disk radii, 17 kpc. 2 kpc away from the disk through the top face of the annuli, 10 $M_\odot yr^{-1}$ flows both inwards and outwards. This is likely material driven through the annuli by feedback (but not as far as the sheet), and falling back down onto the disk again. Differences between outflow and inflow through the top face represent the accretion of new material. Material flows through the bottom face of the annuli at rates 2-4 times larger than through the top face, $20 - 40$ $M_\odot yr^{-1}$. This indicates that turbulence in the atmosphere above the disk may be a large factor in the flow through the bottom face, but not the top face, of the annuli. Differences in the flow in and out through the bottom face of the annuli suggest the true accretion rate onto the disk. In the outer region of the disk, approximately 10 $M_\odot yr^{-1}$ flows out of the bottom face and onto the disk (magenta dot-dashed line).

As discussed in Keller et al. (2015), g1536_SB drives more massive outflows than g1536_BW. This is seen in the annuli fluxes of g1536_SB. 55 $M_\odot yr^{-1}$ of material flows

through the bottom face of the annuli, away from the disk (solid magenta). In radii coincident with the disk of g1536_SB, outflow dominates over inflow. This is further suggesting that some of the material ejected by SB outflows joins the halo potential, rather than falling back onto the disk. The flux inwards through the top face of the annuli (solid red), is similar in magnitude to that of g1536_BW.

In g15784_SB, the flow through the bottom of the annuli, 0.7 kpc from the disk, is very similar to that of g15784_BW, 40 $M_{\odot}yr^{-1}$. As we have discussed in many previous sections, the differences between g15784_BW and g15784_SB incorporate different physics compared to the results of g1536. The gravitational binding energy of g15784 is dominant over the energy returned to the ISM by stellar feedback. Inflow and outflow through the top of the annuli, 2 kpc away from the disk, are similar in magnitude: 10 $M_{\odot}yr^{-1}$.

Generally, the annuli geometry show that material accretes directly onto the disk, as opposed to at larger radii and spiralling inwards in the equatorial plane. While the inflow through the sphere can possibly be connected with the cold inflow through the sheet, there is no such connection possible with the annuli geometry. The annuli region is much more active and complicated, and any trace of inflowing signature is lost. Outflows are driven in the disks which include stellar feedback, and superbubble feedback produces a more massive outflow than blastwave in a less massive galaxy. Little can be said about the radii at which inflow or outflow might dominate. The results show no distinct trend and have scatter. Section 3.3.3 attempts to reduce this noise.

Figures 3.36 and 3.37 show the flux through the side faces of the annuli in both disks. The solid green line shows material moving radially inwards (through the side faces of the annuli), while the dot-dashed line represents the flux of material moving radially outwards. As with the top and bottom faces of the annuli, there is very little flux through the sides of the annuli in the case of the disk evolved without stellar feedback (for both g1536 and g15784).

In the disks evolved with stellar feedback, there are large amounts of material mov-

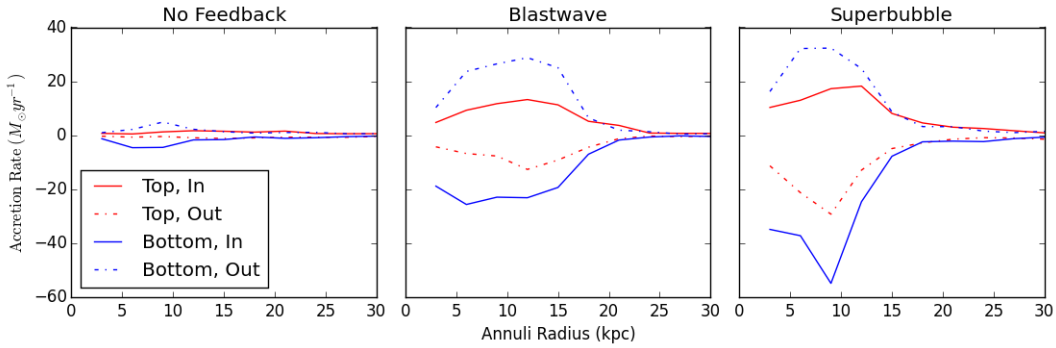

Figure 3.34: Flux through annuli for g1536 at $z = 0$

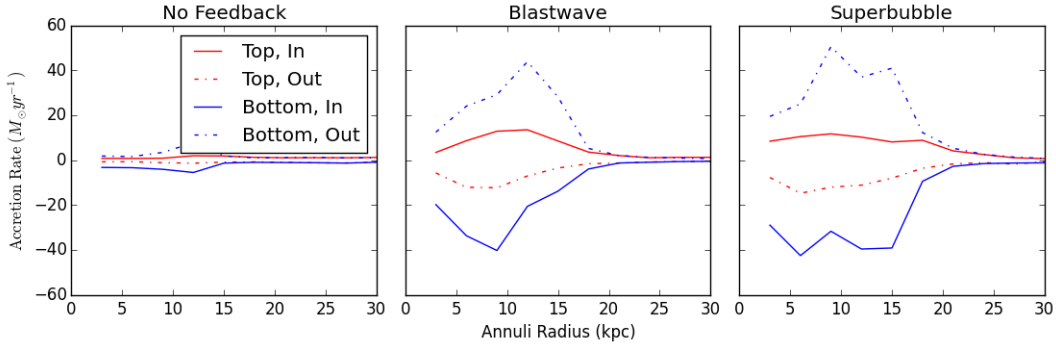

Figure 3.35: Flux through annuli for g15784 at $z = 0$

ing radially outwards within the annuli, and systematically less material moving radially inwards. In the case of g1536, there is 5 $M_\odot yr^{-1}$ more material flowing radially outwards than inwards. In the case of g15784, there is 15 $M_\odot yr^{-1}$ more material flowing radial outwards than inwards. The differences between the inward and outward motion are more pronounced at radii coincident with the disk; little material moves radially beyond the disk edge.

The largest discrepancies between inward and outward flow are seen in the disks evolved with SB feedback. There is overall less radial motion in g1536_BW and g15784_BW than in g1536_SB and g15784_SB. As expected, the differences between g15784_BW and g15784_SB are less pronounced than those in g1536.

The radial outward flow is further evidence of the outflows driven by supernovae. As

material is ejected from the disk, it does not move solely upwards, but flows with a radial velocity component as well. This is analogous to the disk winds driven by accretion disks around young stars and black holes.

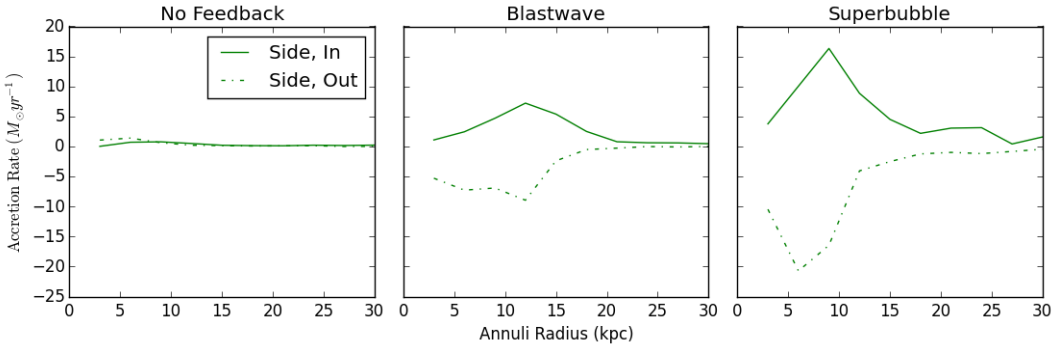

Figure 3.36: Radial flux through annuli for g1536 at $z = 0$

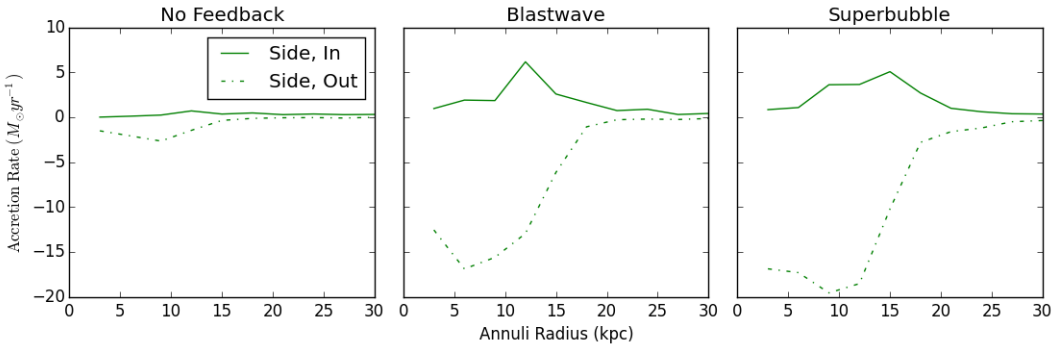

Figure 3.37: Radial flux through annuli for g15784 at $z = 0$

3.3.3 Reducing Scatter via Co-Added outputs

Although there were some trends visible in the accretion rates of the last section, many of the results were too noisy to make strong predictions about the gas accretion onto a galaxy (particularly regarding the radial dependence). To reduce noise, we co-add the fluxes from the last three simulation outputs. This essentially averages the fluxes being considered over 214 Myr. Again, it would be most ideal to average the results over many individual time steps, but this is not possible as the outputs have not been saved.

The co-added spherical fluxes are shown in figures 3.38 and 3.39. The results are not very different from their un-averaged counterparts. This implies that the flux through the spherical surface is nearly constant over the simulation outputs used. For g1536, the accretion rate through the spherical shell is 3.7 $M_\odot yr^{-1}$, 2.5 $M_\odot yr^{-1}$ and 2.0 $M_\odot yr^{-1}$ for the g1536 SB, BW, and NF cases respectively. We see higher rates of inflow in SB than in the BW or NF cases. This is consistent with the results found when using only the last simulation output.

For the g15784 disks the accretion rates through the spherical shell are equal to 2.9 $M_\odot yr^{-1}$, 1.3 $M_\odot yr^{-1}$, and 1.2 $M_\odot yr^{-1}$ for the NF, BW, and SB feedback cases respectively. As with the results using only a single output, g15784_SB is accreting the most material.

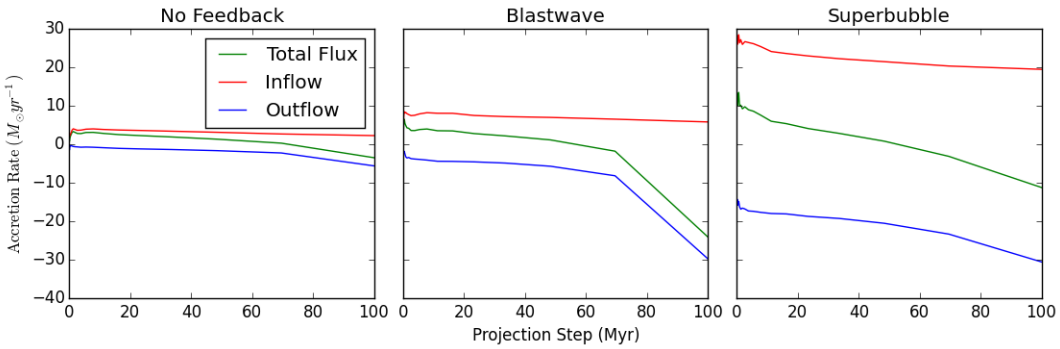

Figure 3.38: Co-added flux through sphere for g1536. The input is averaged over $z = 0, 0.008, 0.016$

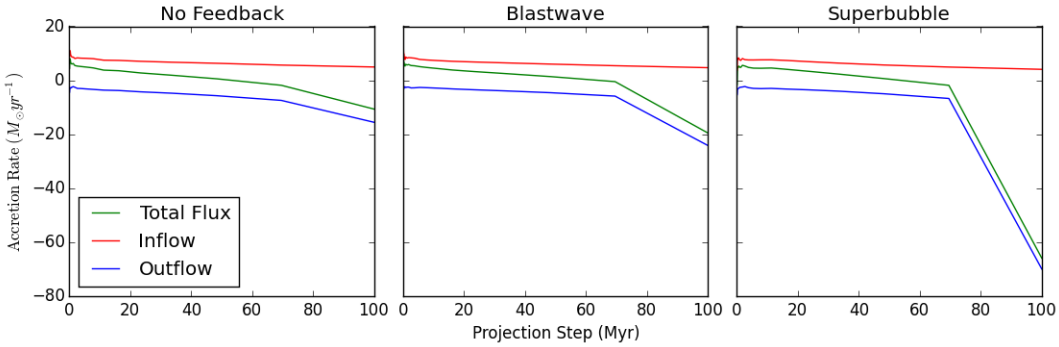

Figure 3.39: Co-added flux through sphere for g15784. The input is averaged over $z = 0, 0.008, 0.016$

We now turn our attention to the results of the fluxes through the sheet and annuli geometries, and the analysis of the radial dependence of gas accretion. The fluxes through the sheet were improved by co-adding three simulation outputs, as seen in figures 3.40 and 3.41. In all cases the hot flux flowing inwards has been smoothed by the averaging process, approaching a constant hot inflow of $0.5-1.5$ $M_{\odot}yr^{-1}$. The noise in the flux of cold material has been reduced in the case of g1536. In g1536_BW cold material flows in through the sheet at a rate of 0.5 $M_{\odot}yr^{-1}$. This can be compared with g15784_BW, where very little cold material moves through the sheet (the spike in accretion at $r = 12$ kpc is likely a cloud of cold material passing through the sheet).

The cold inflow of g1536_SB is smoothed by the co-adding process; the accretion rate is constant at 2.0 $M_{\odot}yr^{-1}$ at radii coincident with the disk. Beyond the disk edge, the cold inflow drops. The cold inflow of g15784_SB is still too noisy to conclude anything about the accretion rate's radial dependence.

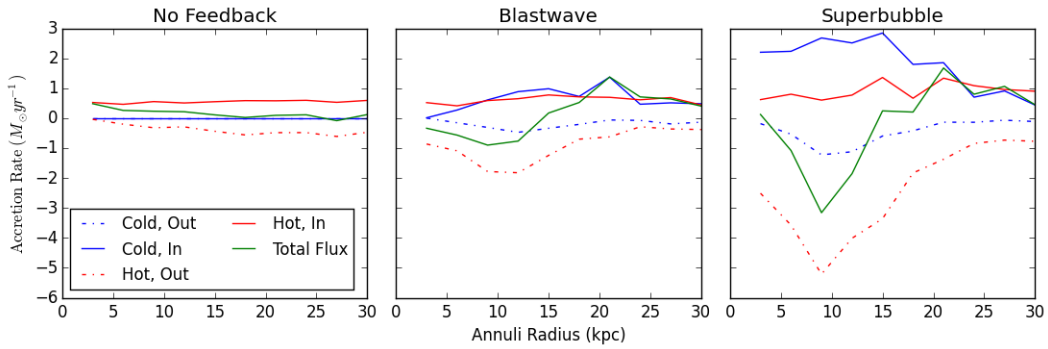

Figure 3.40: Co-added flux through sheet for g1536. The input is averaged over $z = 0, 0.008, 0.016$

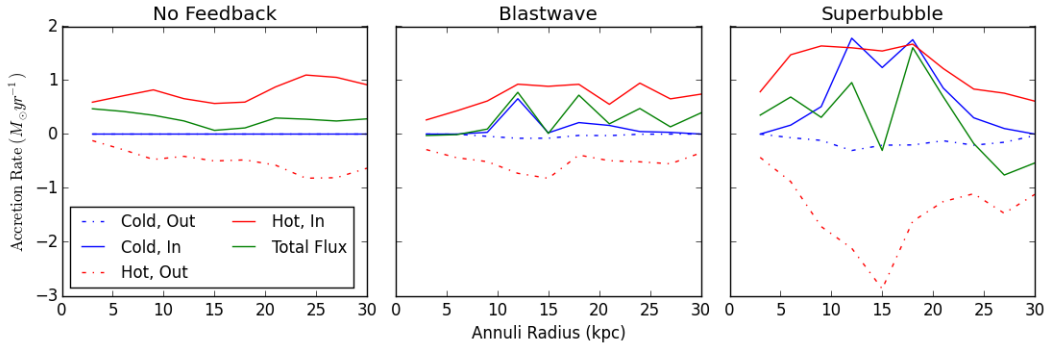

Figure 3.41: Co-added flux through sheet for g15784. The input is averaged over $z = 0, 0.008, 0.016$

Figures 3.42 and 3.43 show the co-added annuli fluxes through the top and bottom faces. The averaging process does not change the results for disks evolved without stellar feedback. The averaged BW and SB disks show nearly symmetric inflow and outflow. The region immediately above the disk is too stochastic to truly analyze in this way. In all cases, the material flowing through the annuli drops significantly beyond radii coincident with the disk edge. This does confirm that most material accretes at small radii, as opposed to large radii and spiralling inwards.

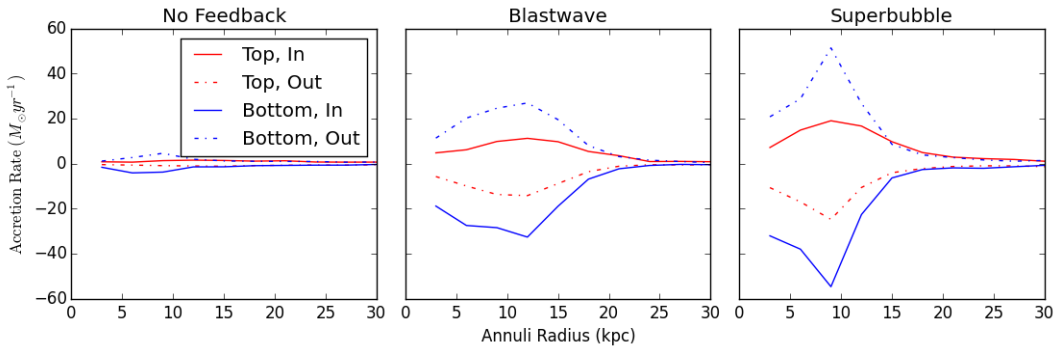

Figure 3.42: Co-added flux through annuli for g1536. The input is averaged over $z = 0, 0.008, 0.016$

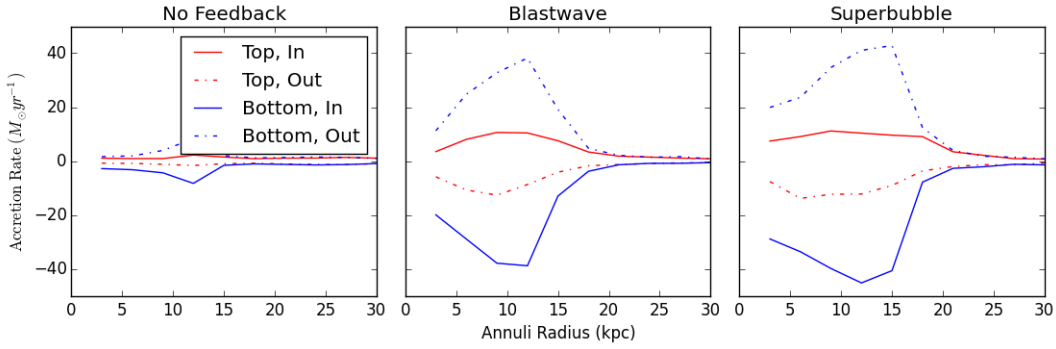

Figure 3.43: Co-added flux through annuli for g15784. The input is averaged over $z = 0, 0.008, 0.016$

In figures 3.44 and 3.45, we see the co-added fluxes through the sides of the annuli for g1536 and g15784. These figures are nearly the same as their un-averaged counterparts of the previous section. The star formation rates of all disks were constant at low redshifts; therefore we expect stellar feedback, when implemented, to be constant at low redshift as well. Unlike the co-added mass flux through the top and bottom faces of the annuli, through the sides outflows dominate over inflow where stellar feedback is implemented. As discussed in the previous section, this radially directed flux is likely a measure of outflow; ejected material accelerates in the radial direction as it moves away from the disk. All inflowing motion through the side faces of the annuli peak at a radius coincident with the disk edge.

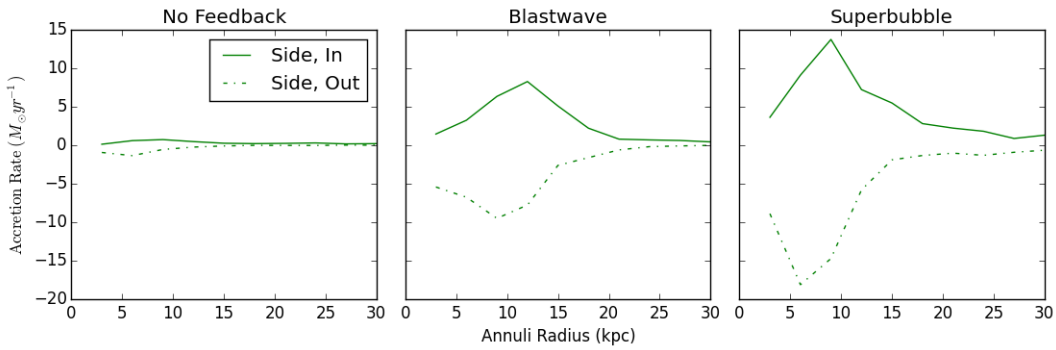

Figure 3.44: Co-added radial flux through annuli for g1536. The input is averaged over $z = 0, 0.008, 0.016$

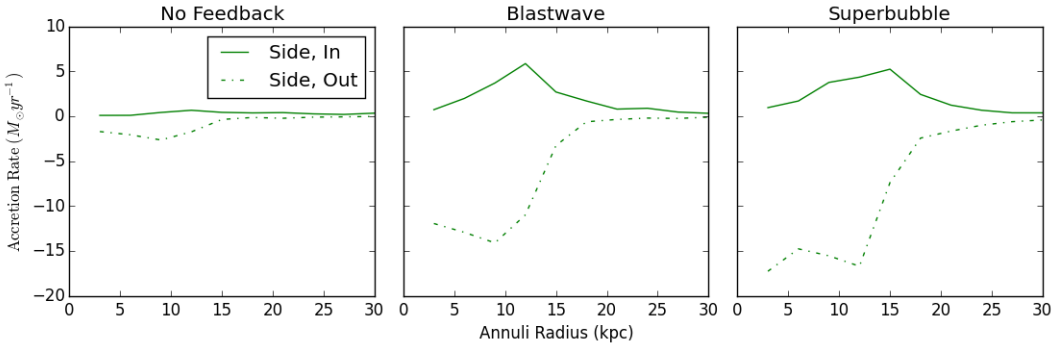

Figure 3.45: Co-added radial flux through annuli for g15784. The input is averaged over $z = 0, 0.008, 0.016$

Chapter 4

Discussion and Conclusions

Firstly, we have confirmed what the history of galactic simulations suggest: including stellar feedback produces substantially different disk morphologies compared to disks evolved without. Without feedback, disks are thin and truncated, seen quantitatively in the scale heights and break radii of the gas profiles, but also visually in the smoothed gas density plots. These disks also show a complete absence of cold gas, because it will immediately condense to form stars without a heating mechanism to balance cooling. Relatedly, disks evolved without stellar feedback have a star formation history which peaks around $z = 3-5$. Including stellar feedback delays the star formation peak, and reduces the maximum SFR.

Secondly, we find that the differences in disk morphologies extend to those disks evolved with BW or SB feedback. That is, disks will evolve differently depending on how stellar feedback is implemented. Disks evolved with SB feedback are more vertically extended than their BW counterparts, but smaller in radius. SB disks are also colder and denser than their BW counterparts. This may seem counter-intuitive; why would more efficient heating mechanisms lead to a surplus of cold material? More efficient heating delays star formation, and prolongs the lifetime of gas within the disk. There is more cold material in disks evolved with stronger stellar feedback algorithms because there is more gas available

to cool; unlike in disks evolved without stellar feedback, where much of the available gas has formed stars. Star formation in disks evolved with BW feedback experience a star formation peak around $z = 2$, while SB feedback delays the peak until after $z = 2$.

Galaxies evolved with SB feedback show greater accretion rates through a spherical shell 30 kpc away from the disk than those evolved with BW or NF feedback. Through a slab located 7 kpc above the disk, galaxies evolved with SB feedback show cold accretion, while disks evolved with BW or NF show predominantly hot accretion, punctuated by cold clumps. SB feedback drives hot outflows which eject material to distances beyond 7 kpc, possibly escaping the disk entirely. Close to the disk, signals of accretion are lost due to the more massive outflows, and general turbulence close to the disk. There are radial flows outwards, considered to be further evidence of feedback driven outflows from the disk. These radial flows are easier to measure, compared to the general accretion rate, because they are more localized.

Thirdly, we find that the effects of SB feedback depends on the mass of the disk being considered. In less massive disks, SB feedback is capable of preventing bulge formation, and centrally peaked velocity profiles, which BW feedback cannot do. However, g15784, with disk mass greater than 10^{11} $M_{\odot}$, develops a bulge regardless of feedback algorithm (as seen in the rotation curves), likely because at this mass AGN feedback is necessary to disturb this low angular momentum material. Modelling this halo mass will likely require more detailed models for AGN.

SB feedback is also capable of preventing baryonic collapse below a disk mass of 4×10^{10} $M_{\odot}$, which can prevent the dark matter density profile from following the NFW profile in the central region of the galaxy. This is seen in the low-mass galaxy, g1536, at $z = 0$ and the high-mass galaxy, g15784, at $z = 2$. The DM density profile of g15784 is seen to visibly steepen between $z = 2$ and $z = 1$, coincident with the onset of star formation.

Lastly, and perhaps most importantly, we find that above some threshold disk mass, SB feedback triggers accretion onto the disk. Generally speaking it is expected that more

efficient feedback will result in a less massive baryonic disk. However, it appears that SB feedback ejects enriched material into the halo. This enriched material will cool, and trigger cooling of halo material due to the thermal conduction algorithm implemented. BW feedback will also enrich the halo, but without the thermal conduction algorithm, the cooling of halo gas is less efficient. This creates a cold gas reservoir in the inner 50 kpc of the halo. We find when the disk mass is greater than $\sim 4 \times 10^{10} M_{\odot}$, the gravitational potential is large enough to trigger the accretion of this reservoir. This is particularly evident when investigating the gas mass marked as inflowing or outflowing in the halo. Disks evolved with SB feedback initially show more outflowing gas than either the BW or NF disks, but this behaviour 'turns-over' as the disk mass increases above the mass threshold. Beyond this critical mass, SB feedback triggers accretion by enriching halo material, reducing cooling times, and will create a more massive disk than BW feedback.

This 'positive' feedback is a surprising result with applications to recent galactic observations. Courtois et al. (2015) found a population of massive galaxies which were over-massive given where their rotational speed placed them on the baryonic Tuller-Fisher relationship. Further, they found that they were located preferentially in cosmic filaments. It is possible that our 'positive' feedback scenario provides a mechanism for the growth of these over-massive galaxies. A filamentary environment could build up more gas in the halo of a galaxy. There would be more gas available to cool after enrichment through SB feedback, and to possibly accrete onto the disk. Not every galaxy in a filament environment would become over-massive, just those beyond the disk threshold mass we have found necessary to trigger accretion. The galaxies which are marked as 'over-massive' by Courtois et al. (2015) exist beyond a baryonic mass of $\sim 10^{10.6} M_{\odot}$. This value is approximately equal to $4 \times 10^{10} M_{\odot}$, the threshold disk mass necessary to begin to accrete the cold gas reservoir out of the halo. This agreement in mass range is very promising and warrants further investigation.

4.0.1 Limitations

As for all numerical studies, this work is limited by several factors that prevent us from drawing concrete conclusions. First, only two disks of different masses were analyzed to find the threshold mass of $\sim 4 \times 10^{10} M_{\odot}$. To firmly conclude whether there is some transition in mass which triggers accretion, more disks evolved with all three feedback mechanisms would need to be examined. Such an ensemble study would be straightforward to do, but would consume many CPU hours.

In analyzing the dark matter density plots, we found that SB feedback may be capable of heating the central regions of the galaxy to the point that density contractions in the baryons, which would condense the dark matter along with them, are prevented. The region at which this effect is most pronounced is within 0.9 kpc, which is only three times the softening length, 312.5 pc. Increased spatial resolution, and a decreased softening parameter, would allow for this interesting central region to be more thoroughly investigated.

Finally, the investigation of how particles accrete onto the disk was severely limited by the scatter in the results. This scatter was mediated slightly by averaging the final three simulation snapshots, but no more could be used before the timescale separating the snapshots was non-negligible in terms of the evolution of the galaxy. Finer spacing between these snapshots would allow more snapshots to be used in this averaging process; more effectively reducing the impact of scatter on the analysis done. Furthermore, if the overall resolution of the simulations were improved, the mass of individual particles could be decreased. Currently, a gas particle has a mass of $\sim 2.5 \times 10^{5} M_{\odot}$. If a single particle is projected forward 10 Myrs and passes through one of the geometries considered in section 3.3, it will contribute ~ 0.25 $M_{\odot}$ yr^{-1}. This is particularly relevant when considering the spherical geometry, where the net accretion is as low as ~ 1 $M_{\odot}$ yr^{-1}. One more particle crossing the boundary, in either direction, could change the measured net accretion by up to 25%.

4.0.2 Future Work

The analysis completed here could be improved by increasing the numerical resolution of the simulations, and increasing the number of outputs around key redshifts. These results could also be further investigated by expanding the simulations to include AGN feedback. This would be particularly helpful in understanding the SB fuelled cold gas reservoir. Keller et al. (2015) argued that AGN feedback will dominate over stellar feedback in galactic haloes with virial masses greater than $10^{12}M_{\odot}$. Would AGN feedback prevent the overmassive g15784_SB from developing? This will depend on the amount of cold gas funnelled into the nuclear region, and the size of the bulge which forms. Future studies should investigate whether heating from AGN feedback prevents the formation and subsequent accretion of a cold gas reservoir in the halo. Furthermore, the metallicity of the gas could be included in the analysis of gas accretion onto the disk of the galaxy. Both BW and SB feedback algorithms return metals to the gas affected by feedback. Thus, the metallicity of gas particles could be used to distinguish between accreting material which is returning to the disk (enriched) and material which is being freshly accreted (presumably not enriched). This would be complicated by gas which is being freshly accreted onto the disk of interest, but was previously enriched in a satellite system. Finally, the study of accretion onto the disk could be further improved by using a particle tagging method; following a particle trajectory exactly through time, rather than linearly projecting the particles forward.

Appendix A

Scale Heights and Radii

For completeness, we include here all of the surface density plots used to calculate the scale radii and heights included in 3.2.

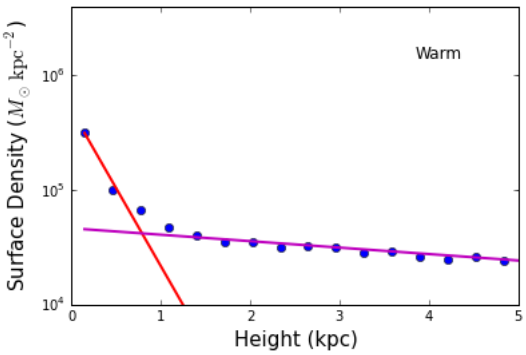

Figure A.1: For g1536_NF: The surface density of warm gass is plotted against height. An inner profile is fit in red, and an outer profile is fit in magenta.

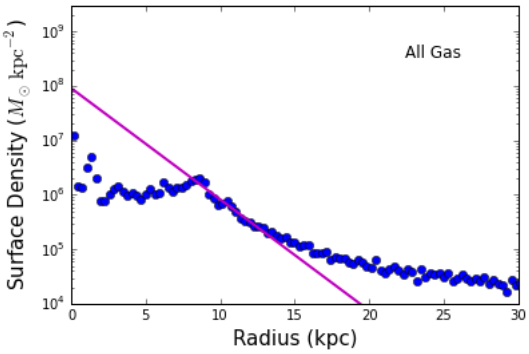

Figure A.2: For g1536_NF: The surface density of all gas plotted against radius. The break point, separating the outer and inner profiles, is used to define the edge of the disk.

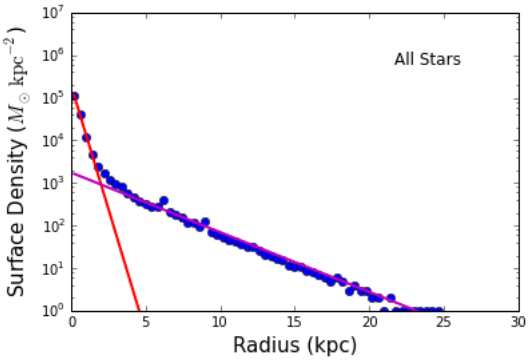

Figure A.3: For g1536_NF: The surface density of all stars plotted against radius. The red line is fit to the stellar bulge, while the magenta line is fit to the stars within the disk.

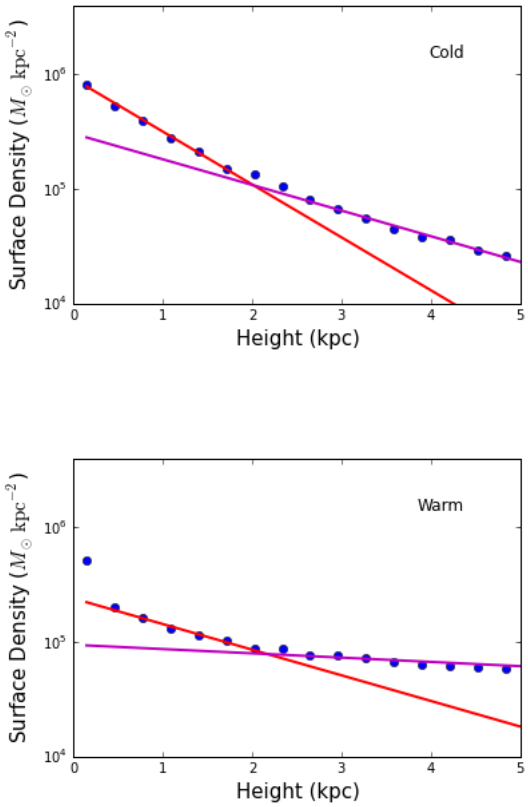

Figure A.4: For g1536_BW: The surface density of cold (top) and warm gas (bottom) in g1536_BW is plotted against height. An inner profile is fit in red, and an outer profile is fit in magenta.

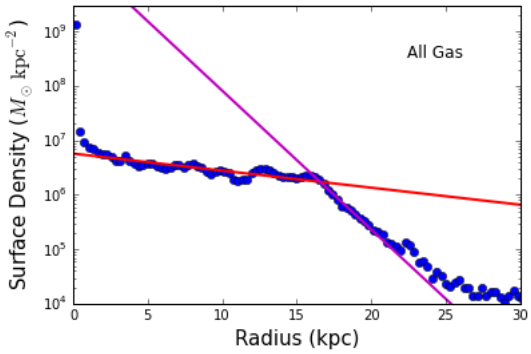

Figure A.5: For g1536_BW: The surface density of all gas plotted against radius. The break point, separating the outer and inner profiles, is used to define the edge of the disk.

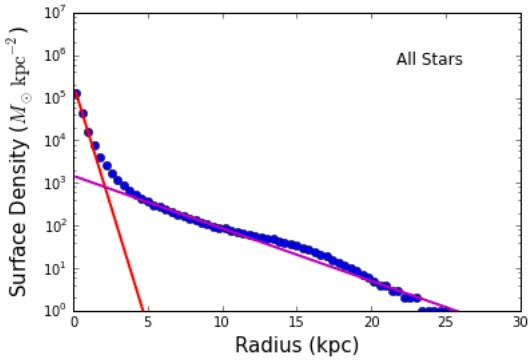

Figure A.6: For g1536_BW: The surface density of all stars plotted against radius. The red line is fit to the stellar bulge, while the magenta line is fit to the stars within the disk.

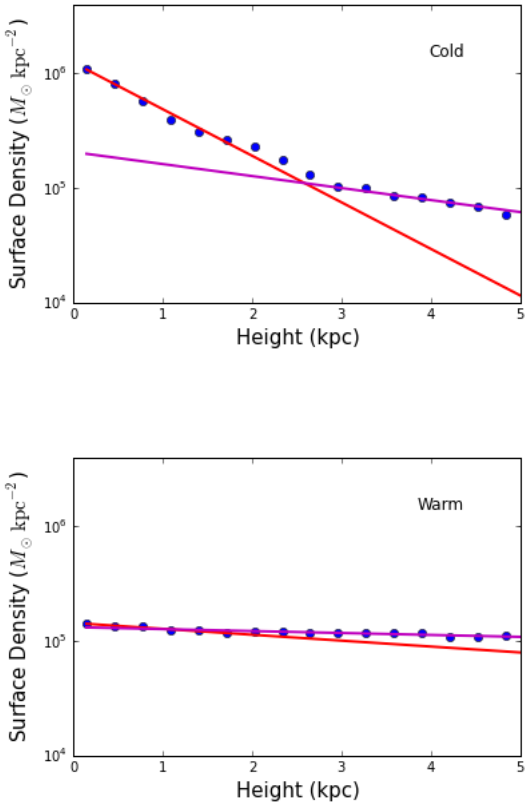

Figure A.7: For g1536_SB: The surface density of cold (top) and warm gas (bottom) in g1536_BW is plotted against height. An inner profile is fit in red, and an outer profile is fit in magenta.

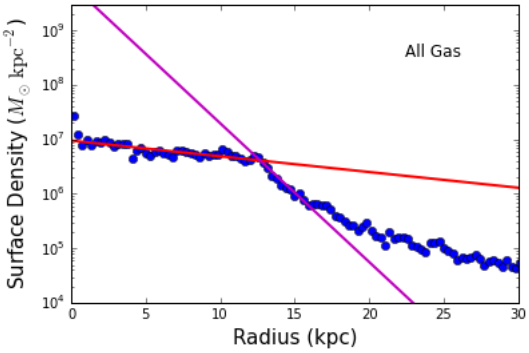

Figure A.8: For g1536_SB: The surface density of all gas plotted against radius. The break point, separating the outer and inner profiles, is used to define the edge of the disk.

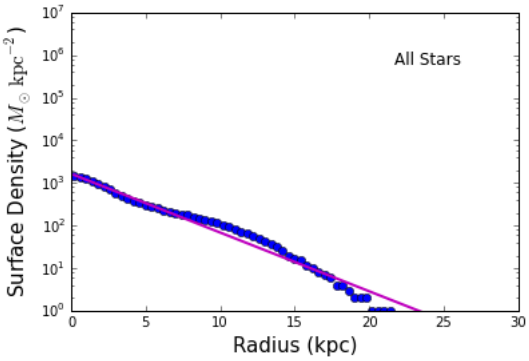

Figure A.9: For g1536_SB: The surface density of all stars plotted against radius. The red line is fit to the stellar bulge, while the magenta line is fit to the stars within the disk.

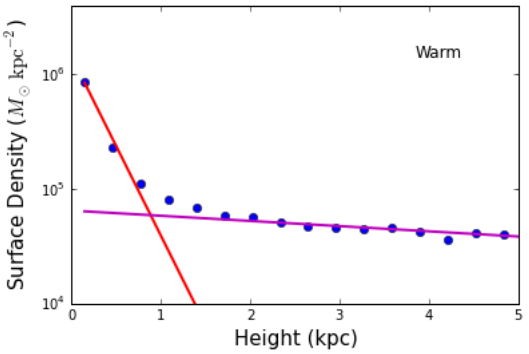

Figure A.10: For g15784_NF: The surface density of warm gas is plotted against height. An inner profile is fit in red, and an outer profile is fit in magenta.

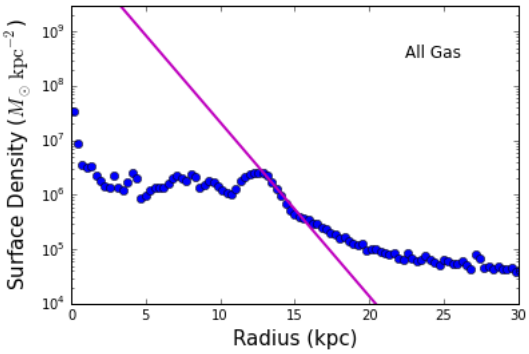

Figure A.11: For g15784_NF: The surface density of all gas plotted against radius. The break point, separating the outer and inner profiles, is used to define the edge of the disk.

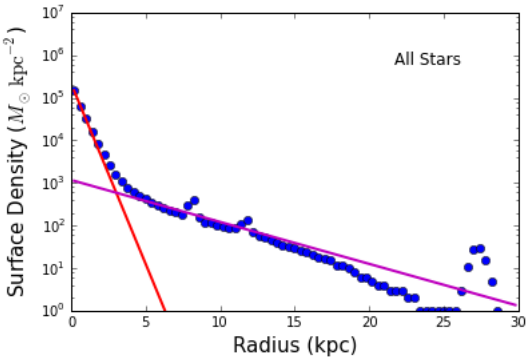

Figure A.12: For g15784_NF: The surface density of all stars plotted against radius. The red line is fit to the stellar bulge, while the magenta line is fit to the stars within the disk.

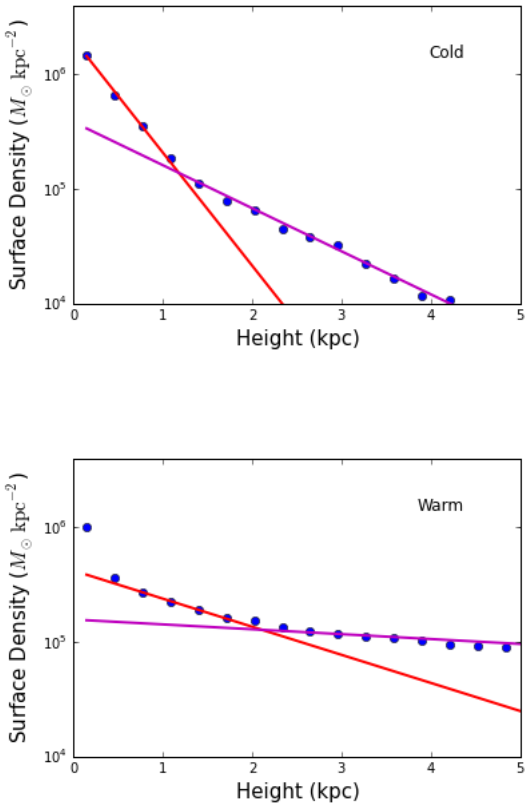

Figure A.13: For g15784_BW: The surface density of cold (top) and warm gas (bottom) in g15784_BW is plotted against height. An inner profile is fit in red, and an outer profile is fit in magenta.

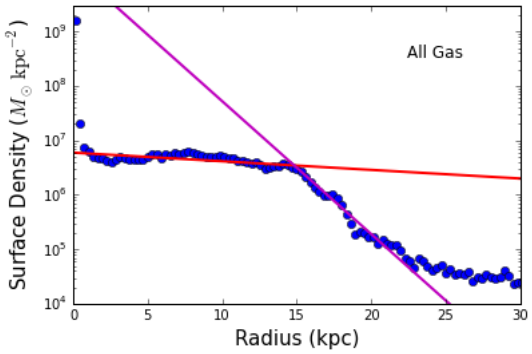

Figure A.14: For g15784_BW: The surface density of all gas plotted against radius. The break point, separating the outer and inner profiles, is used to define the edge of the disk.

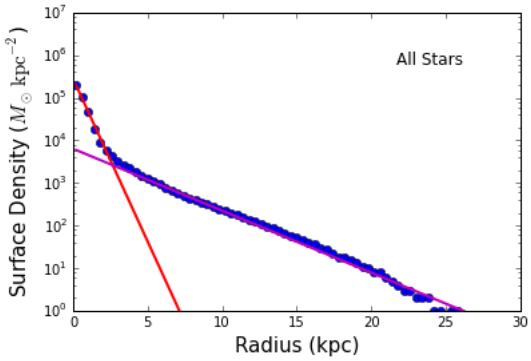

Figure A.15: For g15784_BW: The surface density of all stars plotted against radius. The red line is fit to the stellar bulge, while the magenta line is fit to the stars within the disk.

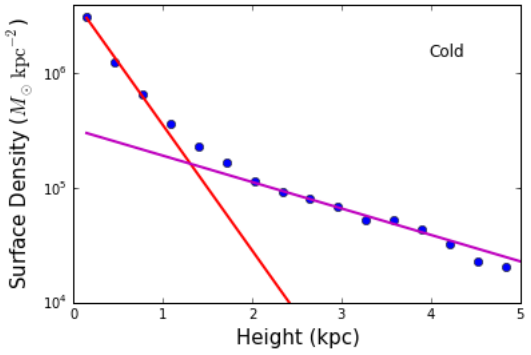

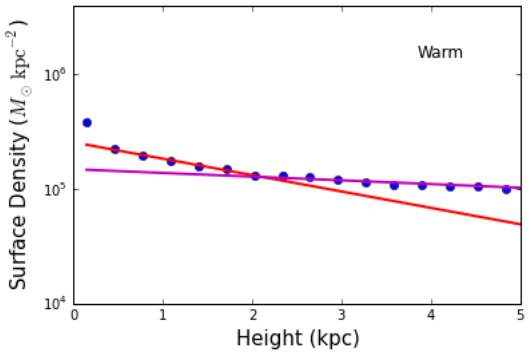

Figure A.16: For g15784_SB: The surface density of cold (top) and warm gas (bottom) in g15784_BW is plotted against height. An inner profile is fit in red, and an outer profile is fit in magenta.

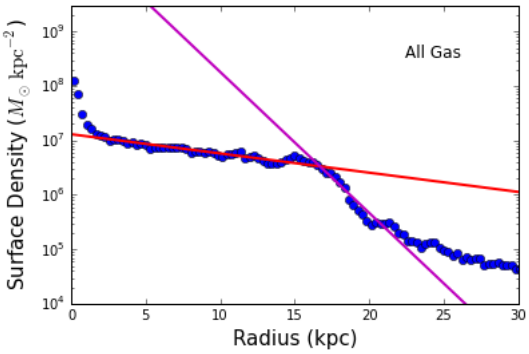

Figure A.17: For g15784_SB: The surface density of all gas plotted against radius. The break point, separating the outer and inner profiles, is used to define the edge of the disk.

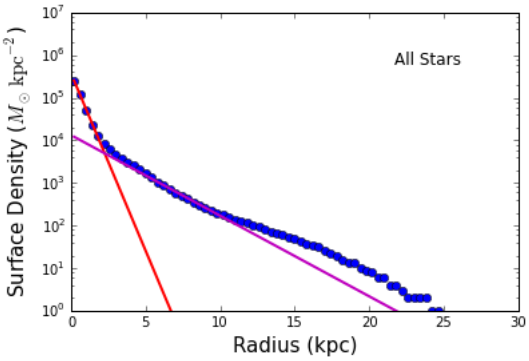

Figure A.18: For g15784_SB: The surface density of all stars plotted against radius. The red line is fit to the stellar bulge, while the magenta line is fit to the stars within the disk.

Bibliography

Aguerri, J. A. L., Balcells, M., & Peletier, R. F. 2001, Astronomy & Astrophysics, 367, 428

Arnett, W. D., Bahcall, J. N., Kirshner, R. P., & Woosley, S. E. 1989, ARA&A, 27, 629

Arzoumanian, D., André, P., Didelon, P., et al. 2011, Astronomy & Astrophysics, 529, L6

Babcock, H. W. 1939, Lick Observatory Bulletin, 19, 41

Bagetakos, I., Brinks, E., Walter, F., et al. 2011, The Astronomical Journal, 141, 23

Barnes, J., & Efstathiou, G. 1987, ApJ, 319, 575

Barnes, J. E. 1992, ApJ, 393, 484

Bate, M. R., & Burkert, A. 1997, MNRAS, 288, 1060

Baugh, C. M. 2006, 69, 3101

Begelman, M. C., & Nath, B. B. 2005, MNRAS, 361, 1387

Begeman, K. G., Broeils, A. H., & Sanders, R. H. 1991, Monthly Notice of the Royal Astronomical Society, 249, 523

Bigiel, F., Leroy, A., Walter, F., et al. 2010, The Astronomical Journal, 140, 1194

Birnboim, Y., & Dekel, A. 2003, MNRAS, 345, 349

Blanton, M. R., Dalcanton, J., Eisenstein, D., et al. 2001, The Astronomical Journal, 121, 2358

Blitz, L. 1993, in Protostars and Planets III, ed. E. H. Levy & J. I. Lunine, 125–161

Blumenthal, G. R., Faber, S. M., Primack, J. R., & Rees, M. J. 1984, 311, 517

Casuso, E., & Beckman, J. E. 2001, output, 557, 681

Chabrier, G. 2003, The Publications of the Astronomical Society of the Pacific, 115, 763

Chandrasekhar, S. 1931, ApJ, 74, 81

Coles, P., & Lucchin, F. 2002, Cosmology: The Origin and Evolution of Cosmic Structure, 2nd edn. (John Wiley & Sons, Ltd.)

Courtois, H. M., Zaritsky, D., Sorce, J. G., & Pomarède, D. 2015, MNRAS, 448, 1767

Courty, S., Gibson, B. K., & Teyssier, R. 2010, arXiv.org, 131

Cowie, L. L., & McKee, C. F. 1977, ApJ

Davis, M., Efstathiou, G., Frenk, C. S., & White, S. D. M. 1985, 292, 371

Dekel, A., Zolotov, A., Tweed, D., et al. 2013, MNRAS, 435, 999

Duffy, A. R., Schaye, J., Kay, S. T., et al. 2010, 405, 2161

Evrard, A. E., Summers, F. J., & Davis, M. 1994, Astrophysical Journal, 422, 11

Fraternali, F., & Binney, J. J. 2006, MNRAS, 366, 449

Gerritsen, J. P. E. 1997, 19

Gingold, R. A., & Monaghan, J. J. 1977, 181, 375

Gültekin, K., Richstone, D. O., Gebhardt, K., et al. 2009, ApJ, 698, 198

Heavens, A., Panter, B., Jimenez, R., & Dunlop, J. 2004, Nature, 428, 625

Hilz, M., Naab, T., Ostriker, J. P., et al. 2012, MNRAS, 425, 3119

Hinshaw, G., Larson, D., Komatsu, E., et al. 2013, ApJ, 208, 19

Hobbs, A., Read, J., & Nicola, A. 2015, MNRAS, 452, 3593

Hopkins, A. M., & Beacom, J. F. 2006, ApJ, 651

Hoyle, F. 1949, 195

Jeans, J. H. 1902, Philosophical Transactions, 199

Kalberla, P., & Kerp, J. 2009, ARA&A, 47, 27

Katz, N. 1992, ApJ, 391, 502

Katz, N., & Gunn, J. E. 1991, Astrophysical Journal, 377, 365

Katz, N., Quinn, T., Bertschinger, E., & Gelb, J. M. 1994, MNRAS, 270, L71

Keller, B. W., Wadsley, J., Benincasa, S. M., & Couchman, H. M. P. 2014, 442, 3013

Keller, B. W., Wadsley, J., & Couchman, H. M. P. 2015, 1

Kennicutt, R. C. 1998, ApJ, 498

Kennicutt, R. C., & Evans, N. J. 2012, ARA&A, 50, 531

Kereš, D., Katz, N., Weinberg, D. H., & Davé, R. 2005, MNRAS, 363, 2

Kirk, H., Klassen, M., Pudritz, R., & Pillsworth, S. 2015, ApJ, 802, 75

Klessen, R. S., Heitsch, F., & Mac Low, M.-M. 2000, ApJ, 535, 887

Kormendy, J., & Ho, L. C. 2013, ARA&A, 51, 511

Kormendy, J., & Richstone, D. 1995, ARA&A,, 33, 581

Lacey, C., & Cole, S. 1994, MNRAS, 271, 676

Lacey, C. G., & Fall, S. M. 1985, output, 290, 154

Lamers, H. J. G. L. M., & Cassinelli, J. P. 1999, Introduction to Stellar Winds (Cambridge University Press)

Leitner, S. N., & Kravtsov, A. V. 2011, ApJ, 734, 48

Lucy, L. B. 1977, 82, 1013

Mac Low, M.-M., & McCray, R. 1988, ApJ, 324, 776

Makiya, R., Enoki, M., Ishiyama, T., et al. 2015, PASj

Marasco, A., Debattista, V. P., Fraternali, F., et al. 2015, 1506.00652

Mashchenko, S., Couchman, H. M. P., & Wadsley, J. 2006, Nature, 442, 539

McKee, C. F., & Ostriker, J. P. 1977, ApJ

Mihos, J. C., & Hernquist, L. 1994, 437, 611

Moaz, D. 2007, Astrophysics in a Nutshell (Princeton University Press)

Navarro, J. F., & Benz, W. 1991, 380, 320

Navarro, J. F., Frenk, C. S., & White, S. D. M. 1997, ApJ, 490, 493

Navarro, J. F., & White, S. D. M. 1993, MNRAS, 265, 271

—. 1994, MNRAS, 267, 401

Oemler, A. 1973, ApJ, 180, 11

Peebles, P. 1982

Peebles, P., & Yu, J. T. 1970

Peebles, P. J. E. 1969, Astrophysical Journal, 155, 393

Peek, J. E. G. 2009, ApJ, 698, 1429

Penzias, A. A., & Wilson, R. W. 1965, ApJ, 142, 419

Peterson, B. M. 2001, in Advanced Lectures on the Starburst-AGN, ed. I. Aretxaga, D. Kunth, & R. Mújica, 3

Planck Collaboration, Ade, P. A. R., Aghanim, N., et al. 2015, ArXiv e-prints, arXiv:1502.01589

Press, W. H., & Schechter, P. 1974, ApJ

Price, D. J. 2010, astro-ph.IM

Rees, M. J., & Ostriker, J. P. 1977, MNRAS, 179, 541

Regan, M. W., Vogel, S. N., & Teuben, P. J. 1997, ApJl, 482, L143

Reynolds, S. P. 2008, ARA&A, 46, 89

Ritchie, Benedict W.; Thomas, P. A. 2001, MNRAS, 323, 743

Robin, A. C., Reylé, C., Derrière, S., & Picaud, S. 2003, Astronomy & Astrophysics, 409, 523

Rubin, V. C., Ford, W. K. J., & Thonnard, N. 1980, ApJ, 238, 471

Sancisi, R., Fraternali, F., Oosterloo, T., & van der Hulst, T. 2008, A&A Rev., 15, 189

Scannapieco, C., Wadepuhl, M., Parry, O. H., et al. 2012, MNRAS, 423, 1726

Schechter, P. 1976, ApJ, 203, 297

Schmidt, M. 1959, ApJ, 129, 243

Schmidt, M. 1963, Nature, 197, 1040

Shen, S., Wadsley, J., & Stinson, G. 2010, MNRAS, 407, 1581

Shu, F. H. 1982, The Physical Universe: An Introduction to Astronomy (Mill Valley, CA: University Science Books), 128

Smith, S. 1936, ApJ, 83, 23

Smoot, G. F., Bennett, C. L., Kogut, A., et al. 1992, ApJ, 396, L1

Springel, V., Di Matteo, T., & Hernquist, L. 2005, MNRAS, 361, 776

Springel, V., & Hernquist, L. 2003

Springel, V., White, S. D. M., Jenkins, A., et al. 2005, Nature, 435, 629

Stinson, G., Seth, A., Katz, N., et al. 2006, 373, 1074

Stinson, G. S., Bailin, J., Couchman, H., et al. 2010, MNRAS, 408, 812

Stinson, G. S., Brook, C., Macciò, A. V., et al. 2013, 428, 129

Strömgren, B. 1939, ApJ, 89, 526

Thacker, R. J., & Couchman, H. M. P. 2000, ApJ, 545, 728

—. 2001, ApJ, 555, L17

Toomre, A., & Toomre, J. 1972, ApJ, 178, 623

van Albada, T. S., Bahcall, J. N., Begeman, K., & Sanscisi, R. 1985, ApJ, 295, 305

Wadsley, J. W., Stadel, J., & Quinn, T. 2004, New Astronomy, 9, 137

Walter, F., Brinks, E., de Blok, W. J. G., et al. 2008, The Astronomical Journal, 136, 2563

White, S. D. M., & Frenk, C. S. 1991

White, S. D. M., & Rees, M. J. 1978, MNRAS, 183, 341

Williams, J. P., Blitz, L., & McKee, C. F. 2000, Protostars and Planets IV, 97

Wolfire, M. G., McKee, C. F., Hollenbach, D., & Tielens, A. G. G. M. 2003, ApJ, 587, 278

Zel'dovich, Y. 1970, Astronomy & Astrophysics, 5, 84

Zwicky, F. 1933, Helvetica Physica Acta, 6, 110

—. 1937, ApJ, 86, 217